Università degli Studi di Pisa
Facoltà di Scienze Matematiche, Fisiche e Naturali
Corso di Laurea Magistrale in Fisica

Tesi di Laurea Magistrale

Evidence of Inter-layer Interaction in Magneto-luminescence Spectra of Electron Double Layers

Relatore:
Prof. Vittorio Pellegrini

Candidato:
Ilirjan Aliaj

Anno Accademico 2011/2012

Contents

Introduction

In this thesis we shall present the results of a photoluminescence (PL) investigation of coupled electron bilayers confined in GaAs/AlGaAs double quantum wells in the Quantum Hall (QH) regime. The studies presented here provide evidence for the manifestation of the impact of inter-layer Coulomb interactions in magneto-PL spectra.

The rich physics of two-dimensional electron gases (2DEGs) under quantizing perpendicular magnetic fields manifests in the integer [1] and fractional [2] QH effect (QHE), discovered in 1980 and 1982, respectively. The QHEs consist in the precise quantization of the Hall resistivity of a cold (T$<$ 4 K) 2DEG around magic values of the magnetic field. The QHE is now understood as a macroscopic manifestation of the combined effect of quantum mechanical energy gaps and disorder. The energy gaps responsible for the integer QHE are due to Landau quantization and spin splitting, while the fractional QHE follows from an arrangement of electrons into highly-correlated states, which minimize the Coulomb energy [3]. Hence 2DEGs in the fractional QH regime have emerged as a laboratory where to explore the effects of Coulomb interactions and the emergence of novel quantum fluids of correlated electrons.

When two parallel 2DEGs are brought sufficiently close together, forming the electron bilayer, the physics is enriched by the interplay between inter-layer and intra-layer Coulomb interactions and by the presence of a new energy gap Δ_{SAS} associated to tunneling between the layers. Electron bilayers in semiconductor heterostructures have been the focus of intense theoretical and experimental work in the last twenty years. Initial numerical studies in 1987 suggested the existence of QH states at filling factors (the ratio of electrons to magnetic flux quanta) $\nu = 1/2$ [4] and $\nu = 1$ [5] in bilayers with $\Delta_{SAS} = 0$, which have no analogue in single layers. These states were later observed in transport experiments [6, 7], which provided evidence for the central role of the inter-layer correlations. In addition, in [7] an intriguing phase diagram for the QHE at $\nu = 1$ was found that resulted from the interplay between single particle tunneling and many-body inter-layer interactions. Subsequent theoretical works [8–11] showed that the $\nu = 1$ QH state at $\Delta_{SAS} = 0$ exhibits spontaneous $U(1)$ symmetry breaking and can be viewed as a pseudospin ferromagnet or equivalently as a BCS condensate of inter-layer excitons. This phase displays remarkable properties, such as the existence of a Goldstone mode and excitonic superfluidity. Transport experiments [12–16] have provided compelling evidence of these properties.

Optical techniques such as magneto-absorption spectroscopy [17] and inelastic light scattering [18–21] have been successfully applied to the study of QH bilayers but only around $\nu = 1$. However, PL spectroscopy, which can be considered as the most straightforward optical technique and provides complementary information to transport experiments or other optical techniques, was only marginally employed in the study of QH bilayers. Indeed, as demonstrated by many studies in single layers [22–25], by exploring the recombination of the electrons in the conduction-band Landau levels with photo-excited holes

in the valence band, PL can offer unique insights in the ground-state properties of the 2DEGs.

With this thesis work we fill the above-mentioned experimental gap and report the magneto-PL behavior of two bilayer samples with zero and finite tunneling gap in a wide range of magnetic fields and at temperatures down to 50mK. We exploit the polarization properties of the emitted light to identify contributions from electrons with opposite spin. The results presented in this thesis demonstrate that the PL is a sensitive probe of inter-layer correlation in coupled electrons bilayers. In particular we show how the PL spectra are affected by the occurrence of the inter-layer correlated QH states such as the ones at $\nu = 1/2$ and 1.

The thesis is organized as follows :

Chapter 1 introduces the fundamentals of the QHE in 2DEGs, with emphasis on bilayers. It starts with the description of the techniques (modulation doping and MBE growth) that have made possible to realize nearly ideal 2DEGs confined in GaAs/AlGaAs quantum wells. Then it presents the basic physics underlying the integer and fractional QHE in single layers. The rest of the chapter focuses on the properties of bilayer systems in the QH regime and offer a review of the transport experiments that provide evidence for the main novelties brought about by bilayers : the QHE at $\nu = 1/2$, the phase diagram for the QHE at $\nu = 1$, and the spontaneous symmetry breaking at $\nu = 1$ with its remarkable consequences such as the existence of a Goldstone mode and excitonic counter-flow supercurrents. Finally, in the conclusions we motivate the investigation of the above phenomena through PL spectroscopy.

The basic facts of PL spectroscopy are described in **chapter 2**, together with a brief review of PL studies of 2DEGs in the QH regime. We illustrate, in particular, some well-established experimental results on the PL of single layers, *e.g.* the role of polarization analysis of the optical emission, the signatures of the QH states in the luminescence spectra, and the role of the hidden symmetry that results from a peculiar cancellation of the electron-electron and electron - (photo-generated) hole interactions. This chapter contains also a technical description of the cryogenic equipment and optical setup used in this thesis for the PL measurements at very low temperatures, and the setup for the auxiliary transport measurements.

Chapter 3 is dedicated to the presentation and analysis of the PL data from the sample with a finite tunneling gap while the data from the sample without tunneling gap are presented in **chapter 4**. In both chapters we present the PL spectra, and the resulting intensities and energies of the PL peaks versus magnetic field as extracted from the spectra. By comparing the data with transport experiments performed on the same samples we identify the QH states and the impact of inter-layer interactions on the PL evolution.

The results of our experiments are resumed in the **conclusions**, together with some possible future extensions of the present work.

Chapter 1

The Quantum Hall Effect

1.1 Experimental Realization of Two-Dimensional Electron Gases (2DEGs)

A system of electrons whose motion is confined in one spatial direction, but free to move in the perpendicular plane, constitutes a Two-Dimensional Electron Gas (2DEG).

Here we deal with the case in which confinement is produced by a quantum well (QW) potential. Let's consider a one-dimensional particle with mass m trapped in an infinite square well potential with width L. It can only occupy discrete energy levels of the form :

$$E_n = \frac{\hbar^2}{2mL^2}n^2, \quad \text{where } n = 1, 2, \dots$$

If we cool down the system to a temperature $k_B T \ll E_2 - E_1$, then the particle can only "reside" in the ground ($n = 1$) state, so we have effectively blocked the dynamics of the particle in the well direction.

How can we create such a confining potential with semiconductor materials ? It turns out that in bulk GaAs electron states near the edge of the conduction band (CB) can be well described as freely moving particles with an effective mass $m^* = 0.067m_e$. In the presence of an AlGaAs/GaAs interface, these electrons "feel" an effective potential described by the spatial profile of the band edge. A rigorous motivation for this fact lies in the envelope function formalism [26].

The ternary compound crystal $Ga_{1-x}Al_xAs$ has a bandgap between those of GaAs ($E_{\text{gap}} = 1.43$ eV) and AlAs ($E_{\text{gap}} = 2.1$ eV)[1] which increases with x. The total discontinuity at the interface with GaAs is taken up mostly by the conduction band edge $\Delta E_c \approx 0.65\Delta E_{\text{gap}}$ and the remaining is left to the valence band $\Delta E_v \approx 0.35\Delta E_{\text{gap}}$, so both electrons and holes in the GaAs side "see" a barrier.

If we combine AlGaAs and GaAs materials, we can realize a QW. In Fig. 1.1(a) we can get a better idea of the composition of a realistic QW sample. In ordinary structures the CB offset is $\Delta E_c \sim 100$ meV and the QW width is $d \sim 10$ nm, so this well can host at least 2 confined states with a typical separation $E_2 - E_1 \sim 10 - 100$ meV. Liquid Helium temperature (T ≈ 4 K) will be sufficient for keeping electrons in the lowest energy level.

It's worth noting that since we have only modified the structure in one direction, electrons will be free to move in the other two - the plane perpendicular to the well. The in-plane Bloch wavevector $\mathbf{k}_{||}$ remains a good quantum number and each confined level

[1] The values given here are the measured bandgaps at room temperature. The bandgap of semiconductors tends to increase as the temperature is decreased.

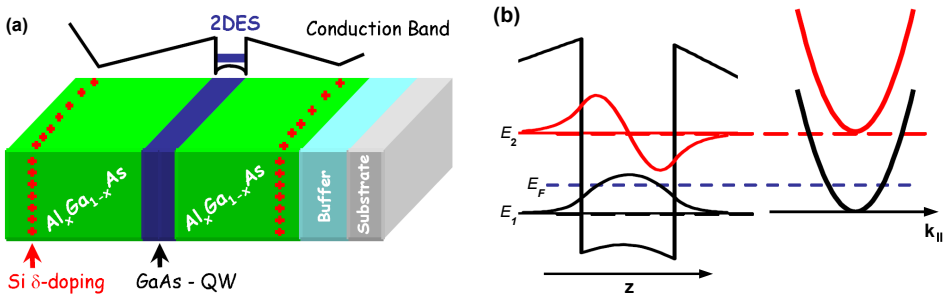

Figure 1.1: Realization of a 2DEG confined in a semiconductor heterostructure. (a) Schematic illustration of the layered structure of a GaAs/AlGaAs modulation-doped QW; the black curve is the spatial profile of the bottom of the CB through the sample. In the left part of (b) we show the CB potential well together with its lowest two confined energy states (E_1, E_2) and the corresponding envelope wavefunction profiles along the growth direction. In the right part we display the subbands associated with each of the levels. Here the Fermi level E_F (dashed horizontal line) lies in the lowest subband. After Ref. [28].

gives rise to a subband with in-plane dispersion :

$$E_n(\mathbf{k}_{||}) = E_n + \frac{\hbar^2 \mathbf{k}_{||}}{2m^*},$$

as illustrated in Fig. 1.1(b). Electrons will occupy the double degenerate states (owing to the spin degree of freedom) in the lowest subband according to their density and temperature.

Finally, how do we get the electron gas ? Pure semiconductors at T $\approx$ 0 K are insulating, so we need to dope the well with donors, in order to get electrons in the CB. Silicon impurities are commonly used as donors in GaAs crystals. In appropriate conditions they replace the Ga atoms and since they have an additional outer-shell electron, they can easily "donate" it to the crystal. However, we have to keep the temperature above the donor binding energies, otherwise electrons get caught by the donors (carrier freeze-out). Furthermore ionized donors produce considerable potential fluctuations in space, which scatter electrons.

The modulation-doping technique, introduced at the end of the 70' [27], has been very successful in avoiding these problems. It consists in placing the doping layer not in the well, but in the barrier (AlGaAs layer) (see Fig. 1.1(a)). The doping sheet should be close to the interface to allow the donors to transfer their extra electrons in the QW, but not too near so as to suppress the Coulomb scattering of the mobile electrons from the ionized donors. In practice the Si doping layer is placed at a typical distance of 0.1 - 0.5 μm from the well. In this way electron mobilities of 10^7 cm^2/Vs or above can be achieved at low temperatures, leading to long mean free paths of the order of 1 mm.

The successful fabrication of these samples relies on the Molecular Beam Epitaxy (MBE) growth technique. Figure 1.2 shows the schematics of a typical MBE system. Basically the MBE machine is a high vacuum chamber, inside which there are several cells containing the source materials. These materials are heated until vaporization and leave the cells through small effusion orifices, under the form of highly collimated molecular beams, whose flux rate can be controlled by shutters placed in front of each furnace. Various molecular beams containing the Ga, As, Al and Si elements are aimed at a GaAs substrate where the film grows epitaxially. The composition and quality of the film can be probed real-time during the growth, using well established surface spectroscopy techniques. With MBE one can grow samples with atomic layer precision.

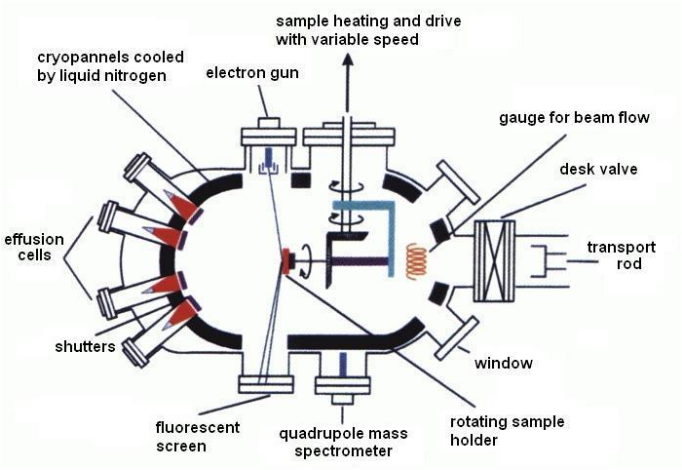

Figure 1.2: A schematic of the MBE growth system. Note the electron gun and fluorescent screen that continuously record the diffraction pattern of high energy electrons from the sample, to monitor the geometry and morphology of its surface. The growth chamber walls are cooled by liquid N_2 which ensures high vacuum by cryopumping atoms and molecules on the walls. The mechanical rotator connected to the sample holder guarantees a more uniform beam deposition on the substrate.

So far we have discussed about the realization of a single 2DEG (single layer) confined in a QW. With the same methods one can also fabricate double QWs, which correspond to bilayers of 2DEG when doped on each side. As we will see, interesting phenomena are observed if the densities of the two layers are equal.

Important parameters in bilayers are : the distance d between the layers (defined as the distance between the centers of the two QWs), which controls the degree of inter-layer Coulomb interaction among electrons, and the height of the barrier in-between the wells, which together with d controls the capability of single electrons to tunnel from one well to the adjacent one.

The rich physics of electron bilayers in double quantum wells lies in the ability to tune this two important physical parameters independently during the growth. In fact the distance is controlled by the thickness of the AlGaAs barrier, while the height (which is directly related to the AlGaAs bandgap) can be varied by changing the Al concentration. For example if one needs to suppress the single particle tunneling between the layers, without changing their mutual interaction, it is sufficient to increase the Al concentration in the barrier. In order to decrease the Coulomb coupling between the layers, without changing the tunneling properties, one has to make a thicker barrier with less Al.

1.2 Two-Dimensional Electron States in a Magnetic Field

Let's consider a single two-dimensional electron, in a rectangular box of dimensions L_x and L_y of the xy plane, in the presence of a perpendicular uniform and constant magnetic field $\mathbf{B} = B\hat{\mathbf{z}}$. The dynamics of the electron is described by the Hamiltonian :

$$H = \frac{1}{2m_c}\left(\mathbf{p} + \frac{e}{c}\mathbf{A}\right)^2 - g\mu_B \mathbf{B}\frac{\mathbf{S}}{\hbar},$$

where m_c is the electron effective mass ($0.067m_e$ in GaAs), $\mu_B = e\hbar/2m_e c$ is the Bohr magneton and g is the effective gyromagnetic ratio. Free electrons have $g \approx 2$, but because of the spin-orbit coupling, it renormalizes to $g \approx 0.4$ in GaAs.

In the Landau gauge $\mathbf{A} = B(-y, 0, 0)$, the stationary states and corresponding energies are :

$$\psi_{n,k,s_z}(\mathbf{r}) \propto e^{ikx}\, HO_n\left(\frac{y - y_k}{\ell}\right) |s_z\rangle$$
$$E_{n,k,s_z} = \hbar\omega_c\left(n + \frac{1}{2}\right) + g\mu_B B s_z, \tag{1.1}$$

where HO_n is the n-th dimensionless wavefunction of the Harmonic Oscillator (HO), $\omega_c = \frac{eB}{m^* c}$ the cyclotron frequency, $\ell = \sqrt{\frac{\hbar c}{eB}}$ is the magnetic length, $y_k = -k\ell^2$, and $s_z = \pm\frac{1}{2}$ is the z component of the electron's spin.

The following relations are useful for estimating typical energy scales in GaAs heterostructures :

$$\hbar\omega_c \approx 19.2B, \qquad E_Z \approx 0.27B, \qquad e^2/\epsilon\ell \approx 50\sqrt{B}, \tag{1.2}$$

where B is measured in Tesla and the energies in Kelvin.

The wavefunction describes a plane wave in the x direction, while in the y direction it represents a HO displaced by an amount proportional to the x momentum, localized around y_k to within $\sqrt{n}\ell$. This HO states are reminiscent of the classical isochronous circular motion of electrons in a magnetic field, with the cyclotron frequency ω_c. The set of wavefunctions with the same n defines a Landau level (LL).

The energy levels are independent of the x momentum, so their degeneracy coincides with the number of allowed values for k. Assuming periodic boundary conditions $\psi(0, y) = \psi(L_x, y)$ and requiring that the particle lies within the box in the y direction $0 < y_k < L_y$, we get a degeneracy of :

$$\frac{L_y/\ell^2}{2\pi/Lx} = \frac{\text{Area}}{2\pi\ell^2} = \frac{B \cdot \text{Area}}{\frac{hc}{e}}$$

for each Landau level. The flux quantum $\Phi_0 \equiv hc/e \approx 4.14 \times 10^{-7}\text{gauss/cm}^2$ so if we apply for example $B = 1$ T, we get $\sim 10^{10}$ states/cm^2 in each Landau level. For a 2DEG with density n, we can define the filling factor $\nu = \frac{n}{B/\Phi_0}$, which tells us how many levels will be occupied at T = 0 K. Ordinary samples have densities in the range $10^9 - 10^{12}$ cm^{-2}.

In the following we will also need the representation of the electron states in the symmetrical gauge $\mathbf{A} = \left(-\frac{By}{2}, -\frac{Bx}{2}, 0\right)$. Given the axial symmetry of the problem, the states inside the same LL will be distinguished by their angular momentum L_z. In the lowest LL, the orbital wavefunctions have the form :

$$|m, n = 0\rangle = \frac{z^m}{\sqrt{2\pi 2^m m!}} \exp\left(-\frac{zz^*}{2}\right) \quad m \geq 0.$$

Here we are using complex dimensionless coordinates in the plane $z = (x + iy)/\ell$. Writing in polar coordinates $z = \rho e^{i\phi}$, the wavefunctions $|m, 0\rangle \propto \exp(im\phi)$ are eigenstates of L_z with eigenvalue $m\hbar \geq 0$, in other words they can only rotate counter-clockwise. The handedness of motion is due to the time invariance breaking brought by the magnetic field. In terms of charge distribution, these new states describe concentric rings of width $\sim \ell$, and radius $\sqrt{\langle m, 0|zz^*|m, n = 0\rangle} = \sqrt{2(m+1)}\ell$.

In conclusion, perpendicular quantizing magnetic fields bring two main novelties : the kinetic energy *discretizes* in Landau levels and each level has a *macroscopic* degeneracy.

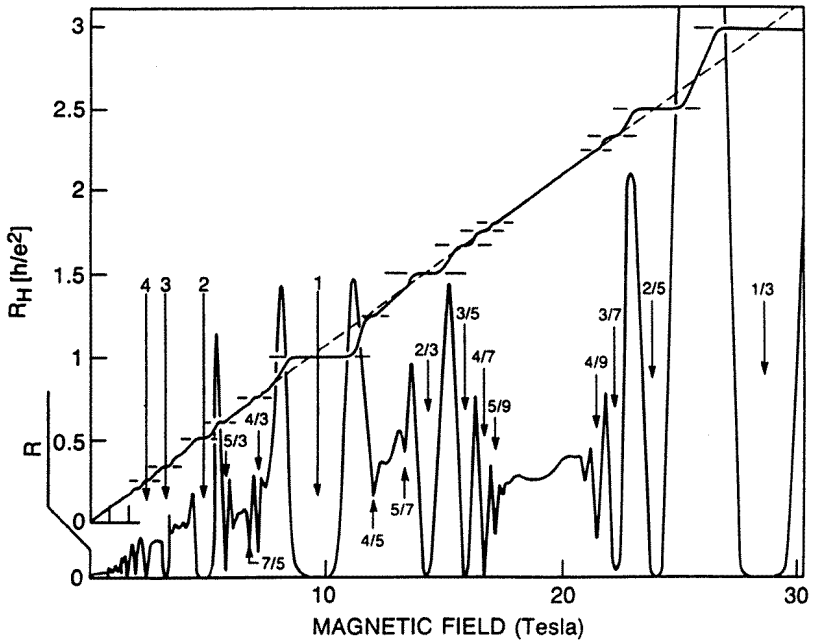

Figure 1.3: Longitudinal and Hall resistivity as a function of magnetic field for a modulation-doped GaAs/AlGaAs heterojunction at 85 mK. The electron gas has a density of $\sim 3 \times 10^{11}$ cm^{-2} and a mobility of $\sim 10^6$ cm^2/Vs. A large number of plateaus in the Hall resistivity (R_H) and zeros in the longitudinal resistivity (R) are identified. After Ref. [30].

1.3 Quantum Hall Effect in Single Layers

An ideal 2DEG is invariant under translations in the plane. In a real sample, this condition is approached when T $\approx$ 0 K and *disorder* is negligible. By disorder we mean any random potential, which couples with electrons e.g. defects, impurities, Coulomb potentials from the ionized donors etc.

This symmetry alone determines the transport properties of the system [29]. In fact, suppose we have a 2DEG with surface density n in a transverse $\mathbf{B}$ field and we turn on a small in-plane electric field $\mathbf{E}$. Because of translation invariance, we can view the system from any other frame S' moving with a velocity $\mathbf{v}$ with respect to the rest frame. Now if we choose $\mathbf{v} \perp \mathbf{E}$, such that $\mathbf{E} + \mathbf{v} \times \mathbf{B}/c = \mathbf{0}$, then $\mathbf{E}' = \mathbf{0}$ in S'. In the absence of the electric field, only uniform and constant currents are allowed, which would introduce some privileged direction in S'. Hence

$$\mathbf{j}' = \mathbf{0} \quad \Longrightarrow \mathbf{j} = -ne\mathbf{v}.$$

The above conditions are fulfilled by choosing $\mathbf{v} = c\mathbf{E} \times \mathbf{B}/\mathbf{B^2}$, which allows us to write the resistivity tensor of the gas :

$$\mathbf{E} = \underline{\underline{\rho}}\,\mathbf{j}, \qquad \text{where} \quad \underline{\underline{\rho}} = \frac{h}{\nu e^2}\begin{pmatrix} 0 & 1 \\ -1 & 0 \end{pmatrix}. \tag{1.3}$$

The system may seem perfectly conducting, since $\rho_{xx} = 0$, but it is not since also $\sigma_{xx} = 0$. If we inject a current in the sample and measure the voltage drop across the current, we should find that the transverse resistivity rises linearly with the field ($B \propto \nu^{-1}$), with a slope depending only on the gas density.

In Fig. 1.3 we show transport data taken from a high mobility 2DEG at very low temperatures. As it can be seen, there are spectacular deviations from the predicted

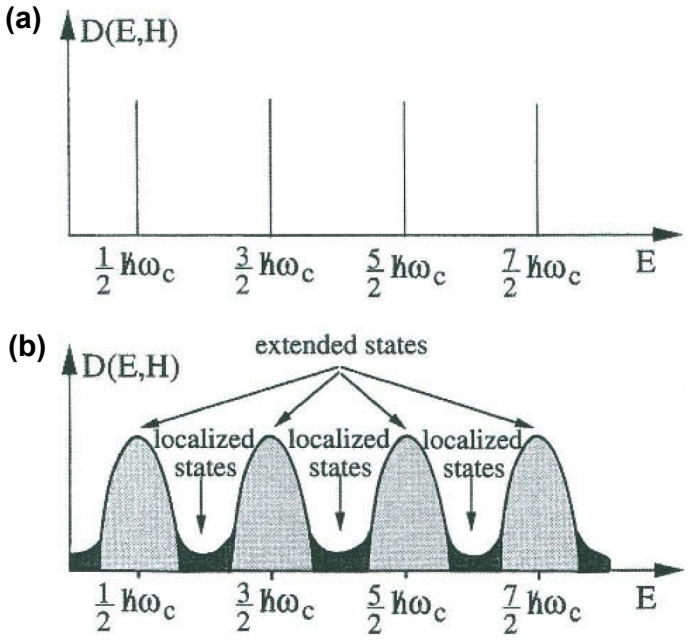

Figure 1.4: Density of states for spinless non-interacting 2D electrons at high magnetic fields in (a) an ideal sample with translational invariance (b) a weakly disordered sample, where Landau levels broaden into bands constituted by extended(light gray) and localized(dark grey) states. After Ref. [31].

simple behaviour: at certain magnetic field intervals, the transverse resistivity develops plateaus of universal values $\frac{h}{\nu e^2}$ with ν being an integer or odd denominator fraction. Also the system becomes dissipationless, *i.e.* the longitudinal resistivity is zero. These facts are verified regardless of the microscopic details of the sample: the exact choice of semiconductor material, the sample geometry, the presence of impurities, the precise value of the electron density etc. In addition the measured accuracy of quantization of the integer plateaus is $\sim 10^{-8}$. The appearance of plateaus with integral/fractional values of ν is the essential manifestation of the Integral/Fractional Quantum Hall Effect (QHE).

The Integral QHE bears an explanation in a picture of independent spinless electrons, when the effect of disorder is properly taken into account [31]. In fact the density of states for spinless electrons in a magnetic field is a comb of equally-spaced deltas and the Fermi level (E_F) can only jump between them (Fig. 1.4(a)). Suppose that the system is weakly disordered, which means that the energy scale of the disorder potential $V_{dis} \ll \hbar\omega_c$. The rigorous treatment of this system is a difficult task, so we only quote the result. Disorder removes the degeneracy and broadens the sharp Landau levels into bands. A small fraction of states with $E \approx \hbar\omega_c(n + 1/2)$ remain extended and can thus carry current, while the majority become localized (see also Fig. 1.4(b)).

Let's now suppose that we sweep the Fermi level, *e.g.* by changing the magnetic field. When E_F lies in a region of localized states, then the population of the conducting(extended) states is not changing and neither are the transport properties. This explains the constancy of both ρ_{xx} and ρ_{xy} within the plateau region. Transitions between the plateaus correspond to the Fermi level lying near the band peaks or equivalently to variations in the population of extended states.

Obviously this argument is not modified by taking into account the spin, since opposite spin Landau levels are still separated by a gap. Anyway since the cyclotron gap is almost 60 times larger than the spin one, we expect even integer plateaus to be more robust.

Let's concentrate now on the Fractional QHE. The existence of this effect is really puzzling : on one hand the charged excitations are gapped, because the system is dissipationless ($\rho_{xx} = 0$); on the other hand ν is fractional so the highest occupied LL is only partially filled and therefore there should be no gap. The key fact is that, in the partially filled LL, Coulomb interactions can give rise to an energy gap.

To account for the QHE at $\nu = 1/m$, R.B.Laughlin introduced a class of variational ground-state wavefunctions, which are conveniently expressed in the symmetric gauge as :

$$\Psi_{1/m} \propto \prod_{i<j} (z_i - z_j)^m \exp\left(-\frac{1}{4}\sum_j |z_j|^2\right). \tag{1.4}$$

$\Psi_{1/m}$ describes fully spin-polarized electrons, so in order to satisfy the antisymmetry requirement, m must be odd. It can be noted, in particular, that $|\Psi_{1/m}|^2$ vanishes as $|\mathbf{r}_i - \mathbf{r}_j|^{2m}$ when any two particles i and j approach each other. Thus $\Psi_{1/m}$ builds in good correlations by having electrons avoid each other and therefore lowering the Coulomb energy. The origin of the gap responsible for the fractional QHE lies in the special correlations contained in $\Psi_{1/m}$ [29]. Exact diagonalization and numerical simulations for few particle systems [3] confirm the fact that $\Psi_{1/m}$ has a good overlap with the true ground state for $m < 7$.

At filling factor exactly equal to $1/m$ (for example $\nu = 1/3$) the electron system can carry current without dissipation, because of the gap, leading to a longitudinal and Hall conductivity of 0 and e^2/mh, respectively . When ν deviates slightly from $1/m$, charged excitations are created which get caught in the disorder potential and give no contribution to the transport. Moving further away from $\nu = 1/m$ such charged excitations get delocalized and the system jumps from one QH state to another.

The understanding of the Laughlin fractions can be extended through different mechanisms to other filling factors that exhibit QHE. We cite Jain's *composite fermion* picture [32], which has the praise of connecting integer QH states n, to fractional ones $\nu = n/(2nk \pm 1)$, with k integer. Candidate states with full spin polarization for $\nu = 2/3, 2/5, 3/5, 3/7\ldots$ can be constructed in this way. Note that this picture doesn't modify the odd denominator rule.

Finally we consider how the spin modifies the picture discussed so far. QH states with $\nu = 1/m$ behave as ferromagnets with full spin alignment. At $B = 10T$, from (1.2) we have that $E_Z \approx 2.7$ K , so one might naively think that charged excitations across the Zeeman gap would destroy the $\nu = 1/m$ QH state at T ~ 1 K . Such an excitation can be constructed by flipping the spin of one electron and separating it from the hole left behind in the spin up level by a distance $\gg \ell$. Thus the electron-hole attraction is negligible, but since the orbital wavefunction is no more exchange antisymmetric there is an energy cost $\sim e^2/\epsilon\ell \approx 160K$. Therefore such charged excitations have an energy of $E_Z + \frac{e^2}{\epsilon\ell} \gg E_Z$. We deduce that Coulomb interactions strongly stabilize the ferromagnetic states, even in the limit $E_Z \longrightarrow 0$.

While this picture holds at $\nu = 1/3$, at other filling factors $(2/3, 2/5\ldots)$ unpolarized QH states compete in energy with the ferromagnetic ones and there could even be phase transitions between the two if, for example, we increase the electron density. Thus the degree of freedom related to spin plays a significant role in the QHE.

This work focuses on the new phenomena brought by another degree of freedom, related to layer occupation in electron bilayers, that we will discuss in the next section.

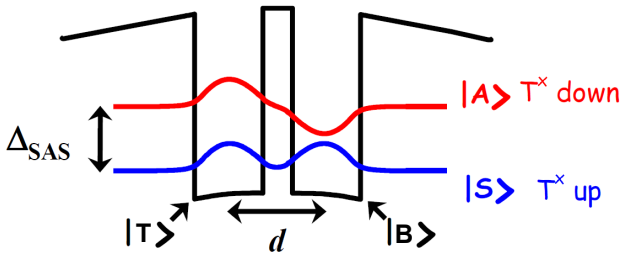

Figure 1.5: Potential energy profile for conduction band electrons along the growth axis of a double quantum well structure with tunneling. The electron wavefunction along the growth axis for the symmetric/antisymmetric state is shown in the red/blue curve. The two states are separated by a finite gap Δ_{SAS}. T_x is the pseudospin quantum number. After Ref. [28].

1.4 Quantum Hall Effect in Double Layers

A double layer is a system composed of two parallel 2DEGs and it can be realized in a modulation doped double QW (see Fig. 1.5). This system is characterized by a new degree of freedom associated with electron occupation in one of the two layers. This degree of freedom can be formally described in complete analogy to spin, by introducing the pseudospin operators τ.

Let's call $|B\rangle/|T\rangle$ the state in which an electron is in the bottom/top layer. We define the operators τ by imposing that in the basis state $|T\rangle, |B\rangle$ they are represented by the Pauli matrices σ.

When the electron is localized in the top / bottom layer, we say that it has pseudospin up / down, which means that pseudospin points in the z direction with eigenvalue $+1/-1$. These states are degenerate for two independent layers not coupled by any mechanism. Actually the parallelism between spin and pseudospin is not limited to the case when $\langle\tau\rangle \parallel \hat{z}$. Any other orientation of pseudospin has a physical meaning and it is physically realizable in a bilayer system. For an arbitrary state $|\psi\rangle = \alpha|T\rangle + \beta|B\rangle$, the z component $\langle\tau^z\rangle = |\alpha|^2 - |\beta|^2$ measures the charge difference between the layers.

We will show in the following that the τ^x eigenstates are useful when tunneling between the layers becomes possible. To understand this, let's imagine two independent empty layers, put an electron in one of the layers and start pushing them closer. Now as the wells get closer, the barrier between the two gets thinner and the electron can tunnel to the adjacent empty well. The latter corresponds to a perturbing potential which depends only on z, consequently the tunneling process conserves both the spin and the in-plane momentum. Remembering that B and T represent some fixed spin and in-plane momentum, the energies and stationary states in the presence of tunneling become

$$\begin{aligned} |S\rangle &= \frac{1}{\sqrt{2}}\left(|T\rangle + |B\rangle\right) \qquad E_S = -t \\ |AS\rangle &= \frac{1}{\sqrt{2}}\left(|T\rangle - |B\rangle\right) \qquad E_{AS} = t, \end{aligned} \tag{1.5}$$

where t is a positive real number determined by the parameters of the double well potential. The states $|S\rangle$ and $|AS\rangle$ are eigenstates of τ_x and their wavefunctions are shown in Fig. 1.5. Hence, tunneling aligns the pseudospins along the positive x direction and opens a gap $\Delta_{SAS} \equiv 2t$, not present in single layers. In the spirit of the spin analogy, we may say that tunneling behaves as a pseudomagnetic field and opens a pseudo-Zeeman gap.

So far we have used a single-particle picture. Let's now discuss the role of Coulomb interactions. To this end let's imagine to increase the height of the barrier, so that tunneling becomes negligible, and add another electron. We have two possibilities : have the two electrons in the same layer or in opposite layers. The electrons feel their mutual Coulomb repulsion and can distinguish between the two possibilities. In fact if their spin and orbital quantum numbers are fixed, the repulsion will be weaker in the opposite layer configuration, because of the spatial separation due to the finite width of the barrier. If we call V_A/V_E the intra-layer/inter-layer Coulomb interaction potential we have :

$$V_A(\mathbf{r}) = \frac{e^2}{r} \qquad V_E(\mathbf{r}) = \frac{e^2}{\sqrt{r^2+d^2}},$$

where d is the inter-layer distance, that in real samples is taken as the distance between the centers of the wells. We can thus see that the interaction between electrons depends on their relative pseudospin orientation. The intra- and inter-layer configurations for two particles (i,j) can be distinguished by the product $\tau_i^z\tau_j^z$ which assumes respectively the values $+1$ and -1. So the total electron-electron interaction Hamiltonian can be written as :

$$\begin{aligned} H_{ee} &= \sum_{i<j} \frac{1+\tau_i^z\tau_j^z}{2} V_A(\mathbf{r}_{ij}) + \frac{1-\tau_i^z\tau_j^z}{2} V_E(\mathbf{r}_{ij}) \\ &= \sum_{i<j} V_0(\mathbf{r}_{ij}) + \underbrace{\tau_i^z\tau_j^z V_z(\mathbf{r}_{ij})}_{V_{ps}}, \end{aligned} \tag{1.6}$$

where we have defined

$$V_0 \equiv \frac{V_A+V_E}{2} \quad \text{and} \quad V_z \equiv \frac{V_A-V_E}{2} > 0.$$

Anyway the interaction depends only on τ^z, so it will be invariant under rotation of pseudospin around the z axis. Therefore in the absence of tunneling the bilayer system doesn't have the full $SU(2)$ symmetry (as the spin), but only $U(1)$ symmetry associated with the conservation of the charge difference between the layers.

The typical energy scales in the presence of a magnetic field for intra-layer and inter-layer interactions are $e^2/\epsilon\ell$ and $e^2/\epsilon d$ respectively. Their relative importance can be conveniently parametrized by the ratio d/ℓ. The system can be found in one of the three regimes : a) *Independent Layers* $d/\ell \gg 1$, in which repulsion between the layers can be safely neglected b) *Single Layer* $d/\ell \ll 1$, in which layers are so close that the difference between intra-layer and inter-layer interaction vanishes and we recover the $SU(2)$ symmetry. c) *Intermediate Regime* $d/\ell \sim 1$, in which there is competition between intra-layer and inter-layer interactions. The samples studied in this thesis belong to this regime.

Additionally, we can define a filling factor for each individual layer:

$$\nu_{\uparrow(\downarrow)} = \frac{N_{\uparrow(\downarrow)}}{2\pi\ell^2},$$

where $\uparrow$ ($\downarrow$) stands for the top (bottom) layer, and the total filling factor is:

$$\nu = \frac{N_\uparrow + N_\downarrow}{2\pi\ell^2}.$$

In this thesis we will be concerned with symmetric (balanced) samples with $\nu_\uparrow = \nu_\downarrow$ and $\nu = 2\nu_{\uparrow(\downarrow)}$

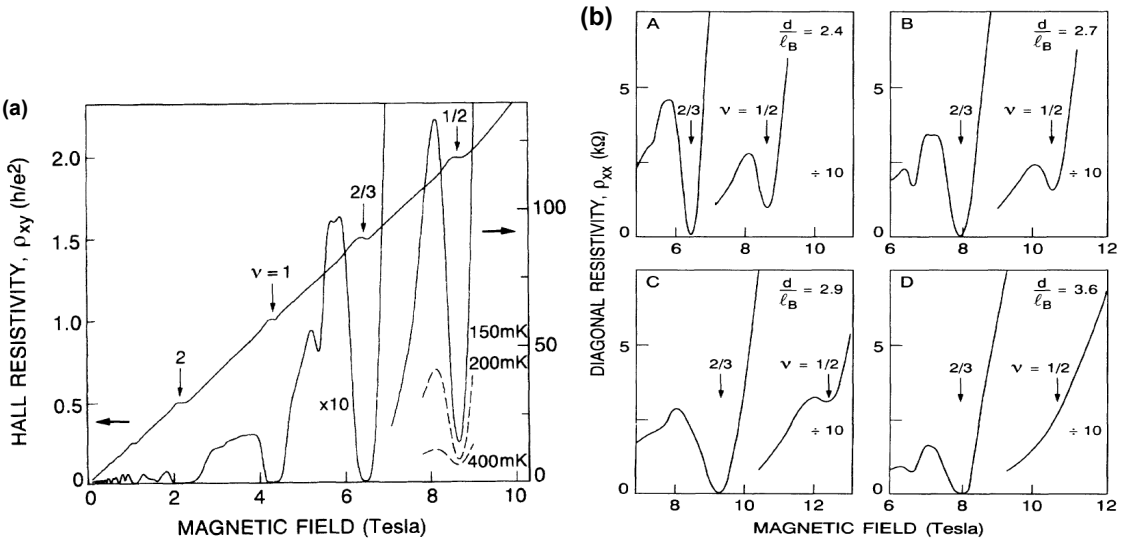

Figure 1.6: (a) Longitudinal and Hall resistivity vs magnetic field at 150 mK for Sample A, which is a GaAs/AlGaAs double quantum well with 18 nm wide wells separated by a 3.1 nm AlAs barrier and total electron density of 1.04×10^{11} cm^{-2}. Dashed curves are fragments of the ρ_{xx} curve around $\nu = 1/2$ at 200 and 400 mK. (b) Comparison of the longitudinal resistivity data for the four samples at $T = 300$mK. Note the weakening of the QHE signature with increasing d/ℓ. After Ref. [6].

1.4.1 The $\nu = 1/2$ QH state

In single layers, only fractional QH states with odd denominators are observed for $\nu < 2$. In bilayers, as a consequence of inter-layer Coulomb interactions, new QH states become possible, which have no analogue in single layers. A remarkable example is the $\nu = 1/2$ state, which clearly violates the odd denominator rule. It cannot be understood in terms of single layer energy gaps, because $\nu_{\uparrow(\downarrow)} = 1/4$. So the existence of this state is a pure manifestation of inter-layer interactions.

Experimental evidence for the 1/2 state was first reported by Eisenstein *et.al.* [6]. They studied the transport properties of four bilayer samples, named A, B, C and D, designed to have minimal tunneling ($\Delta_{SAS} < 0.9K$), but yet be coupled by Coulomb interactions.

The transport data at low temperatures for sample A are shown in Fig. 1.6(a). QHE signatures are observed at $\nu = 2, 1, 2/3$ and most importantly at $\nu = 1/2$. The deep minimum in ρ_{xx} at $\nu = 1/2$ becomes less sharp with increasing temperature, indicating the weakening of the QHE, as it should be.

In order to clarify the role of the inter-layer correlations in the formation of the 1/2 state, three other samples (Samples B, C and D) with increasing values of d/ℓ were studied. In Fig. 1.6(b) we can see a comparison of the longitudinal resistivity data at 300 mK for all four samples. First we focus on samples A, B and C that are structurally identical, but differ in their densities. While the $\nu = 2/3$ ρ_{xx} minima are almost similar for the three, the $\nu = 1/2$ feature weakens monotonically with increasing density. If the 1/2 state was of single layer origin, we would expect the opposite behaviour. In fact when density increases, we need a higher magnetic field to reach the same filling factor and since the Coulomb energy $e^2/\ell \propto \sqrt{B}$, the energy gap increases and there should be a stronger transport feature. Actually for bilayers the relative magnitude of intra-layer and inter-layer interactions plays a crucial role. We note that the increase in d/ℓ when going from Sample A to C, and hence the decrease of the relative importance of inter-layer interactions is concomitant to the weakening of the QH feature. Now we consider Sample

D, which has a nearly equal density to Sample B, but a thicker barrier and consequently a higher d/ℓ ratio. Again it exhibits a 2/3 QHE similar to the other samples, but the 1/2 feature is absent.

All these data show that the $\nu = 1/2$ QHE collapses as d/ℓ increases and provide compelling evidence that this new QHE derives from inter-layer correlations. This experiment also establishes an approximate critical value for the ratio $(d/\ell)_{cr} \approx 3.1$ above which the 1/2 state is destroyed.

1.4.2 The $\nu = 1$ Phase Diagram

The $\nu = 1$ state may seem less interesting at first thought. Although it has no counterpart in single layers ($\nu_{\uparrow(\downarrow)} = 1/2$), its gap can be of single particle origin. Indeed in the presence of tunneling, the lowest symmetric spin up LL is separated from higher levels by spin and pseudospin gaps, which can give rise to a QHE. Quite surprisingly the $\nu = 1$ state can also occur in the absence of tunneling if the layers are placed close enough. This indicates again the crucial role of inter-layer Coulomb interactions.

The first experiment emphasizing the impact of inter-layer correlations in the bilayer $\nu = 1$ QHE was conducted by Boebinger *et.al.* in 1990 [35], where bilayers with finite tunneling gaps were studied. However the first systematic study of the $\nu = 1$ QHE in bilayers was carried out in 1994 by Murphy *et.al.* [7].

In the experiment of Murphy *et.al.* 15 samples were studied and most of them consisted of two 18 nm wide GaAs wells separated by a 3.1 nm $Al_xGa_{1-x}As$ barrier. By changing the Al concentration in the barrier ($0.3 < x < 1.0$), the tunneling gap was varied between 0.5 and 8.5 K , while the total carrier concentration ranged from 0.8×10^{11} to 3.2×10^{11} cm^{-2}, with low temperature mobilities of $\sim 10^6$ cm^2/Vs. The samples are represented in Fig. 1.7(a) as a function of the tunneling gap Δ_{SAS}, normalized to the intra-layer Coulomb energy $e^2/\epsilon\ell$ and of d/ℓ at $\nu = 1$.

Transport data as a function of magnetic field were taken for all samples at T = 300 mK. In Fig. 1.7(b) we show the magnetic field dependence of ρ_{xx} for the samples indicated by numbers 1 and 2 in Fig. 1.7(a). While both display QHE at $\nu = 2, 4/5$ and $2/3$, they differ dramatically at $\nu = 1$. Sample 1 displays a strong QHE at $\nu = 1$, while in sample 2 there is no such effect. Similar analysis was performed on the other samples.

Two important qualitative conclusions can be drawn from the data: 1) there exists a well-defined boundary separating the QHE from the non-QHE phase; 2) the phase boundary intercepts the vertical axis at a non-zero value of d/ℓ (≈ 2). In fact the samples enclosed by the dashed curve in Fig. 1.7(a) have negligible tunneling ($\Delta_{SAS} < 1K$), but still they display a well-defined $\nu = 1$ QHE. We deduce that QH states exist in the limit of zero tunneling where they can only derive from inter-layer correlations. The phase transition that we see when moving from sample 1 to 2 cannot be accounted for by the competition between tunneling and interaction effects, because of the negligible value of the tunneling gap. It should be driven entirely by Coulomb effects. As the layers distance exceeds a critical value, the correlations between the two layers vanish and the system evolves into an uncorrelated gapless state, composed by two independent layers at $\nu_{\uparrow(\downarrow)} = 1/2$.

Finally the distribution of points in the phase diagram suggests that the QHE evolves continuously from a state dominated by single-particle tunneling (rightmost samples) to an intrinsically many-body state at $\Delta_{SAS}/(e^2/\epsilon\ell) \longrightarrow 0$.

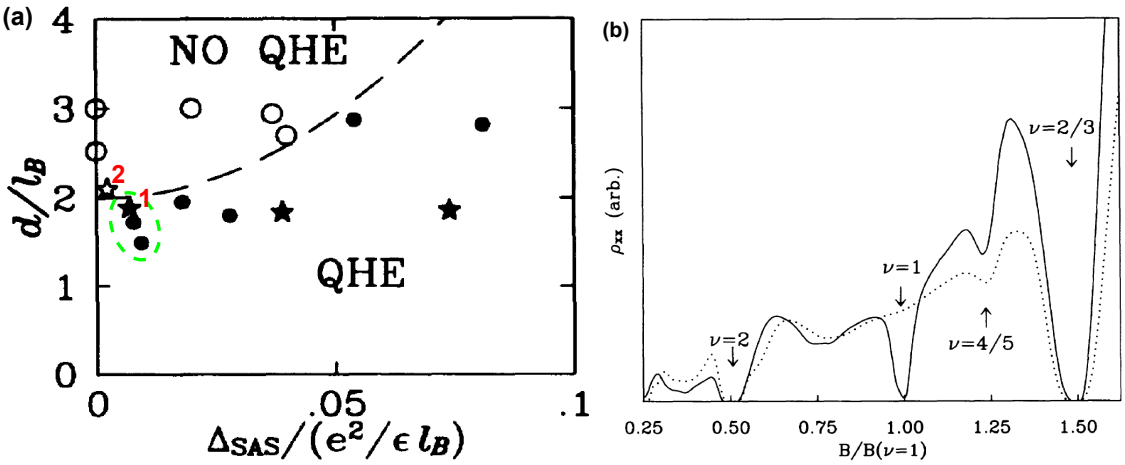

Figure 1.7: (a) 15 bilayer samples plotted according to their values of the tunneling gap and the inter-layer distance. Samples that exhibit QH signatures at $\nu = 1$ are presented by solid symbols in the diagram, while those that do not show the $\nu = 1$ QHE by open symbols. The dashed line estimates the location of the phase boundary. (b) Longitudinal resistivity data taken at 0.3 K for samples indicated in (a) by 1 (solid trace) and 2 (dashed trace). After Ref. [7].

1.4.3 Two-Component Wavefunctions

We have encountered two examples of two-component degrees of freedom : the spin and the layer, where the latter can be described in complete formal analogy to spin. We now explicitly write the two-component wavefunctions for QH bilayer states and discuss their properties. Being interested only in the pseudospin physics, we will assume the spin to be fully aligned and frozen.

In order to deal with QH spin systems, Halperin generalized the Laughlin orbital wavefunctions as :

$$\Phi_{m,m',n}[z] = \prod_{i<j\leq N_\uparrow} (z_i - z_j)^m \prod_{k<l\leq N_\downarrow} (z_{[k]} - z_{[l]})^{m'} \prod_{a=1}^{N_\uparrow}\prod_{b=1}^{N_\downarrow}(z_a - z_{[b]})^n \prod_{s=1}^{N} \exp\left(\frac{-|z_s|^2}{4}\right), \tag{1.7}$$

which are also suitable for treating pseudospin systems. In (1.7), $N_\uparrow$, $N_\downarrow$ represent the number of electrons in the top, bottom layer respectively, and the index $[i] \equiv N_\uparrow + i$. The total wavefunction is obtained by properly antisymmetrizing the orbital part given in 1.4.3.

In (1.7) electrons in the two wells are treated as distinguishable particles. While m and m' are forced to be odd integers by the Pauli principle, n can take on any value : odd, even or zero. The distinguishability picture breaks down if tunneling becomes relevant, because the pseudospin states of single electrons hybridize into symmetric and antisymmetric combinations of $|T\rangle$ and $|B\rangle$, so the $\Phi_{m,m',n}$ are strictly useful only in the limit $\Delta_{SAS} \to 0$.

The exponents (m, m') and n describe the intra-layer and inter-layer correlations respectively. In fact $\Phi_{m,m',n}$ excludes relative angular momenta less then m in the upper layer, less than m' in the bottom layer and less then n for electrons in opposite layers. Hence the electron organization described by $\Phi_{m,m',n}$ lowers the Coulomb energy by forcing electrons, either inside the single layers or in opposite ones ($n \neq 0$), to avoid each other.

Halperin wavefunctions are good approximations to the true ground state and they

Table 1.1: Some balanced Halperin states (m, m, n). τ is the total pseudospin and asterisks denote states that are not eigenstates of τ^2. Partial filling factors $\nu_{\uparrow(\downarrow)}$ are shown in parenthesis for the states with $m = n$, because they are not uniquely defined.

m	n	$\nu_{\uparrow(\downarrow)}$	ν	τ
1	0	1	2	0
1	1	(1/2)	1	$N/2$
3	0	1/3	2/3	*
3	1	1/4	1/2	*
3	2	1/5	2/5	0
3	3	(1/6)	1/3	$N/2$
5	0	1/5	2/5	*
5	1	1/6	1/3	*

display a charged excitation gap [37]. The presence of the charge-gap is important for two reasons : it guarantees that the system displays the QHE; it ensures that the presence of a small amount of tunneling between the layers doesn't invalidate this correlation picture.

The Halperin wavefunctions are explicitly constructed to be entirely in the lowest Landau level, so they are useful for QH states with $\nu \leq 2$. The individual layer filling factors can be read by counting the powers of z_1 and $z_{[1]}$ in $\Phi_{m,m',n}$, yielding:

$$\nu_\uparrow = \frac{m' - n}{mm' - n^2} \quad \text{and} \quad \nu_\downarrow = \frac{m - n}{mm' - n^2}. \tag{1.8}$$

The majority of experimental situations deal with balanced bilayers *i.e.* bilayer samples in which the two layers are equally occupied ($N_\uparrow = N_\downarrow$). These systems can be well described by Halperin states with $m = m'$. In Table 1.1 the partial and total filling factors are shown for some balanced Halperin states.

For $\nu = 1/2$ the only candidate is the $(3, 3, 1)$ state. Its intra-layer correlations are the same as for the Laughlin 1/3 state. We can crudely describe this state as two Laughlin 1/3 states locked with respect to each other such that electrons in one layer face correlation holes in the opposite one. The validity of this wavefunction is supported by numerical simulations [36, 37] .

At $\nu = 2/5$ there are two available candidate Halperin states. Numerical simulations [36] suggest that the QHE appears for all values of d/ℓ, but for $d/\ell < 2$ the $(3, 3, 2)$ wavefunction provides a better description of the system, while for $d/\ell > 2.5$ the $(5, 5, 0)$ state is more adequate. The idea is that for small separations inter-layer correlations are preferred, while at large separations the system evolves into two independent layers ($n = 0$) with $\nu = 1/5$. At intermediate values of d/ℓ we could have a phase transition between the two states, which should manifest itself in a significant change of the charged excitation gap, probably due to the different nature of charged excitations in the two states.

The $\nu = 2/3$ behaves similarly, in the sense that it should display a QHE at all values of d/ℓ, but in both single and independent layer regimes it is of single layer origin. In fact for $d \ll \ell$ the system is well described by a Laughlin 2/3 orbital wavefunction and a fully symmetric pseudospin (if $\Delta_{SAS} \neq 0$, all pseudospins align along the $+x$ direction). In the opposite limit, the $(3, 3, 0)$ is more appropriate, because it lacks inter-layer correlations ($n = 0$).

For $\nu = 1/3$ the Halperin $(3, 3, 3)$ is realized in the single layer limit, while the less correlated $(5, 5, 1)$ at intermediate d/ℓ values. Despite these results, the bilayer $\nu = 1/3$ QHE has never been reported experimentally to our knowledge.

Finally for $\nu = 1$, the $(1,1,1)$ state has a good overlap with the numerically exact ground state at small d/ℓ.

1.4.4 Spontaneous Symmetry Breaking

Let's inspect more carefully the Halperin (m,m,m) states. The orbital wavefunction is equivalent to the Laughlin function at $\nu = 1/m$ and it is completely antisymmetric, yielding a fully symmetric pseudospin function. This tells us that we have a fully aligned pseudoferromagnetic state with total pseudospin $\tau = N/2$. At the same time the partial filling factors in (1.8) are ill-defined, because of the vanishing denominator $mm' - n^2$. The anomaly follows naturally from the fact that corresponding to maximal total pseudospin, there are $2\tau + 1 = N + 1$ orthogonal states differing only by their τ^z quantum number.

In the single layer limit, the states of the $\tau = N/2$ multiplet are all degenerate. At finite layer separation, interactions become pseudospin dependent and the degeneracy is lifted. In fact $V_{ps}{}^2$ is a positive-definite operator, so it favours the states with $\langle \tau^z \rangle = 0$, for which pseudospin lies in the xy plane. Since τ^z measures the charge difference between the layers, the detachment of pseudospin from the xy plane can be viewed as a charging of the capacitor formed by the two layers and this explains why states with $\langle \tau^z \rangle \neq 0$ have a higher energy.

A state with full pseudospin polarization in the xy plane is referred to as *easy-plane* pseudospin *ferromagnet* and its wavefunction has a generic form given by :

$$|\Psi_\phi\rangle = \prod_X \frac{1}{\sqrt{2}} \left[c^\dagger_{X,T} + e^{i\phi} c^\dagger_{X,B} \right] |0\rangle, \tag{1.9}$$

where $|0\rangle$ is the electron vacuum, $c^\dagger_Q / c_Q$ is an operator that creates/destroys an electron with quantum numbers Q, and X is an index running through the orbitals of the lowest LL in the top and bottom layers. The global phase ϕ determines the orientation of the total pseudospin in the xy plane

$$\langle \Psi_\phi | \tau | \Psi_\phi \rangle = \frac{N}{2} \left(\hat{\mathbf{x}} \cos\phi + \hat{\mathbf{y}} \sin\phi \right).$$

All these states have the same lowest energy, so the ground state of the system is highly degenerate. These states are transformed into one another for rotations of the total pseudospin around the z axis, which is an expression of the $U(1)$ symmetry of the Coulomb interactions in bilayers (see end of section 1.4). However the system chooses a particular pseudospin orientation ϕ and it spontaneously breaks the $U(1)$ symmetry. In fact $|\Psi_\phi\rangle$ is a coherent superposition of all τ^z eigenstates, so that the layer charge difference is uncertain. The phenomenon is analogous to a BCS state that has an uncertain number of Cooper pairs, or to superfluid He. We say that the system has spontaneous inter-layer phase coherence.

At non-zero tunneling ($\Delta_{SAS} \neq 0$), pseudospins "prefer" to align along the $+x$ direction, so that the state of the system can be well approximated by $|\Psi_{\phi=0}\rangle$. In this case the symmetry is explicitely broken and the system lacks many of the interesting properties found in the case of $\Delta_{SAS} = 0$.

There is another suggestive way of viewing the states in (1.9). If we start with a vacuum state $|0'\rangle$ with no electrons in the bottom layer and no holes in the top layer (*i.e.* the top layer contains a fully filled LL), then the above wavefunctions can be rewritten as

[2] the pseudospin dependent part of the electron interaction, defined in (1.6)

$$|\Psi_\phi\rangle = \prod_X \frac{1}{\sqrt{2}} \left[1 + e^{i\phi} c^\dagger_{X,T} c_{X,B}\right] |0'\rangle. \tag{1.10}$$

The combination $c^\dagger_{X,T} c_{X,B}$ creates an inter-layer electron-hole pair, or equivalently an inter-layer exciton. In this formulation the $\nu = 1$ many-body wavefunction takes the same form of the BCS state for conventional superconductors, in which Cooper pairs are replaced by excitons.

Conventional excitonic states in insulators or semiconductors differ substantially from the ones introduced above [38]. In fact they are usually created by shining light on the crystal, which produces equal numbers of electrons in the conduction band and holes in the valence band that form bound states after relaxing into the extrema of the respective bands. However they represent highly excited states (with energy close to the bandgap) and spontaneously decay into the crystal ground state, usually by emitting photons. Their lifetime varies from ms to ns depending on the material. In contrast bilayer excitons at $\nu = 1$ are already present at equilibrium. The whole electron gas contributes to the formation of excitons and not just the few photoexcited particles. Furthermore they are perfectly stable particles with infinite lifetime. Bilayers of 2DEGs then host all the appropriate conditions for realizing the Bose-Einstein condensation of excitons.

We now address two important consequences of spontaneously broken symmetry in bilayers at $\nu = 1$, a rigorous derivation of which can be found in [11, 34]. The first concerns the low lying excitations of the system. Those are neutral pseudospin waves with linear dispersion $\omega \propto |\mathbf{q}|$ at long wavelengths and zero energy at $\mathbf{q} = 0$. They represent the Goldstone mode associated with the broken symmetry.

The second is related to the existence of dissipationless excitonic currents, analogous to the supercurrents observed in superconductors. If $\phi(\mathbf{r})$ is the spatial profile of the inter-layer phase associated with the excited state wavefunction, it can be demonstrated [11,34] that such excitonic currents can be expressed as :

$$J = \frac{2\rho_s}{\hbar} \nabla\phi,$$

where ρ_s is a pseudospin stiffness coefficient, related to the exchange energy cost of spatial variations of the pseudospin. Since excitons are composed of bound electrons and holes belonging to opposite layers, their uniform flow is equivalent to ordinary electrical currents flowing in opposite directions in the two layers. Therefore exciton supercurrents can be probed in a counterflow geometry, *i.e.* by applying electrical fields of opposite signs in the two layers.

1.4.5 Evidence of Spontaneous Inter-layer Phase Coherence

The observation of QHE at $\nu = 1$ in bilayers with $\Delta_{SAS} \approx 0$ indicates the paramount importance of inter-layer Coulomb correlation, but it does not reveal the existence of an exciton condensate.

Evidence for a broken symmetry phase comes from tunneling spectroscopy measurements, performed by Spielman *et.al.* [12] in a GaAs/AlGaAs double QW, where the layer densities can be varied by using top and bottom gates. In this way the various regimes of d/ℓ can be explored in a single sample. By contacting independently the two layers [39], the authors were able to apply a voltage difference V between the layers and measure the tunneling current I.

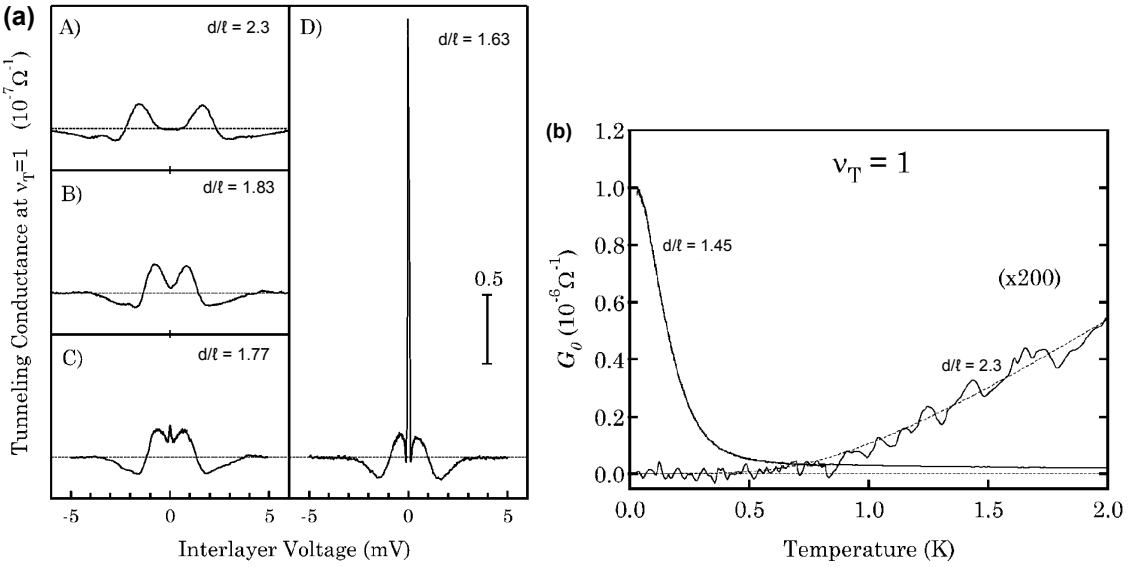

Figure 1.8: (a) Tunneling conductance dI/dV vs inter-layer voltage at $\nu = 1$ and $T = 40$mK in balanced bilayers with $\Delta_{SAS} \approx 0$. Each trace corresponds to a different total density (or effective layer separation d/ℓ) (b) Temperature dependence of the zero bias tunneling conductance at $\nu = 1$ for low and high effective layer separation. The latter data has been magnified by a factor of 200. After Ref. [12].

The tunneling conductance $(dI/dV - V)$ was measured at 40 mK and $\nu = 1$, for various values of d/ℓ. The central result is displayed in Fig. 1.8(a). At the largest d/ℓ, the zero bias tunneling is strongly suppressed. Then at $d/\ell = 1.77$ a small sharp peak appears at $V = 0$, which becomes the dominant feature of the spectrum at $d/\ell = 1.63$. The qualitative picture behind this data is the following :

For $d/\ell > 2$ there is no QHE and the layers are decoupled. Each layer behaves as a strongly correlated 2DEG with $\nu = 1/2$ described as a *composite fermion* metal [32]. Tunneling of one electron from one layer to the other costs an amount of energy $\Delta E \sim e^2/\epsilon\ell$, so the process becomes possible only at high voltages $eV = \Delta E$. In conclusion, the tunneling spectra display a Coulomb gap at zero bias.

At $d/\ell \approx 1.6$ the system displays the QHE and it is characterized by strong inter-layer correlations. Indeed in the $(1, 1, 1)$ state, electrons in one layer are opposite to holes in the other layer, so it seems plausible to get an enhancement of tunneling. Anyway this simple view cannot address the sharp resonant peak at $V \approx 0$. Such a feature suggests the existence of a gapless long-lived excitation of the system, which is capable of transferring charge between the layers. This is exactly what the pseudospin Goldstone mode does. In fact it involves oscillation of pseudospins in the z direction.

The collective nature of the tunneling process is supported by the temperature dependence of the conductance peak (see Fig. 1.8(b)). In fact in the non-correlated phase there is a monotonic increase, consistent with a thermally-activated excitation across the Coulomb gap. On the contrary, in the QH phase the peak decreases sharply for $T > 300$ mK, which reflects the thermal destruction of inter-layer correlations.

While suggesting the existence of a gapless Goldstone mode, fingerprint of a broken symmetry states, this result is not sufficient to demonstrate the exciton condensation. Evidences of exciton condensation were reported by Kellogg *et al.* [14] in a sample similar to the previous one.

By making independent electrical connections to the individual layers, they could inject

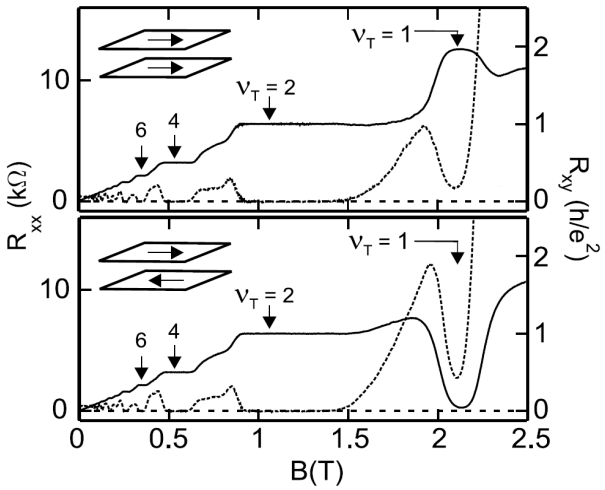

Figure 1.9: Hall and longitudinal resistances (solid and dotted traces respectively) for balanced bilayer at 50 mK for currents *in parallel* in the two layers (upper panel) and *in counterflow* configuration (lower panel). After Ref. [14].

currents in the layers in the same direction (parallel transport) or in opposite directions (counterflow transport) and measure the longitudinal and Hall voltage drops in the upper layer. At $\nu = 1$ and $d/\ell = 1.58$ (well within the QH phase, see Fig. 1.7) the longitudinal and Hall resistances at 50 mK are shown in Fig. 1.9(a).

In the case of parallel transport, the usual QHE signatures are seen around $\nu = 1$. The Hall plateau occurs at $2h/e^2$, because only half of the total current is measured. However in the counterflow configuration, there is a dramatic difference : the Hall resistance exhibits a deep local minimum. The idea is that dissipationless transport, associated with the exciton condensate, has infinite longitudinal conductivity, so both the longitudinal and Hall counterflow resistances should vanish. An even simpler picture is that excitons are neutral entities and do not experience the Lorentz force, so the Hall voltage must vanish.

Similar transport evidences were found almost simultaneously by Tutuc *et.al.* [15] and later by Tiemann *et.al.* [16] in a different sample geometry.

1.5 Conclusions

In this chapter we have examined some of the most remarkable phenomena that occur in cold 2DEGs in semiconductor heterostructures subjected to quantizing magnetic fields. In single layers, the combined effect of gaps in the electronic density of states and disorder leads to spectacular deviations from the classical transport behaviour, where the Hall resistivity instead of rising linearly with magnetic field, exhibits plateaus at values $h/(\nu e^2)$ with ν integer or odd-denominator fractions. For integer plateaus the gap is due to Landau quantization of the single particle kinetic energy. At fractional plateaus the electrons reorganize into correlated states with a gap dictated by the Coulomb interaction.

Bilayer systems enrich the scenario by bringing two new energy scales : the single particle tunneling gap and the Coulomb interaction between electrons in different layers. In concert they can either enhance or destroy the QHE, giving rise to phase diagrams for certain filling factors. Of particular interest is the case of bilayers coupled only by Coulomb interaction: they can exhibit QH states that have no analogue in single layers (at $\nu = 1$ and $1/2$) and they undergo quantum phase transitions with increasing layer separation. The $\nu = 1$ state involves a spontaneous symmetry breaking and it can be

pictured either as an easy-plane pseudospin ferromagnet or as a BCS like condensate of inter-layer excitons. Astonishing phenomena have been observed in this state, such as resonant enhancement of inter-layer tunneling at zero bias voltage and vanishing Hall resistance indicating dissipationless counterflow transport of inter-layer excitons.

The experiments discussed in this chapter were based on transport measurements. However there are at least two other classes of experimental tools that can be successfully employed for studying bilayers, namely nuclear magnetic resonance [40, 41] and optical spectroscopy, particularly inelastic light scattering [18–21]. In this thesis work we have decided to use photoluminescence(PL) spectroscopy with the target of highlighting the impact of inter-layer correlations and exploring new experimental evidences of bilayer QH states. There are several reasons for this experimental choice:

1) GaAs/AlGaAs heterostructures have enhanced optical properties, both because of intrinsic properties of GaAs and of the increasing precision of modern growth techniques. So these samples produce good quality optical signals, when optically probed.

2) Optical spectroscopy provides information complementary to transport experiments. In particular PL probes individually electrons in different spin/pseudospin states and can thus give information on the energies of these states and the distribution of electrons among them. This motivates our expectation of observing new properties of QH states, not seen in transport data.

3) In the last 25 years PL has been successfully employed for investigating single layers in the QH regime. Signatures of QH states and associated quasiparticle excitations have been found. Many important aspects of the experimental data are now theoretically well-understood. These results provide a useful and reassuring guideline, when dealing with bilayers.

4) The topic of photoluminescence in QH bilayers still represents an unexplored area. There have been very few experimental [42, 43] and almost no theoretical work on the argument. To this respect, the present work represents the first attempt to explore QH bilayers with the hope of opening a new route for the studies of this rich class of phenomena.

Chapter 2

Photoluminescence Spectroscopy and Experimental Setup

The modulation doping technique, able to suppress the scattering of electrons from the ionized donors, makes it possible to realize "clean" high mobility 2DEGs. In GaAs/AlGaAs heterostructures grown by MBE such systems display remarkable optical properties. In the following we briefly review the most relevant optical techniques exploited so far in the investigation of 2DEGs, with emphasis on bilayer samples.

Magneto-absorption spectroscopy relies on the ability to discriminate between occupied and unoccupied states around the Fermi level. In fact absorption can only occur into unoccupied states, so monitoring the absorption level while sweeping the Fermi energy can shed some light into the spin and pseudospin polarization of the various QH states. However these experiments are difficult to conduct. In particular the samples need further processing in order to remove the substrate which would otherwise absorb most of the light. In order to increase the absorption, typical samples include several replica of the QW. In this way, however, some disorder is introduced. In the experiments on bilayers, this would be detrimental, since it is difficult to realize identical copies of coupled bilayers. Indeed very few experiments have been reported on bilayers. We mention, in particular, the work by Manfra *et.al.* [17] on a coupled double layer at $\nu \approx 1$. They observed a loss of pseudospin polarization, which suggests an interplay between single-particle tunneling and inter-layer Coulomb effects.

Inelastic light scattering has been successfully employed in the study of QH bilayers. It provides access to the collective neutral excitations of the system. In particular the low lying spin excitations (spin-flips and spin waves) have proven very useful in probing the properties of QH bilayers at $\nu \approx 1$. For instance, it has been shown that the pseudospin polarization of the ground state can be deduced from the energies of these spin excitations, and a loss of pseudospin polarization was found in a coupled bilayer with a non-zero tunneling gap [19]. Phase transitions at $\nu = 1$ have been observed both in zero [20] and finite tunneling gap samples [21], which are signalled by dramatic changes in the nature of the spin-flip excitations seen in the light scattering spectra.

Finally, photoluminescence (PL) spectroscopy can be considered as the most straightforward optical technique. It consists in optically injecting an electron-hole pair into the sample, which probes the electron gas. The energies and intensities of the interband recombination channels of the 2DEG electrons with the photo-generated hole provide information on the ground state configuration of the 2DEG.

Magneto-PL has been extensively employed in the study of single layer 2DEGs. Inten-

sity modulations, energy non-linearities and line splittings in the optical spectra provide evidence for various integer [22] and fractional QH states [23–25]. These features have been linked to changes in the screening behaviour of the electron gas in the QH state. In addition, PL has proven to be a useful tool in studying the spin polarization of the 2DEG [23, 44] also in the fractional QH regime.

Considering the success of PL spectroscopy with single electron layers, there is little doubt that it can also be profitably used for studying electron bilayers. However, to our knowledge, there have been very few PL investigations of bilayer samples.

In the first part of this chapter we introduce the basics of PL spectroscopy and illustrate its application in the study of 2DEGs in the QH regime. The knowledge of the energy level structure of GaAs/AlGaAs QWs, with which we deal throughout this work, is essential for understanding their emission spectra, so we briefly describe the most relevant valence and conduction band levels of these samples. To illustrate the application of PL spectroscopy and its potentiality, we present some well-established experimental results on single layers, such as the polarization analysis of the PL spectra, optical signatures of the QH states and the role of the Hidden Symmetry in the optical emission. These results are also important for the understanding of the data from bilayer samples.

The second part of the chapter is dedicated to the description of the experimental equipment used in this work. Particular emphasis is placed on the cryogenic systems, that allow the achievement of mK temperatures, and on the optical setup used for the magneto-PL measurements.

2.1 Introduction to PL Spectroscopy

2.1.1 Energy Level Structure of GaAs/AlGaAs QWs

The understanding of the PL data is almost impossible without an apriori knowledge of the energy levels of the sample. In Chapter 1 we saw that the energy structure of the 2DEGs is driven by strong electron correlations, so we expect the electron states to be of collective nature. Anyway our knowledge of these correlated states is limited to particular filling factors, while we know almost exactly the evolution of the single particle levels. For this reason, in the following we will mainly refer to the single particle picture and include correlations effects only when needed.

The Landau level structure in the conduction band (CB) was discussed in the previous chapter. To understand optical spectroscopy, one needs to know the valence band (VB) energy structure as well. Figure 2.1 shows the evolution of the relevant VB and CB states from bulk GaAs to QWs at B = 0 and to QWs at finite magnetic fields.

In bulk GaAs the VB structure is composed of three bands (Fig. 2.1(a)) : the heavy hole(HH), light hole(LH) and split-off(SO) bands. Since $E_{SO} \approx 0.34$ eV, we can neglect the SO band in the description of the optical spectra. HH and LH bands have coincident (degenerate) maxima at the Γ point and dispersion around Γ is approximately parabolic with effective masses : $m_{HH} \approx 0.4\ m_e$ and $m_{LH} \approx 0.1\ m_e$. HH and LH differ by their angular momentum : HHs have $J = 3/2$, $J_z = \pm 3/2$[1], while for LHs $J = 3/2$, $J_z = \pm 1/2$. Each band is doubly degenerate in J_z. For the electron states in the CB, J and spin(S) coincide and we have $S = 1/2$, $S_z = \pm 1/2$.

The QW confinement brings important changes [26]. Electrons, HHs and LHs can still be described as freely moving particles in the QW plane, but the confinement in the well

[1] In bulk GaAs we choose $\hat{z} \parallel \mathbf{k}$, while in QWs it is convenient to choose $\hat{z}$ along the growth direction.

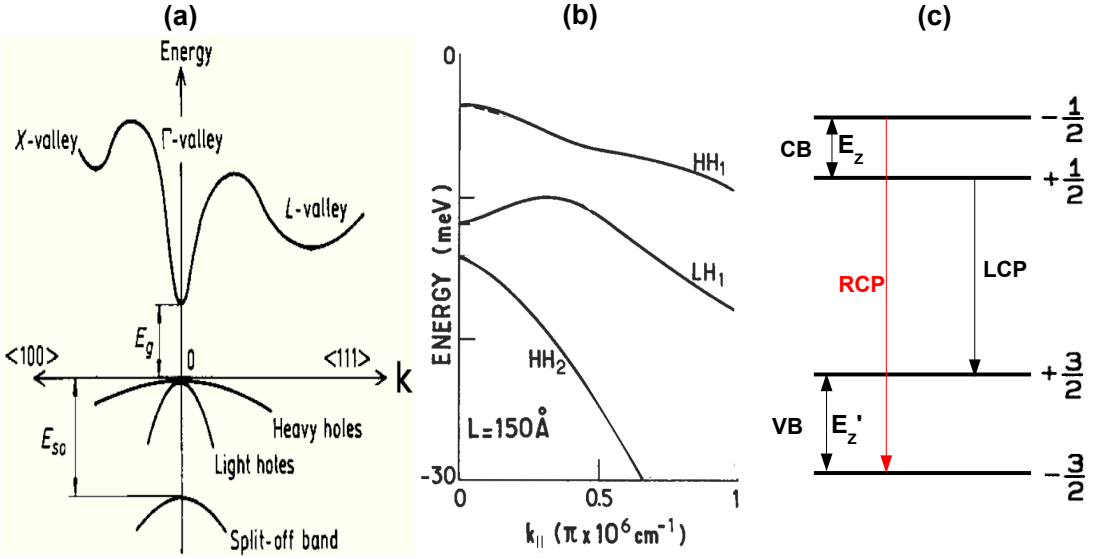

Figure 2.1: (a) Band structure of bulk GaAs (b) Calculated valence subband structure of a GaAs QW at $B = 0$, obtained by neglecting the coupling to the conduction band and assuming crystal inversion symmetry. Strong subband non-parabolicities can be noted. After Ref. [26]. (c) Lowest Landau levels originating from the lowest electron subband in the CB and HH1 subband in the VB. Optical transitions between the LLs connected by arrows, generate left(LCP) and right(RCP) circularly polarized photons. $E_{Z(Z')}$ are the Zeeman energies in the conduction (valence) band.

direction gives rise to energy subbands. Only the first subbands (n=0) for each type of hole will be considered, since the successive ones (n$\geq$ 1) are usually tens of meV lower in energy and do not contribute to the optical emission. If the heterostructure has inversion symmetry in the well direction, each subband remains doubly degenerate.

Since the confinement energy goes as $1/m^*$, then the Γ point degeneracy in the VB is lifted and the LH subband becomes lower in energy than the HH subband (see Fig. 2.1(b)). In magneto-PL experiments only the lowest energy emissions are studied, so recombination processes involving the HH only are typically considered.

The new hole states with in-plane momentum $\mathbf{k}_{||} \neq 0$ do not have a well-defined angular momentum, because the HH and LH states mix. Nevertheless, the amount of angular momentum mixing is generally quite small. For this reason we continue to label HH states with $J_z = \pm 3/2$ and LHs with $J_z = \pm 1/2$.

Summarizing, magneto-PL spectra in GaAs QWs can be understood in terms of HHs in the VB and electron states with mass m_c and $S = 1/2$ and $S_z = \pm 1/2$ in the CB. HHs can be considered approximately as free particles with an effective mass m_v and angular momentum $\pm 3/2$.

Finally, in a magnetic field the energy levels for the electrons and HHs take the form :

$$E_{n,s_z} = \hbar\omega_{c,c}(n + \frac{1}{2}) + g_e\mu_B B S_z, \quad \text{where} \quad \omega_{c,c} = \frac{eB}{m_c c}, \text{ and}$$
$$E_{m,J_z} = -\hbar\omega_{c,v}(m + \frac{1}{2}) + g_h\mu_B B J_z \quad \text{where} \quad \omega_{c,v} = \frac{eB}{m_v c}. \tag{2.1}$$

Since $m_v \approx 6m_c$, the Landau level energy spacing will be much lower in the VB than in the CB, so we expect Landau level mixing to be much more important for holes than for electrons.

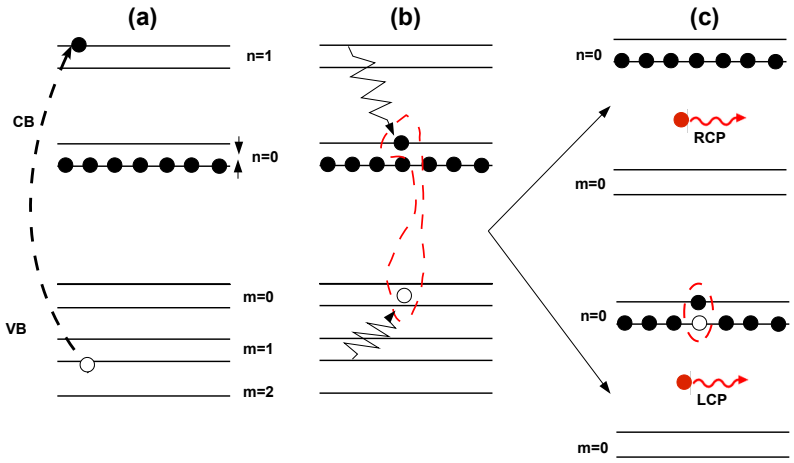

Figure 2.2: Schematic description of a PL process at $\nu = 1$: (a) Absorption of incident photons and generation of an electron-hole pair (b) Relaxation of the photogenerated particles. Both spin states of the $m = 0$ LL are possible for the hole (depicted in the middle of the spin up/down levels). The dashed closed loop represents the formation of a bound state between the encapsulated particles, while the full spin up LL acts as an inert background (c) Two possible recombination channels, yielding photons with orthogonal circular polarizations. In LCP emission a spin wave is left in the final state, which consists of a bound state between the reversed spin electron and the spin hole in the otherwise full Landau level.

2.1.2 Fundamentals of PL Spectroscopy

PL involves three consecutive processes : excitation, relaxation and spontaneous emission. Initially the system contains an unperturbed 2DEG. In Fig. 2.2 we illustrate the case of a 2DEG at $\nu = 1$, in which all the electrons occupy the lowest LL with spin up.

Let's assume that we excite the system by some external light source (laser), which pumps electrons from the valence to the conduction band, thus generating electron(e)-hole(h) pairs. Usually laser powers are kept very low, so that the number of pairs is much lower than that of electrons in the 2DEG. In this way the photo-generated electrons perturb very weakly the 2DEG and also the photo-generated holes are very diluted so we can safely neglect the interaction between them. In this picture, we only need to consider the evolution of the electron gas + one hole system. The effect of the hole on the surrounding gas is far from being trivial. In fact the $e-h$ and $e-e$ Coulomb interactions are of equal strength and should, therefore, be considered on equal footing. Some issues regarding the current understanding of the PL in single layers will be addressed in the following.

Soon after excitation, the 2DEG + h system is in a highly excited state, since the photogenerated e and h occupy higher-energy Landau levels. Because of the coupling with lattice vibrations or scattering with electrons of the gas these particles loose energy and rapidly (∼ps) relax non-radiatively towards the lowest available unoccupied states. In the situation depicted in Fig. 2.2(b), the photo-electron will relax to the spin down lowest LL ($n = 0$) in the CB and the hole to one of the spin resolved states of the "lowest" hole LL ($m = 0$) in the VB. Usually relaxation times are much faster than the $e-h$ recombination times (∼ns), so the system will be found either in its ground state $|i_g\rangle$ or in one of its lowest excited states $|i_e\rangle$. With increasing temperature the $|i_e\rangle$ become more populated and are expected to contribute more to the PL emission.

Finally the $e-h$ interband recombination leads to emission of a photon. PL spectroscopy is concerned with the collection and analysis of the emitted photons in order

to get information about the state of the 2DEG. The form of the PL spectrum can be expressed as :

$$I(E) = \sum_{i,f} P_i |\langle f|\mathcal{L}|i\rangle|^2 \delta(E_f - E_i - E), \tag{2.2}$$

where $I(E)$ represents the intensity of emission at energy E, $|i\rangle$ and $|f\rangle$ represent the states immediately before and after recombination, respectively, P_i is the occupation probability of state $|i\rangle$ before recombination and $\mathcal{L}$ is the dipole transition operator.

The first type of information that can be read from the spectra, is the energy of the emission peaks. It corresponds to the energy difference between the initial and final states involved in the emission. From the energy value and in particular its variation with magnetic field, we can infer about the nature of the initial state. If energy varies linearly, emission is expected to be of single particle origin, while deviations from this behaviour could be a signature of many-body effects, including excitonic effects.

Most importantly, the recombination of electrons from different spin-resolved Landau levels occurs at different energies, so in the PL spectrum we get a separate signature for each level, in contrast to transport measurements, where only the average response of the electron gas can be read from the data. Usually the Zeeman splitting is of the same magnitude as the emission linewidth and the spin states are typically not resolved in the spectra, except at very high magnetic fields. However the emissions from the two spin levels have orthogonal circular polarizations, as it can be seen in Fig. 2.1(c), so by detecting only certain polarization components we can probe separately the spin levels. The technique is called polarization-resolved PL spectroscopy and it provides information on the spin polarization of the system.

Another valuable information contained in the spectra is the emission intensity of the various peaks. Intuitively one could relate the intensity variation of a peak to a variation in the population of the corresponding electron level. Actually, from (2.2) we learn that the intensity of the peaks is determined by the simultaneous action of three physical variables : the stationary population P_i of the initial luminescence states, that is also influenced by the absorption cross section of the exciting radiation, and it also depends on the various relaxation and decay times ; the optical transition matrix element, which is governed by the overlap integral of the e and h wavefunctions, and varies under the influence of localization in the disorder potential; the density of states, in which gaps are opened in correspondence to QH plateaus. Therefore one has to be cautious when interpreting the intensity behaviour and complementary evidence is often required to support the assigned interpretation.

2.2 PL in the QH Regime

2.2.1 PL in Single Layers

We review here some representative magneto-PL data obtained in single layers. In particular we start by illustrating the main ideas and potentialities of the polarization-resolved PL, which we have also adopted in our study of bilayers. Next we present the features of the optical spectra that signal the formation of QH states in single layers, and their physical meaning. The QHE in single layers is usually associated with minima in the emission intensity, which are also observed in our PL spectra of bilayers at particular filling factor values. We also explain that two-dimensional $e + h$ systems under high magnetic fields manifest an internal symmetry, called Hidden Symmetry (HS), due to the equality of

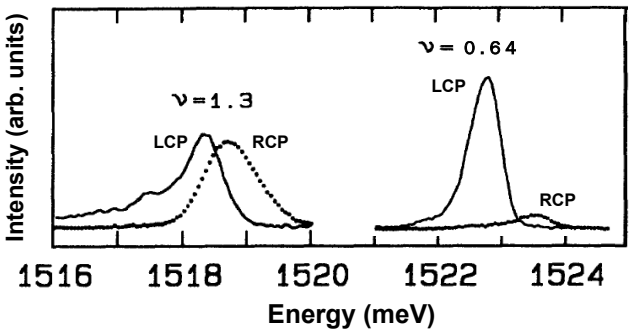

Figure 2.3: Emission spectra of a 25 nm wide QW at 0.56 K, hosting a 2DEG with density 1.83×10^{11} cm^{-2}. Solid/dotted lines correspond to left/right circularly polarized emission spectra at two different filling factors (indicated in the figure). After Ref. [23].

strength of $e-e$, $e-h$ and $h-h$ interactions. In the last part of this section we introduce the HS, its consequences and limits of validity.

Polarization resolved PL

Polarization analysis of the optical emission from a 2DEG discriminates the separate contributions of the spin-split states of the lowest LL. This follows from the fact that electrons in the two spin states recombine with HHs by emitting photons of opposite circular polarizations, as shown in Fig. 2.1.

Polarization-resolved luminescence spectroscopy was initially exploited by Goldberg *et.al.* [23] to probe 2DEGs in GaAs/AlGaAs QWs at high magnetic fields. Figure 2.3 displays representative examples of two circularly polarized emission spectra. The depopulation of the upper spin state for $\nu < 1$ causes the RCP emission to be strongly suppressed. In addition, by comparing the anomalies in the LCP and RCP emission energies at $\nu = 1$, Goldberg *et.al.* could determine the relative impact of many-body effects[2], that depend differently on the initial occupancy of the spin states.

Measurement of the polarized emission offers the possibility to determine directly the spin polarization of the 2DEG. This was demonstrated by Kukushkin *et.al.* [44] in a GaAs/AlGaAs heterojunction, hosting a 2DEG. By analysing the intensities of the LCP and RCP emissions, they could quantitatively estimate the variation of the 2DEG spin polarization around $\nu = 1$.

QHE in the PL spectra

In transport measurements, the QHE appears as plateaus in the Hall resistivity and deep minima in the longitudinal resistivity. Signatures in the PL spectra that have been observed, are : plateaus in the recombination energy, peak shifts, minima in the emission intensity and line splittings.

PL signatures of the QHE at $\nu = 1, 2/3$ and $2/5$ were observed by Goldberg *et.al.* [24]. They measured simultaneously the transport resistivity components and the PL spectra of a high-mobility 2DEG, hosted in a GaAs/AlGaAs QW, at different temperatures. Figure 2.4 shows the experimental data around $\nu = 1$, where plateaus in the emission energy and intensity minima can be noticed. The extent of the R_{xy} plateau delimits the magnetic field interval over which the Fermi energy E_F lies in a region of localized states. As the

[2] such as the screening of the hole potential, the $e-h$ Coulomb binding and the $e-e$ Coulomb and exchange interactions

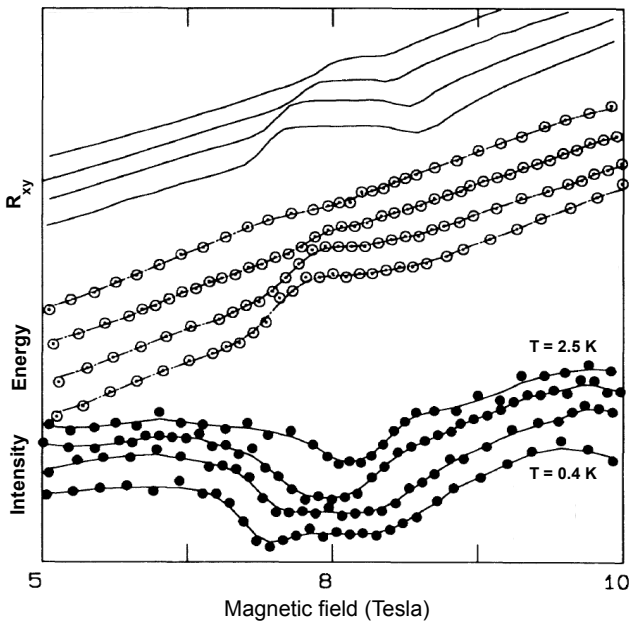

Figure 2.4: Transition energy (circled dots), peak intensity (solid dots) and Hall resistance R_{xy} (solid lines) around $\nu = 1$ at T = 2.5, 1.3, 0.6, and 0.41 K, for a sample nominally identical to the one in Fig. 2.3. The energy curves are offset by 0.5 meV each, and the intensity and R_{xy} curves by arbitrary constant values, for better visibility. After Ref. [24].

temperature is reduced, fewer extended states lie within k_BT from E_F, causing the Hall plateau width to increase. The similar behaviour of the transport Hall plateau and the optical intensity minimum and energy plateau, upon cooling of the 2DEG, indicates their common physical origin *i.e.* the position of E_F inside the localized states region. A similar correspondence between optical and transport features was also observed at $\nu = 2/3$ (not shown here).

While only specific fractional QH states are usually seen in the PL spectra of 2DEGs, the work of Byszewski *et.al.* [25] reported signatures of a whole set of fractional QH states, which are symmetric around $\nu = 1/2$. In particular energy blue shifts and line splittings were observed at filling factors $\nu = 1,\ 2/3,\ 3/5,\ 3/7,\ 2/5$ and $1/3$. The jumps in energy were seen in correspondence to the edges of Hall plateaus and they gradually disappeared with increasing temperature.

The quenching of the lowest energy emission at $\nu = 1$ and $2/3$ [23, 24] is currently understood as a consequence of the localization of e and h in the disorder potential of the 2DEG. We recall, in fact, that the charged excitations of a 2DEG in a QH state are gapped, so that electrons are unable to screen external potentials. Thus the residual potential fluctuations that originate from the ionized donors and the well-width fluctuations can localize e and h quasiparticles. Because of their opposite charge, e and h are confined in different regions of space. Hence their wavefunction overlap and the optical matrix element is reduced, leading to a suppression of the optical emission. This interpretation is supported by time-resolved PL investigations of doped QWs, which revealed a large increase in the radiative recombination time at $\nu = 1$ [45].

The changes in the screening response of the 2DEG are also thought to be responsible of the upward cusps (or energy blue shifts) observed in the PL peak energy evolutions [23–25].

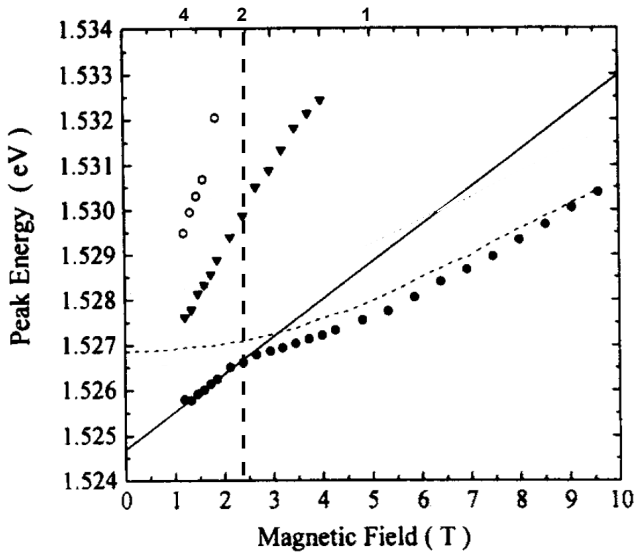

Figure 2.5: Luminescence peak energies as a function of magnetic field for a 20 nm wide symmetric QW, containing 1.2×10^{11} electrons/cm^2 at 4.2 K. The solid line is the best linear fit to the lowest emission energy at low fields, while the dotted line represents the peak energy at low electron density. Filling factors are shown in the upper axis, while the position of $\nu = 2$ is also indicated by the dashed vertical line. After Ref. [46].

Hidden symmetry

The magneto-luminescence spectra of symmetric quantum wells containing a high density ($\gtrsim 10^{11}$ cm^{-2}) electron gas show an abrupt changeover from Landau-level behaviour (i.e. linear shift of energy with magnetic field) to approximately quadratic behaviour (exciton-like), at electron filling factor $\nu = 2$. Figure 2.5 illustrates the phenomenon (at the dashed vertical line). The data have been published by Yoon *et.al.* [46]. At $\nu < 2$, the emission energy follows the transition energy observed in the same sample at low electron density to less than 0.5 meV, so the energy depends weakly on the gas density. The changeover is not observed in wide (width > 25 nm) asymmetric QWs.

Based on these observations, Rashba and Struge [47] argued that the changeover is a consequence of the *Hidden Symmetry* (HS), inherent in 2DEGs in strong magnetic fields. If we mapped the $e - h$ system into a spin-1/2 electron system, then HS would simply correspond to the invariance of Coulomb interactions under spin rotation [48]. The validity of the HS requires that Coulomb interactions are charge-symmetric $V_{ee} = V_{hh} = -V_{eh}$ and that e and h have identical wavefunctions. These conditions are realized if : a) particles(e, h) have the same wavefunction in the growth direction b) B is sufficiently large, that we can neglect the LL mixing c) all carriers are in the lowest LL.

In an ideal system, where a) and b) are satisfied, condition c) is equivalent to $\nu < 2$. Let's consider an ideal gas of N electrons with $\nu < 2$ in the presence of a photogenerated electron-hole pair. The ground state of the system is a product of the wavefunction of a neutral magneto-exciton (ME) and the wavefunction of the background gas of the N electrons. Because of the HS, both the ME wavefunction and the energy of the system are the same as if the well was empty ($N = 0$) [47]. In other words, the energy doesn't change if we add or remove an electron from the background gas.

This picture explains coherently the above mentioned experimental observations : the emission energy varies quadratically, because it originates from an exciton and it doesn't depend on the gas density because of the HS. The changeover occurs at $\nu = 2$, in corre-

spondence to the onset of the HS. Finally, in wide asymmetric QWs e and h can lie in different places along the QW growth axis. Hence condition a) and the HS are not valid, which explains the fact that the changeover is not observed.

The ideal picture implies also that the PL spectra contain a single line for $\nu < 2$, resulting from the radiative decay of a ME, and give no information about $e-e$ correlations in the 2DEG. The behaviour of real samples, however, deviates from the ideal model, because of the violation of the HS. In the following, we present two mechanisms through which the HS is violated and their consequences on the 2DEG luminescence.

1) The magnetic field is finite in realistic conditions, so condition b) is never fully satisfied. In real samples condition b) quantifies in:

$$\gamma \equiv \hbar\omega_c/Ry \gg 1,$$

where $Ry = \frac{m^* e^4}{2\hbar^2 c^2 \epsilon^2} \approx 4.8$ meV is the effective Rydberg energy for excitons in bulk GaAs, and $m*^{-1} = m_c^{-1} + m_v^{-1}$ is the reduced electron-HH mass. Actually the manifestation of the HS at $\nu = 2$ is so robust that it has been observed for γ as low as 0.5 [46].

At finite magnetic fields, the ME can bind an additional e and form negatively charged excitons X^-, which interact weakly with the surrounding 2DEG. The possible states of X^- are classified according to its spin and angular momentum : $X_S^-, X_{TB}^-, X_{TD}^-$ and X_{SD}^-, called singlet, bright triplet, dark triplet and dark singlet respectively. Charged excitons dominate the luminescence spectrum of 2DEGs at low and intermediate gas densities ($< 10^{11}$ cm^{-2}) and have been extensively studied theoretically [49] and experimentally [50–52].

2) The ideal model does not take into account the disorder potential and the carrier localization. As we have seen before, localization becomes important in the QH phase and gives rise to specific optical anomalies, such as intensity minima and energy jumps.

2.2.2 PL in QH bilayers

Little work has been done on the PL of double layers in the QH regime.

One of the first reports by Pellegrini *et.al.* [42] on the polarized inter-band recombination in single and symmetric double layers hosted in GaAs/AlGaAs QWs, showed the appearance of a new peak in the spectra of the double QW, whose intensity was enhanced for $\nu \approx 1$. This peak was interpreted as a signature of the pseudospin degree of freedom and its behaviour suggested a loss of pseudospin polarization for $\nu \approx 1$. We will see later that our studies corroborate this interpretation.

A recently published work [43] focused on the physics of a symmetric GaAs/AlGaAs double layer with tunneling gap at integer filling factors $\nu \gtrsim 2$. The authors observed anomalies in the polarization-resolved PL spectra, which were tentatively attributed to the many-body induced formation of a charge density wave at $\nu = 3$.

Other PL experiments were carried-out in doped asymmetric double QWs [53, 54], which are however less interesting for our purposes, since this samples lack many of the interesting properties discussed in Chapter 1.

This brief review reveals the lack of PL investigations in QH bilayers with $\Delta_{SAS} = 0$ and in bilayers with $\Delta_{SAS} \neq 0$ in the fractional QH regime ($\nu < 1$).

2.3 Experimental Setup

2.3.1 Low Temperature Systems

Transport experiments on bilayers suggest that the remarkable inter-layer correlated phases in the QH regime require temperatures below 1 K. In our work we achieved temperatures in this range by using two different fridges : a ^{3}*He fridge* for the transport measurements and a *dilution fridge* for the magneto-luminescence experiments. In the following we introduce the basic features that are common to both fridges and then describe the most important details of each of them.

The central unit of most fridges is a low boiling point liquid (the refrigerant) and their ability to cool is related to the phenomenon of evaporative cooling. Basically only the most energetic molecules are able to leave the liquid surface, so during evaporation the liquid looses energy. This is described by the latent heat of vaporization per atom l. Without external action, an equilibrium is established between the liquid and its vapour, in which the system temperature and the vapour pressure remain constant. The relation between the two quantities is well approximated by the Clausius-Clapeyron relation:

$$P = P_0 \exp\left(-\frac{l}{kT}\right), \tag{2.3}$$

where P is the vapour pressure at temperature T and P_0 is a material dependent constant. This formula tells us that we should reduce the vapour pressure in order to lower the temperature. In fact the fridges that we will consider are supplied with pumps, that continuously remove the evaporated fluid. A natural low temperature limit for all fridges is the freezing point of its refrigerant. The only elements that we know to remain liquid even at absolute zero are ^{3}He and ^{4}He. But there is another important limitation that stems from (2.3). In fact a good pump is able to remove a constant volume of gas per unit time. But with decreasing pressure, the same volume corresponds to a smaller number of removed molecules, which at steady conditions means a smaller number of molecules evaporating from the liquid. Then (2.3) says that the evaporating rate decreases exponentially with the lowering of temperature and so will the cooling power of the pump. This will ultimately limit the system from going to absolute zero.

In fact with a ^{4}He refrigerant, we cannot go lower than 1 K. In practice ^{4}He fridges are used to cool down to 2.2 K (lambda point fridge), because at lower temperatures a large amount of ^{4}He ($> 30\%$) will need to be evaporated to cool the remaining liquid. Anyway a small ^{4}He recipient cooled at 1K is often used in other fridges to condense the refrigerant. The unit is called "1K Pot". It needs to be continuously fed with ^{4}He from a reservoir and the input rate is controlled by a needle valve.

^{3}He has a lower normal boiling point (3.2 K) then ^{4}He (4.2 K) so it can reach a lower base temperature of T $\lesssim$ 0.3 K .

In order to decrease further the base temperature, we need to overcome the limit posed by (2.3). This can be achieved by using a mixture of ^{3}He/^{4}He. The properties of the mixture as a function of temperature and ^{3}He concentration were studied intensively in the period 1950-70 and an interesting phase diagram, shown in Fig. 2.6, was found. When the temperature decreases below 0.86 K, the mixture can separate into two distinct phases : the ^{3}He rich phase (aka concentrated phase) which floats above the heavier ^{4}He rich phase (aka dilute phase). The properties of the two liquids are governed by quantum mechanics, but for our purposes the concentrated phase may be considered as liquid ^{3}He and the dilute one as ^{3}He gas. The picture is valid if the ^{3}He concentration of the mixture

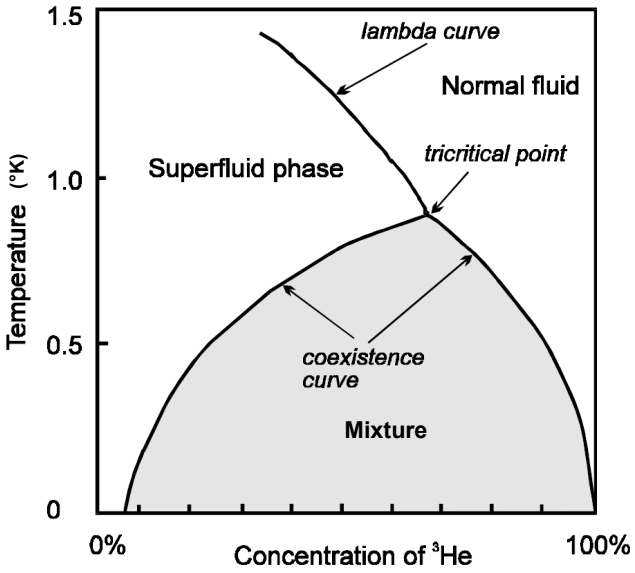

Figure 2.6: Phase diagram of ^{3}He/^{4}He mixtures.

is below 20%. ^{3}He has a lower entropy in the concentrated phase, so when it 'evaporates' from the concentrated to the dilute phase, heat is subtracted from the system. If we keep the system inside the mixture phase (light gray area in Fig. 2.6), then even at absolute zero the 'gas' concentration doesn't decrease below 6.6% (see the left intercept of the coexistence curve at T = 0 K in Fig. 2.6). Thus cooling will continue at the lowest temperatures without loss of efficiency. The base temperature for dilution fridges is typically $5 - 30$ mK and it is limited only by imperfections in the fridge design.

Such low temperatures would be impossible to obtain in the presence of the large heat load coming from the environment. That's why both the fridges used in our experiments are hosted in big bath cryostats, that act as an efficient thermal shield. Figure 2.9 illustrates the schematic design of a bath cryostat, used in our experiment. We can distinguish three successive cooling steps. Clearly the outermost surface is in thermal contact to the environment at $T \approx 300$K. Going inside the cryostat we encounter a nitrogen jacket, filled with liquid nitrogen (LN_2) at 77 K and covers almost the entire surface of the inner part of the cryostat. Further in, we find the main bath which is basically a reservoir of liquid Helium (LHe) at 4.2 K. The three steps are separated from each other by vacuum chambers. The removal of matter drastically reduces the conduction and convection heat exchange between the various steps. Most importantly, the cold surfaces of the cryogen reservoirs reduce the amount of radiation heat load, which goes as the fourth power of the surface temperature (Stefan-Boltzmann law). Finally the innermost part of the cryostat contains the fridge insert, which can be removed to change the samples, and it is separated by a vacuum chamber from the main bath.

For measurements in the QH regime, it is fundamental to have a stable and homogeneous high magnetic field source. To this end, our cryostats are fitted with superconducting magnets. In our case the magnet is a solenoid formed by the winding of kilometres of superconducting wires made of both NbTi and Nb_3Sn. The solenoid is immersed in the LHe of the main bath at the height of the sample (see Fig. 2.9). At 4.2 K it can provide magnetic fields up to 12 T. The peculiarity of superconducting magnets is their ability to operate in persistent mode : once the current in the solenoid has been raised to the desired value, the superconducting circuit is closed to form a continuous loop. Because of

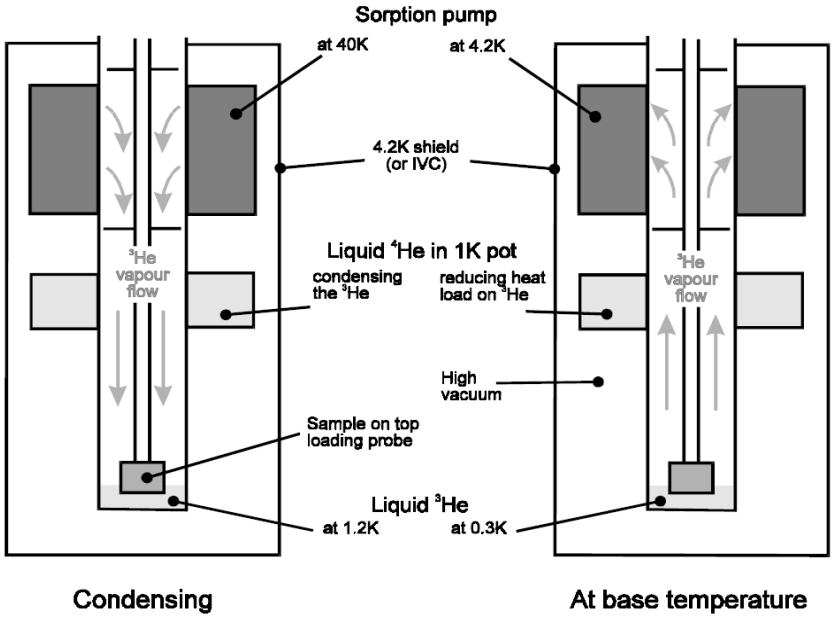

Figure 2.7: Schematic diagram illustrating the principle of operation of the ^{3}He fridge during condensation of the refrigerant and at base temperature. After Ref. [55].

the negligible resistance, the current decays slowly with a relative rate of 0.01% per hour. Therefore the only consumption comes from the LHe required for cooling the solenoid. The magnet can provide a relative field homogeneity of 0.1% in a spherical volume of 1 cm diameter around the sample.

We now briefly describe the specific working principles of the two fridges used in this work.

^{3}He Refrigerator

For transport measurements a temperature of 200 - 300 mK is sufficient. To this end we have used an Oxford Heliox^{TM}TL system. It is designed for routine operation in the range 0.3 to 1.2 K by using ^{3}He as refrigerant.

The fridge consists of an insert (see Fig. 2.7), inside a LHe cryostat, that contains a sorption pump, a 1K pot and the ^{3}He pot filled with refrigerant. The sorption pump(sorb) is a vacuum pump, that works by adsorbing gas and it can be controlled by changing its temperature. When it is warmed up, it releases the gas while, when cooled, it pumps the gas to a pressure that depends on the temperature. The pump is fitted with a heater and it can also exchange heat with the main bath. With this combination, temperature can be varied in the range 4.2 to 40 K. What makes this fridge special is the top loading probe, which can be inserted or removed quickly (for changing the sample) through the central access of the insert while this last one remains cold. The sample is mounted on the probe, which is then loaded directly onto the ^{3}He pot. The probe permits also an easy wiring connection to the sample.

During condensation, the sorb is warmed above 40 K, so it desorbs all the gas. ^{3}He condenses on the 1K pot assembly and runs down to cool the sample and the ^{3}He pot. At the end of this stage the ^{3}He pot is full of liquid at 1.2 K. The sorb is then cooled and it begins to reduce the ^{3}He vapour pressure, so the liquid is cooled and with it also the sample. With the sorb cooled at 4.2 K, the fridge can reach a base temperature of 260

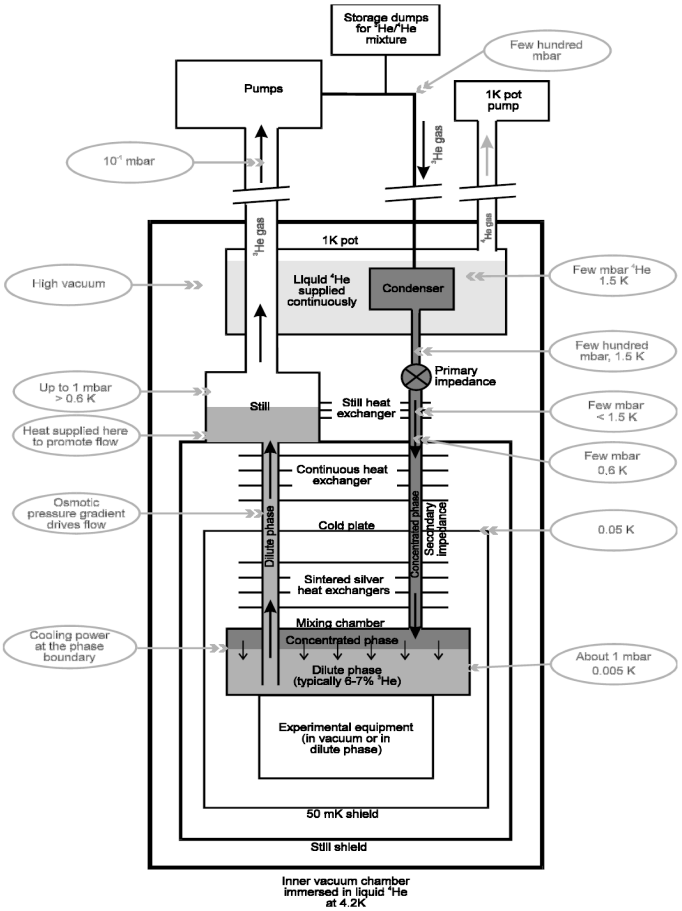

Figure 2.8: Schematic design of a dilution fridge. After Ref. [55].

mK. Any other temperature in between 260 mK and 1.2 K can be adjusted, by controlling the sorb temperature. The fridge works in a 'single shot' mode, which means that the evaporated refrigerant is not replaced, so operation will continue until the small initial amount of refrigerant has been completely pumped. Ideally it can provide an operation time at base temperature of nearly 50 hours.

Dilution Fridge

In order to fully appreciate the optical properties of the correlated states in bilayers, temperatures well below 0.3 K are desirable. For this purpose, we used an Oxford Kelvinox 400 HA system for our magneto-luminescence experiments. This is a dilution fridge, designed to operate stably in the range 0.05 to 1 K and equipped with optical windows for direct access to the sample. A schematic design is shown in Fig. 2.8. We describe its operation at base temperature ($\approx$ 50 mK).

The unit of the fridge where the lowest temperatures are realized, is the mixing chamber (M/C). It contains the ^{3}He/^{4}He mixture, separated into two phases with the concentrated phase floating above the heavier dilute one. There are two lines starting from this unit, that allow the continuous flow of the mixture.

The pumping line originates from the dilute phase. The liquid in this phase goes up to the still and during the process its temperature is raised to 0.6 - 0.7 K. At this temperature the ^{3}He vapour pressure is 1000 times larger than that of ^{4}He, so ^{3}He evaporates preferentially. The vapour is pumped away from the surface of the still. It follows that

the ^{3}He concentration in the remaining liquid becomes lower and the osmotic pressure difference drives a flow of ^{3}He from the M/C. This mechanism guarantees that in stationary conditions ^{3}He atoms will continuously cross the phase boundary (in the M/C) and hence supply a continuous cooling power.

Now the pumped mixture will have to return to the concentrated phase to close the cycle. Before doing so, it is passed through a series of filters and cold traps which remove the impurities, returned to the cryostat, where it is precooled in the main bath, and finally it enters the condenser line. The 1K pot liquefies the mixture and cools it to 1.2 K. During its way to the M/C, the mixture is further cooled down by the still and the dilute liquid flowing upwards to the still. It is important for the fridge operation to choose the mixture (its volume and ^{3}He concentration) in such a way that the phase separation occurs inside the M/C and the liquid surface is in the still.

The M/C can reach temperatures as low as 6-7 mK. Anyway the sample is not directly attached to it, but it is mounted on a sample holder, connected to the M/C by a copper rod. Copper is a good but not perfect conductor, so there will be a natural temperature rise from its M/C extremum to the sample holder.

Another limitation is related to the fact that our fridge is designed for optical spectroscopy. Therefore it is provided with a series of windows at the bottom of the cryostat as illustrated in Fig. 2.9, which allow optical access to the sample. The windows are made of a synthetic silica (Spectrosil) with high transmission in the visible range[3], which effectively cuts out the unwanted thermal radiation in the near-mid infrared. The outermost window isolates the cryostat from the environment and must be vacuum tight. Being at room temperature, it would introduce considerable radiation heat load at the sample. The latter is reduced in a stepwise fashion, by placing three other windows, each of which is thermally anchored to a cryostat cooling unit (LN_2 jacket, LHe main bath and the still shield). Finally the windows do not affect the light polarization, so they are suitable for polarization-resolved spectroscopy. The laser exciting radiation and also the residual thermal radiation transmitted from the cryostat windows will inevitably heat the sample. The working temperature on the sample is typically around 50 mK.

2.3.2 Optical Setup

The experimental setup for PL measurements is fairly simple. Figure 2.9 gives a schematic picture of the setup arrangement.

The excitation light is generated by a Ti:sapphire laser (Coherent, MBR-110), optically pumped by a 5W solid state (Nd:$YV0_4$ crystal) green laser (Coherent, Verdi 5, 532). The laser works in single mode, with a narrow linewidth $< \mu$eV and it is tunable in the range 780 - 870 nm, with a peak emission power of 350 mW. The single mode operation is achieved by forcing the unidirectional operation inside the ring cavity and also by a servo-locked intra-cavity thin etalon.

A polarization rotator, placed immediately after the laser output head, transforms the laser light polarization from horizontal to vertical. In this way, reflections of the laser light that eventually reach the spectrometer, would be rejected, since the spectrometer only "accepts" linear horizontal polarizations. Otherwise the intense laser reflections would cause excess noise in the detector.

The excitation power is controlled by a series of filters : the first ones have transmissions of $10^{-2}, 10^{-1}, 10^{-0.5}$ and realize a coarse adjustment of the power, while the circular

[3]including the spectral interval 790 - 820 nm of interest in our measurements.

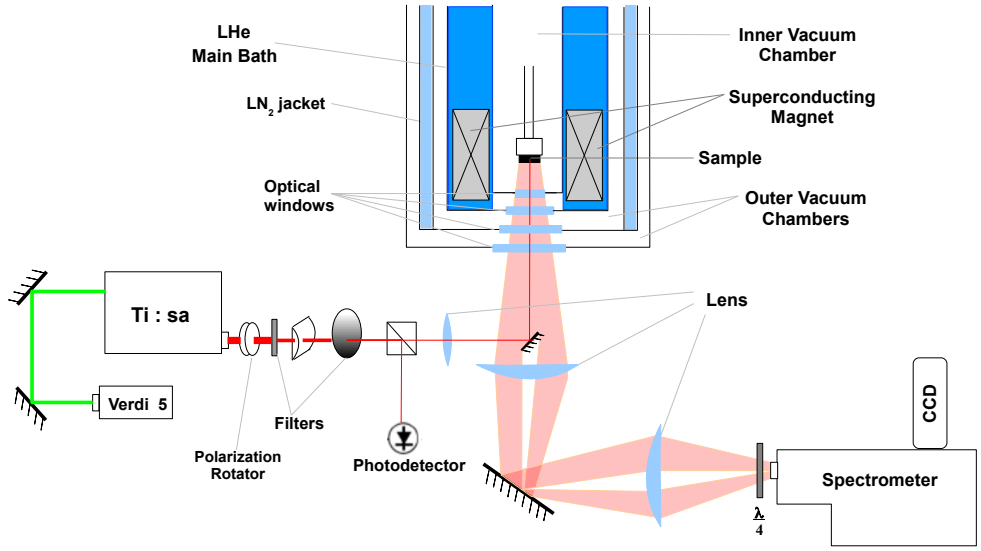

Figure 2.9: Schematic of the optical setup, showing also the relevant constituents of the LHe cryostat. The delivery line can be seen on the left of the cryostat, while the collection line on the right

variable filter allows a fine control. The power fluctuations are continuously monitored by drawing some of the radiation from the delivery line (through a 50:50 beam splitter) and sending it to a Si powermeter. The estimated power at the sample is 0.1 μW and the relative fluctuations are kept below 1%.

The spectrometer entrance slits have a rectangular shape, so an efficient coupling with the emitted light requires the illuminated area on the sample to have a similar shape. To this end, the laser beam is passed through a cylindrical lens that transforms the initial circular spot into an ellipse.

A biconvex lens focuses the beam to a 1 mm $\times$ 0.1 mm spot and its position is calculated so that the laser beam has its focal spot at the sample. The estimated incident intensity is $\sim 10^{-4}$ W/cm^2, a value that represents a compromise between the intensity of the emitted signal and the heating of the electron gas. Finally a 1.5 cm diameter mirror sends the beam up to the sample. The mirror dimension is chosen in such a way that it can efficiently block the reflections of the laser beam (from the optical windows, the metallic sample holder, the sample itself) which are undesirable in the detector, but at the same time it only blocks a small portion of the PL signal.

The collection line starts immediately under the delivery mirror and consists of a lens-mirror-lens. Each of these elements has a large diameter (9-10 cm) in order to collect the largest possible amount of signal which is focused by the last lens into the entrance slits of the spectrometer.

We employ a Jobin-Yvon T64000, which is basically a triple Czerny-Turner spectrometer, containing three master diffraction gratings with 1800 grooves/mm. The grooves are horizontally oriented, which brings two important implications : the spectrometer can detect horizontally polarized light only, and the size of the image on the sensor and thus the wavelength resolution is determined by the horizontal slit, while the vertical one simply influences the intensity. We use openings of 40 $\times$ 100μm. The spectrometer can be operated either in additive or subtractive mode. In the first case, which is the one we adopt in our experiments, all the three gratings are used, maximizing the instrument's spectral resolution, but minimizing the spectral window (4 nm in our case). In the subtractive mode only two gratings are used to diffract the light, so it provides less resolution in a

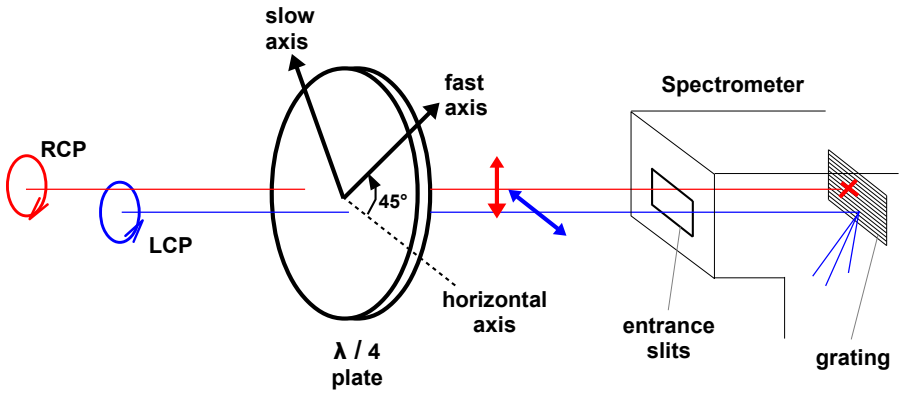

Figure 2.10: Working principle of the setup used for polarization-resolved PL. The quarter wave-plate transforms the polarization of the emitted light from circular to linear, while the internal gratings of the spectrometer "accept" horizontally polarized signals only.

larger spectral window ($\approx$ 12 nm).

After the spectral components of the signal are spatially separated, light is directed into a Charge-Coupled Device (CCD) sensor. It consists of a 2D array of Si MOS capacitors (pixels). Different spectral components will hit into different pixels, that accumulate a charge proportional to the impinging light intensity. The electronics reads out the pixel matrix and in the end it produces the desired intensity vs wavelength spectrum. In order to reduce the electronic thermal noise, the CCD is cooled with LN_2. The combined resolution of the detecting system, at 40 μm of slit opening, is of the order of 10^{-5} eV.

Polarization-resolved spectroscopy can be carried-out by simply placing a quarter wave-plate in front of the detecting system. If the fast-axis is oriented at 45° with respect to the horizontal direction as in Fig. 2.10, then the left/right circular polarization will be transformed into horizontal/vertical linear polarization, thus only the left component will be detected. Similarly, at 135° we can probe the right circularly polarized emission.

2.3.3 Transport Measurements

For the electrical characterization of the samples, we used a Van der Pauw geometry, shown in Fig. 2.11. It consists in placing four metallic electrodes (Ohmic contacts) at the perimeter of the sample (of arbitrary shape) and it is much easier to realize than the standard Hall bar geometry. The correct usage of this geometry requires five conditions to be satisfied : 1) The sample should have a flat area of uniform thickness 2) It shouldn't contain isolated holes 3) It should be homogeneous and isotropic 4) All four contacts should be placed at the edges of the sample 5) The average diameter of each contact should be much smaller than the distance between the contacts.

In our case samples were cut into rectangular pieces and the Ohmic contacts were placed at the corners. The mm^2 area of the contacts was defined lithographically, Au/Ge/Ni alloy was evaporated on this area and then thermally diffused to contact the 2DEGs.

The sample was mounted on the top loading probe of a ^{3}He fridge, equipped with a 12 T superconducting magnet. The four contacts, labeled 1,2,3 and 4 as in Fig. 2.11, were connected to a Lock-in Amplifier. The internal oscillator of the Lock-in Amplifier generates a 17 Hz current, which is injected through contacts 1 and 2 (I_{12}). Small currents $\sim \mu A$ are preferred to avoid strong perturbations of the 2DEG and we work with AC signals in order to reduce the flicker noise. The lock-in amplifier measures the voltage across the contacts 3 and 4 (V_{34}), basically by combining homodyne detection with an extremely low

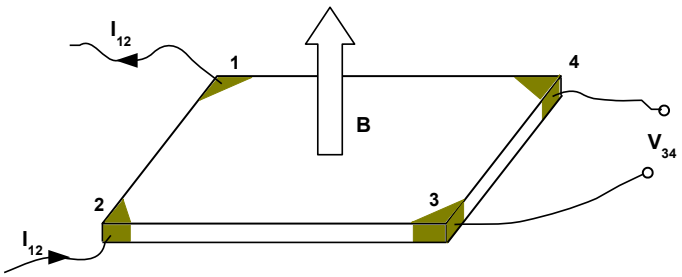

Figure 2.11: Schematics of the Van der Pauw geometry used for transport measurements. The wide arrow represents the applied magnetic field.

pass filter. In [56] it was shown that the ratio V_{34}/I_{12} is proportional to the longitudinal resistance $R_s \equiv \rho/d$, with a proportionality constant that depends on the shape of the sample and the relative position of the contacts.

Once we reach the desired temperature, the magnetic field is swept in the interval 0 - 10 T with a 2 mT step and for each value of the field the ratio V_{34}/I_{12} is measured. In this way we can analyse the behaviour of the longitudinal resistance with magnetic field and locate the position of the QH states (vanishing R_s).

Acquisitions were done with the sample both in dark or under illumination. In dark conditions we analysed the QHE of the unperturbed sample. Anyway during optical measurements the laser generates electron-hole pairs, which can modify the conductivity of the sample. The purpose of illuminating the sample is to simulate the experimental conditions during optical measurements. To this end we used a GaAs LED, driven by a 10 mA current. When the sample is at 4 K, the LED is turned on for 2-3 minutes. The time is sufficient for the sample to reach the persistent photo-conductivity mode. This is a particular regime, when the photogenerated carriers exist for a long time after excitation. In III-V semiconductor structures relaxation times of hours have been reported, which cover our entire measuring time. So there is no need to keep the sample illuminated during the magnetic field scanning and the LED is switched-off.

Chapter 3

Photoluminescence from the Sample with Tunneling Gap

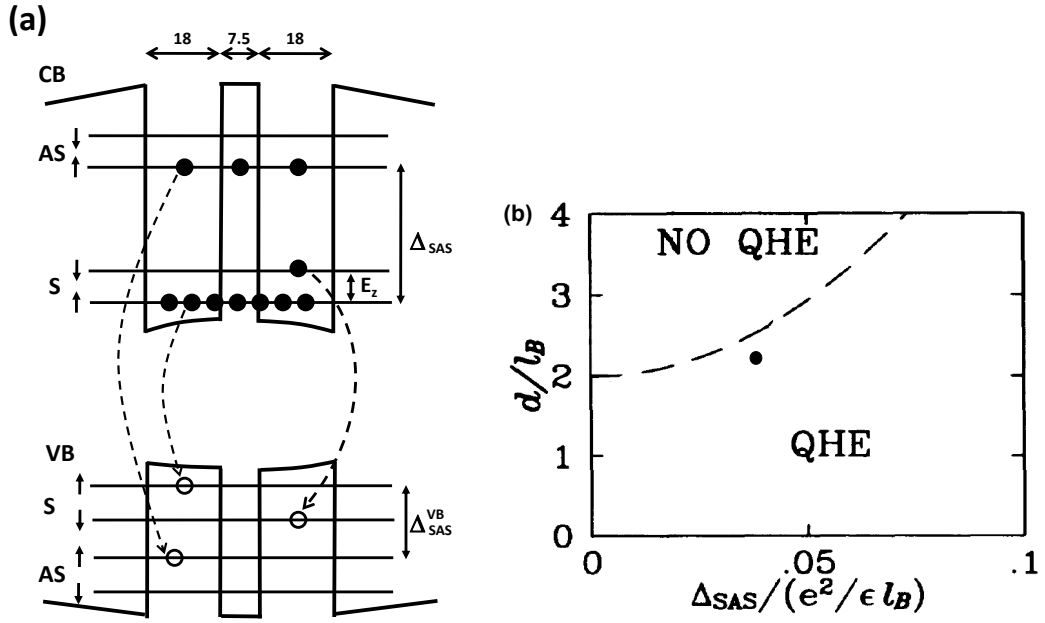

Figure 3.1: (a) Conduction(CB) and valence(VB) band-edge profiles along the growth axis, for the sample with tunneling gap. On the top, the widths of the wells and the intermediate barrier are given in nm. The single particle symmetric (S) and antisymmetric (AS) levels of the lowest Landau level are shown. E_Z and Δ_{SAS} stand for the Zeeman and tunneling gap energy, respectively. Small arrows represent the orientation of the spins with respect to the magnetic field, while dashed arrows indicate the relevant interband recombinations. (b) Phase diagram for the $\nu = 1$ QHE in bilayers, as obtained from [7]. The filled circle indicates the position of our sample in the phase diagram.

This chapter deals with the presentation and analysis of the experimental data from the bilayer sample with a finite tunneling gap. The choice of starting from this sample is due to the fact that its optical spectra are better understood and they provide a useful guideline for discussing the data from the other sample with zero tunneling gap.

A schematic illustration of the sample and its relevant energy levels is given in Fig. 3.1(a). It is a modulation doped GaAs/$Al_{0.1}Ga_{0.9}As$ symmetric double quantum well, grown by molecular beam epitaxy. Both the side and central barriers are made of $Al_{0.1}Ga_{0.9}As$. The low Al concentration allows to minimize alloy-disorder and thus leads

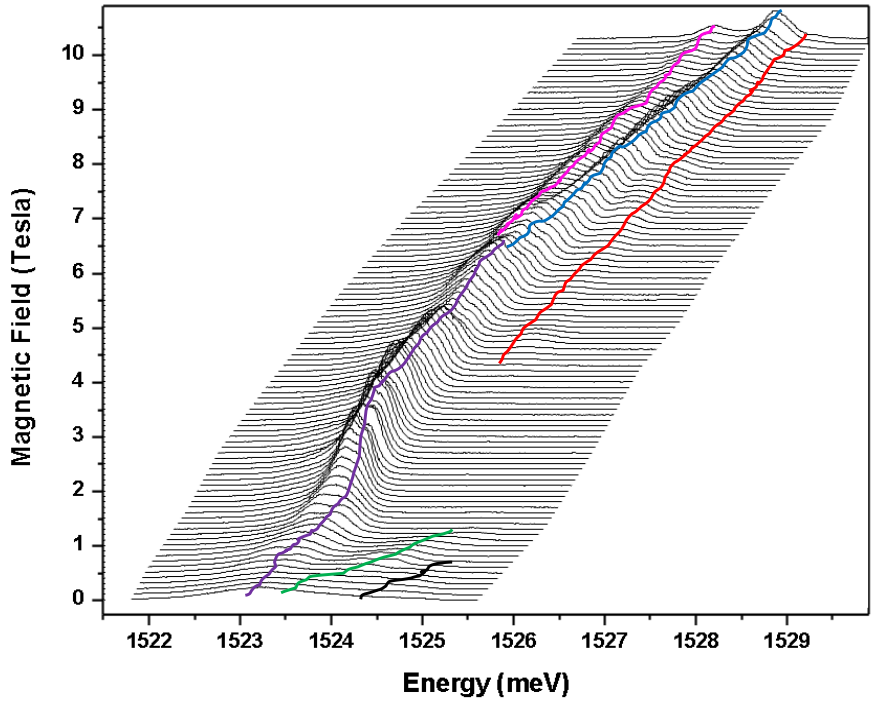

Figure 3.2: Left circularly polarized optical spectra in the magnetic field range from 0 to 10.4 T, taken at T = 50 mK with an excitation wavelength of 795 nm. Coloured lines are guides to the eye that follow the evolution of the various peaks. The spectra are vertically shifted for clarity.

to sharp optical emission lines. The electron gas has a total density of 1.1×10^{11} cm^{-2}, divided equally between the wells, and electron mobility above 10^6 cm^2/Vs. Measurements of the CB tunneling gap at zero magnetic field give $\Delta_{SAS} = 0.36$ meV [19]. For $B < 15$ T, the Zeeman splitting remains lower than 0.36 meV, so the proposed ordering of the single particle CB levels is appropriate.

At $\nu = 1$, we have $d/\ell \approx 2.18$ and $\Delta_{SAS}/(e^2/\epsilon\ell) \approx 0.038$, where d = 7.5 + 18 = 25.5 nm is the inter-layer distance. The sample's position in the phase diagram of the QHE at $\nu = 1$ is shown in Fig. 3.1(b). The sample is situated below the boundary, so it should exhibit the QHE at $\nu = 1$ at sufficiently low temperatures.

3.1 Introduction to the Data and Peaks Identification

We measure the PL spectra in the magnetic field range 0 - 10.4 T, with a 0.1 T step, while keeping the sample at 50 mK and the laser excitation line at $\lambda = 795$ nm. The estimated incident power density on the sample is $\sim 10^{-4}$ W/cm^2, which allows us to get good optical signals with 300 seconds of integration time per acquisition, while keeping the electron gas temperature as close as possible to the lowest accessible value. A stack plot of all the PL spectra in LCP polarization is shown in Fig. 3.2.

The spectrum at B = 0 T is shown in Fig. 3.3(a). It consists of a single wide asymmetric line, characteristic of emission from the 2DEG. To understand this point, we should consider that in the absence of external fields electrons in the CB fill the (spin degenerate) symmetric and antisymmetric subbands up to the Fermi energy E_F, as shown in Fig. 3.3(b). The photo-excited holes have $\mathbf{k}_{\|} \neq 0$, so before relaxing to the top of the VB, they can recombine with all electrons in the CB. Therefore we expect an emission width

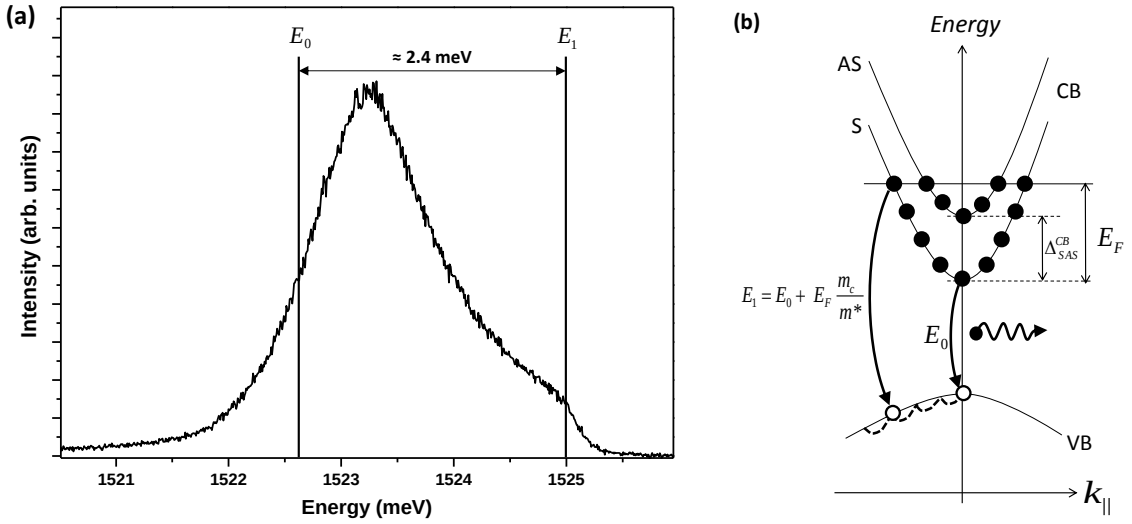

Figure 3.3: (a) Plot of the 0 T spectrum, taken in the same conditions as in Fig. 3.2 (b) Schematic of the energy level diagram of the sample at B = 0 T. The relaxation transitions of the photoexcited HH in the VB are labelled with short dashed curves. The curved arrows represent the interband recombinations of minimum (E_0) and maximum (E_1) energy.

of $E_1 - E_0 = E_F \frac{m_c}{m^*}$, where m_c is the effective electron mass in the CB and m^* is the reduced electron-HH mass *i.e.* $m*^{-1} = m_c^{-1} + m_v^{-1}$.

Using the nominal electron gas density n, we can derive the Fermi energy from :

$$D\Delta_{SAS} + 2D(E_F - \Delta_{SAS}) = n,$$

where $D = m_c/\pi\hbar^2$ is the areal density of states in the CB. We find $E_F = 2.2$ meV, which confirms the occupation of both S and AS subbands, and gives an emission width of $\approx$ 2.5 meV. The value measured in the spectrum of Fig. 3.3(a) is 2.4 $\pm$ 0.1 meV, compatible with that derived from the nominal density value.

When we increase the magnetic field, the initial PL line starts to split into different lines. For B $<$ 1.6 T, three peaks can be noted, whose energies shift almost linearly with the magnetic field. The higher the energy of the peaks, the lower the magnetic field at which they disappear. We attribute these emissions to the recombination of electrons and/or holes from higher Landau levels, which are occupied at such low fields.

The remaining lowest-energy peak evolves continuously until 5.5 T, where it splits into two lines, whose energy difference monotonically increases with B. A new emission peak at higher energy appears at 4 T.

To identify the origin of the emission lines, it is useful to plot their peak energies versus magnetic field. In a significant fraction of the spectra, however, the emission lines have an energy separation comparable to their linewidth. It is therefore impossible to determine the energies, intensities and linewidths of the peaks by reading directly the raw spectra. This analysis requires a fitting procedure.

Figure 3.4 illustrates a representative fit performed on the spectrum at 6 T. Clearly Gaussian peaks reproduce the spectrum better than Lorentzians, so they have been used to fit all the other spectra. The procedure produces also the standard errors associated with the energies and amplitudes of the peaks. However, the fitting errors of the peak energies are always below 30 μeV, lower than the instrumental spectral resolution of 70 μeV. In the following energy plots a fixed error bar of 70 μeV should be associated to all

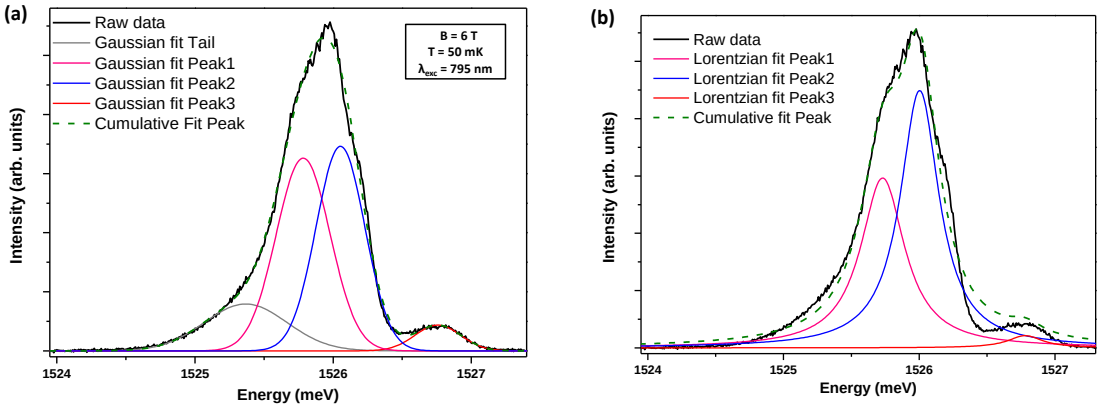

Figure 3.4: Best fit of the 6 T spectrum in Fig. 3.2 with four Gaussian (a) and three Lorentzian (b) lines. The colors refer to the peaks in Fig. 3.2. Gaussian lines fit the whole spectrum quite well, while Lorentzians fail to reproduce the high energy part. Note also that the additional gray peak in (a) is necessary for reproducing the low energy tail of the spectrum, while in (b) the tail is marginally reproduced by the high intensity wings of the Lorentzians and an additional peak would deteriorate further the quality of the fit.

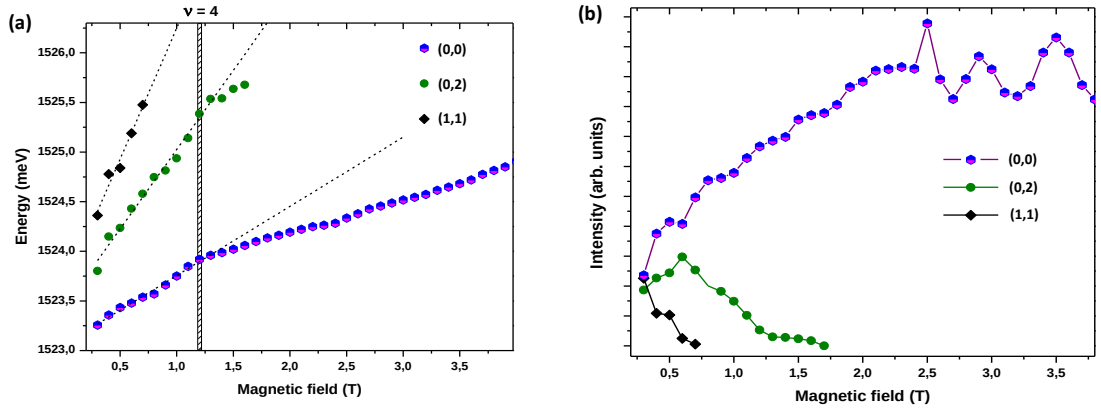

Figure 3.5: Peak energies (a) and integrated intensities (b) for the three emission lines at low magnetic fields B $<$ 4 T, obtained from the Gaussian fits of the spectra in Fig. 3.2. In the legend, (n,m) indicates a line resulting from recombination of electrons and HHs that reside in the n-th and m-th LL, respectively. In (a) dashed lines are linear fits to the energy curves. The vertical strip in (a) indicates the position and magnetic field width of the $\nu = 4$ QH state as obtained from the transport measurements.

points, so we have omitted it. For the amplitude data, we have verified that the relative errors are of the order of 0.1 %, therefore cannot be represented in the intensity plots.

3.1.1 Low Magnetic Field Sector

Figure 3.5 displays the magnetic field dependence of the peak energies and intensities of the three peaks observed at low fields. The energy plot confirms the linear dependence on B and linear fits have been performed to obtain the slopes, leading to 1.00 ± 0.02, 1.60 ± 0.06 and 2.65 ± 0.03 meV/T for the magenta, green and black peaks, respectively (see Figs. 3.2 and 3.5).

We recall that if an electron from the n-th LL recombines with a hole from the m-th LL, the emission energy in the single particle picture, neglecting spin effects, is :

$$E_{(n,m)} = E_0 + 2\mu_B B \left[\frac{m_e}{m_c} \left(n + \frac{1}{2} \right) + \frac{m_e}{m_v} \left(m + \frac{1}{2} \right) \right], \tag{3.1}$$

where E_0 is the emission energy at $B = 0$ and m_e is the electron mass in vacuum. In the following we will use the notation (n,m) for these transitions. Ideally (n,m≠n) transitions are forbidden, but in the presence of impurities and/or interface roughness of the QW they could be observed.

We assume that the lowest emission originates from the recombination of electrons and holes both in the lowest LL (0,0). Then from (3.1), using $m_c = 0.067\ m_e$ and the slope value of 1 meV/T, we get $m_v \approx 0.38 m_e$, consistent with reported values for the HH mass in GaAs/AlGaAs QWs, that vary in the interval 0.3 - 0.4 m_e [26].

We can now analyse the remaining peaks : the slopes of the green and black peaks are compatible with the transitions (0,2) and (1,1) respectively. In Fig. 3.5(b) we note that the intensities of these two lines vanish above a certain magnetic field. This is because they both involve electrons and/or holes from higher LLs, which are depopulated at sufficiently high fields.

A peculiar aspect of the energy data in Fig. 3.5(a) is the abrupt change in the B dependence of the (0,0) line[1] from linear to quadratic around $\nu = 4$. The natural interpretation is that for $\nu > 4$ the emission results from the recombination of non-interacting $e - h$ pairs, while for $\nu < 4$ the sample enters a regime in which bound complexes (excitons) are formed, whose energy depends quadratically on B.

A widely accepted mechanism that governs the transition between the two regimes is the hidden symmetry (HS) explained in the previous chapter. Emission becomes excitonic when the HS is valid and changes to single-particle like when it is broken. The validity of the HS requires the charge symmetry of Coulomb interactions. We argue that this condition is satisfied in our sample. In fact, the sample is completely symmetric, with the two wells being nominally identical in the geometric parameters, electron density and distance from the donors. In addition the wells are moderately narrow (18 nm). These facts guarantee that in each well electrons and holes have similar wavefunction profiles in the QW growth direction, so that Coulomb interactions are charge-symmetric.

Surprisingly, the filling factor where the transition occurs is doubled with respect to single-layer samples. The effect has never been observed before and we argue that it is a consequence of the pseudospin degree of freedom. In fact the validity of HS requires both e and h to be in the lowest LL, so that their in-plane wavefunctions are identical. In single 2DEGs each LL consists of two opposite spin sublevels, while in bilayer systems

[1] the (0,2) line displays similar behaviour, but the evidence is less convincing because of the absence of points for B ≤ 1.8 T

four sublevels are present because of the additional pseudospin degree of freedom. So the condition of being in the lowest LL translates into $\nu \leq 4$ in bilayers.

Actually one needs to be cautious when dealing with pseudospin, because Coulomb interactions are pseudospin dependent. A priori it is not obvious that the HS argument, derived for single component electron gases, can be straightforwardly generalised for two-component gases. Further theoretical investigation is needed to clarify the issue. However our data suggest the validity of the HS argument. In fact it is difficult to imagine other mechanisms that produce such a changeover in the energy dependence exactly at $\nu = 4$.

3.1.2 High Magnetic Field Sector

Let's now concentrate on the high-field region B $\geq$ 5.5 T, where we expect only the m=0, n=0 levels to be populated. In this region, three main emission peaks are observed, indicated in magenta, blue, and red lines in Figs. 3.2 and 3.4.

A crucial tool for understanding the physical origin of the observed peaks is the polarization analysis. As Fig. 3.6(a) makes clear, the recombination of spin-up electrons (s_z = +1/2), either from the symmetric or the antisymmetric level, results in the emission of photons with LCP polarization. Similarly, spin-down electrons recombine by emitting RCP polarized photons. In this picture, polarized spectra should consist of two lines at most, whose energies change by $E_Z = g_{eff}\mu_B B$ from the LCP to the RCP spectra.

Spectra at 6 T, in both polarizations, are shown in Fig. 3.6(b). We find the same number of peaks, at the *same energy positions*, with different relative intensities. At this field, the Zeeman splitting with $g_{eff} \approx 1$ is $E_Z \approx 1 * 0.058 * 6 = 0.35$ meV and it should be resolvable in the spectra. Thus if there was a shift of the peaks from the LCP to the RCP spectra, it would be clearly visible.

These observations, on the contrary, suggest that the interband transitions do not produce 100 % circularly polarized photons, as they should according to Fig. 3.6(a). We believe that this behaviour derives from the HH-LH mixing effects in the VB. For instance, if a HH in the state $\alpha|+3/2\rangle + \beta|+1/2\rangle$ recombines with an electron having $s_z = +1/2$, both LCP and linearly polarized photons will be emitted, with the same energies. Since we assume that HHs are involved in all the observed emission lines, the mixing mechanism explains also the observation of partial polarization in the whole explored magnetic field range.

We notice that the intensities of all the lines change significantly (by at least a factor of two) from the LCP to the RCP spectra. This means that, despite the mixing, the optical emissions preserve some dominant polarization character. The latter should be the same as in the absence of mixing and can still be understood from the simplified energy level diagram of Fig. 3.6(a).

One strategy for obtaining the dominant polarization is to consider the difference spectra $I_{diff} \equiv I_{LCP} - I_{RCP}$ vs E. I_{diff} at 6 T is shown in Fig. 3.6(b). As we can see, two of the peaks have mainly LCP character, while the intermediate energy one is of RCP character. The natural implication, considering also the energy ordering, is to link the three peaks with the recombination of electrons from the S↑, S↓ and A↑ levels, as shown in Fig. 3.6(a). The three peaks, in increasing energy order, will be called $I_{S\uparrow}$, $I_{S\downarrow}$ and $I_{A\uparrow}$.

Ideally, the A↑ level should be empty for $\nu < 2$, so it should not be involved in the optical emission. Anyway some photo-electrons could relax to A↑, giving rise to the weak emission observed for B > 4 T. Other measurements, as discussed in the following, can contribute to the $I_{A\uparrow}$ emission.

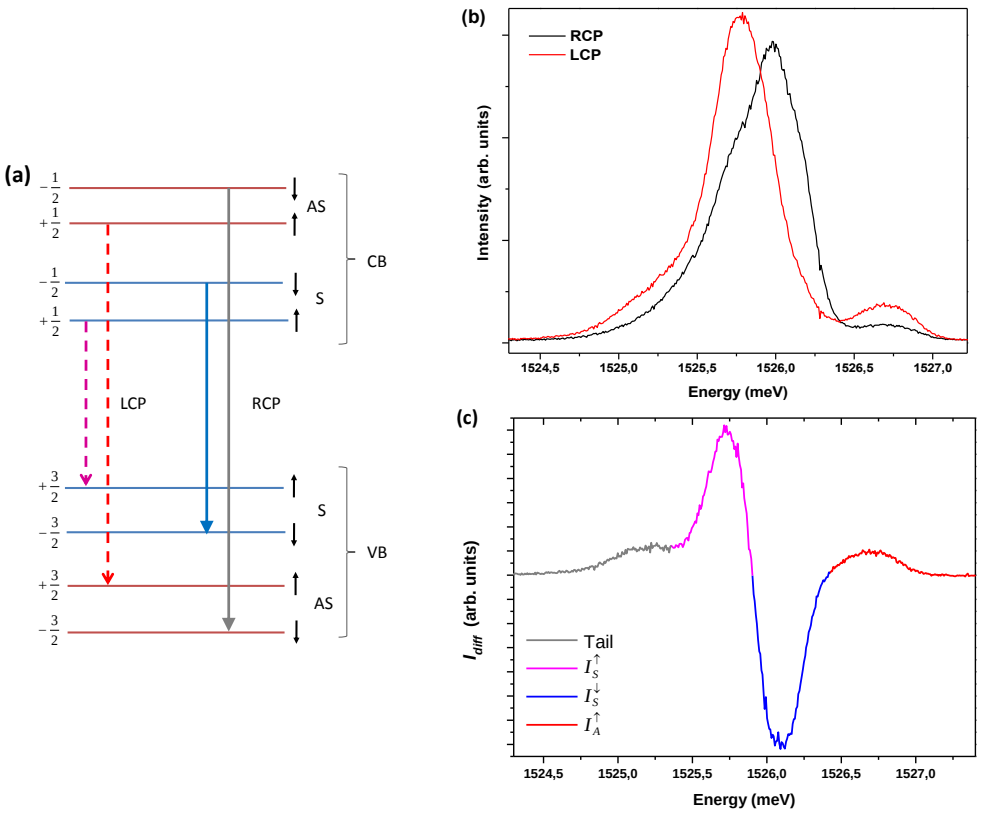

Figure 3.6: (a) Schematic of interband recombinations, resulting in the emission of left (LCP) and right (RCP) circularly polarized photons, represented by dashed and solid lines respectively. The z component of the total angular momentum is reported for each level. (b) Circular polarization components of the optical emission at B = 6 T, in the same experimental conditions as in Fig. 3.2. (c) Spectrum resulting from the difference of the LCP and the RCP spectra shown in (b). The colors refer to the three peaks identified in Fig. 3.4.

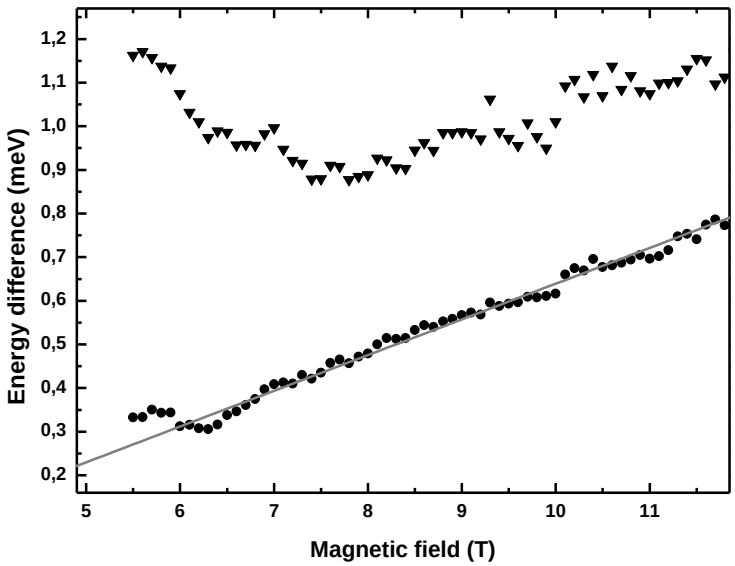

Figure 3.7: Peak energy difference as a function of magnetic field for two couples of peaks : $I_{S\downarrow}$, $I_{S\uparrow}$ (circles) and $I_{A\uparrow}$, $I_{S\uparrow}$ (triangles). The straight line is the best linear fit to the energy difference curve for the $I_{S\downarrow}$, $I_{S\uparrow}$ couple.

Further evidence in support of this assignment comes from the analysis of the energy differences between the three observed peaks. The difference between $I_{S\downarrow}$ and $I_{S\uparrow}$ is plotted in Fig. 3.7, showing a linear dependence on the magnetic field. Fitting the curve with a straight line, we get for the slope a value of 0.081 ± 0.002 meV/T and for the intercept (at B=0) -0.17 ± 0.01 meV. In the single particle picture, the difference corresponds to the Zeeman splitting $E_Z = g_{eff}\mu_B B$, so the estimated effective Landé factor is $g_{eff} \approx 1.4$. The value is in good agreement with the one obtained in [50] for a 15 nm wide single GaAs/AlGaAs QW. Since $g_{eff} = g_e + g_h$ and $g_e \approx 0.4$, we obtain $g_h \approx 1.0$.

However, there are also a few anomalies. Firstly a deviation from the linear behaviour is observed for 5.5T < B < 6.5T. Additionally the negative value of the intercept implies a finite splitting of the two peaks at B=0 and a crossing at B≈ 2T.

A trivial explanation of the first anomaly stems from the fact that for B < 6.5T the peaks are not well-resolved [2], yielding some uncertainty in the fitting analysis. In fact, starting from different initial peak parameters, slightly different fitting results can be obtained. We note also that in [57] a highly non-linear dependence of g_h on B was predicted for high magnetic fields, due to a field induced admixture between HH and LH states. However it is unlikely that such a mechanism is active only in a narrow magnetic field range.

Another more interesting possibility that can be invoked to explain both anomalies, considers the role of many-body interactions. In fact it was shown in [58] that, because of the different exchange interactions in the final luminescence states of the RCP and LCP recombinations, there can be deviations from the linear B-dependence of the Zeeman splitting, which can be expressed as :

$$E_Z = g_{eff}\mu_B B + \Delta\Sigma(B).$$

In our case, if $\Delta\Sigma(B)$ contains a constant negative term, this would explain the non-zero intercept, while B-dependent terms could account for anomalies in the 5.5 - 6.5 interval. Actually many-body corrections become relevant in proximity of QH states [58]. Further analysis and theoretical efforts are needed to clarify this issue.

The energy difference for the other couple of peaks $I_{S\uparrow}$, $I_{A\uparrow}$ is reported in Fig 3.7 with filled triangles. In the single particle picture, the splitting should be constant $\Delta_{SAS}^{eff} = \Delta_{SAS} + \Delta_{SAS}^{VB}$. In fact, for B > 6 T we do not see significant variations : the splitting is always higher than 0.9 meV and varies maximally by 0.2 meV in the whole field range.

Inelastic light scattering measurements give $\Delta_{SAS} = 0.36$ meV at zero magnetic field [19]. Since $m_{HH} \approx 6m_c$, the tunneling gap in the VB should be smaller, and $\Delta_{SAS}^{eff} < 0.72$ meV, less than what is seen experimentally. Together with the unusual increase for B < 6 T, these anomalies are analogous to those previously encountered and the same arguments can be invoked to account for them.

Finally, we discuss some additional aspects of the data :

1) All spectra present a low energy tail, as can be seen from the plot in Fig. 3.2 or from the fit in Fig. 3.4 (gray peak). The tail never splits into a separate peak; instead its energy follows the lowest emission line almost in parallel in the whole field range. Difference spectra show that it does not have a well-defined polarization character. As for its amplitude, it varies in proportion to that of the lowest line. This structure does not provide much information and its origin remains unclear.

2) In the range 1.5 - 3.5 T, the (0,0) line seems to have an internal structure, due to the overlap of two subpeaks. When fitting it with two Gaussians, we discovered that the

[2] $I_{S\uparrow}$ appears as a shoulder on the low energy side of $I_{S\downarrow}$.

energy difference between the subpeaks remains almost constant and both their intensities increase slightly when we switch from the LCP to the RCP configuration. We attribute one of the peaks to a direct interband electronic transition, while the other to a disorder replica of the first. In the plots of Figs. 3.5 and 3.8, the energy of the (0,0) line represents the intensity weighted average of the energies of the two subpeaks, and its intensity is the integrated area of the structure. The double structure of the $I_{S\downarrow}$ in the range 5.5 - 7.5 T behaves in the same way and an analogous interpretation can be given.

It must be noted that similar anomalies have been observed in other PL experiments and related to QH states. For example, in [59] a low energy tail appears in LCP emission in the vicinity of $\nu = 1$, which is linked to the shake-up of a spin-wave left in the CB after the $e - h$ recombination. It has been also demonstrated (see [25] for example) that the emission lines develop an internal structure in the vicinity of fractional QH states ($\nu = 3/7, 2/5, 1/3$), due to the formation of excitonic complexes involving quasiparticle excitations of the QH phase. However the anomalies seen in our experiment cannot be related to particular QH states, mainly because they are seen in a large range of magnetic fields, much wider than any QH plateau.

3) As it will be seen in Fig. 3.8 in the next section, there is a discontinuity in the energy and intensity plots at 5.5 T, where the (0,0) line is interrupted and a new line appears. This corresponds to the Zeeman splitting of the lowest emission line, which becomes visible for the first time at this value of B. In other words the (0,0) line represents an unresolved sum of $I_{S\uparrow}$ and $I_{S\downarrow}$.

3.2 Evidence of QH states

3.2.1 Transport Measurements

In order to unambiguously identify the QH states we have performed magneto-transport measurements. To this end we used a van der Pauw geometry to measure the longitudinal resistivity(ρ_{xx}) of the sample at 260 mK, in the range 0 - 10 T, under both dark and illuminated conditions.

The ρ_{xx} vs B curve, under illuminated conditions, is shown in Fig. 3.8(a). Characteristic dips in ρ_{xx} can be seen, which indicate the formation of QH states. Given the nominal density value of 1.1×10^{11} cm^{-2}, we expect the $\nu = 1$ state at 4.8 T. In fact a dip is present at 4.9 $\pm$ 0.1 T. The magnetic field values of the dips on its left are compatible with $\nu = 2, 3, 4$ and 5, while the one on the right with $\nu = 2/3$.

An unpleasant aspect of the data is that the integer QH signatures appear as very small dips on a high background resistivity, in contrast to the sharp clean features seen in Fig. 1.3, Chapter 1. The background resistivity could be of extrinsic origin. In fact, a high concentration of almost free electrons is formed in the vicinity of the doped layers, because of their high Si content and low Al concentration in the barrier. The electrons in the doped layer cause a strong conduction in parallel to the main channel given by the 2DEG, so they affect the 2DEG resistivity measurements. Indeed this sample with low Al concentration has been designed for optical studies and it is not optimized for transport measurements. Low Al content minimizes alloy fluctuations yielding sharper optical emission lines.

Additionally, QH states in bilayers are destroyed at lower temperatures than their cousins in single layers. We recall from Chapter 1 that for bilayers with no tunneling gap the $\nu = 1$ state is destroyed at 300 mK and the dip in the $\nu = 1/2$ state smears at 400 mK (Fig. 1.6(a), Chapter 1). Thermally induced dissipation makes the dips in ρ_{xx} less

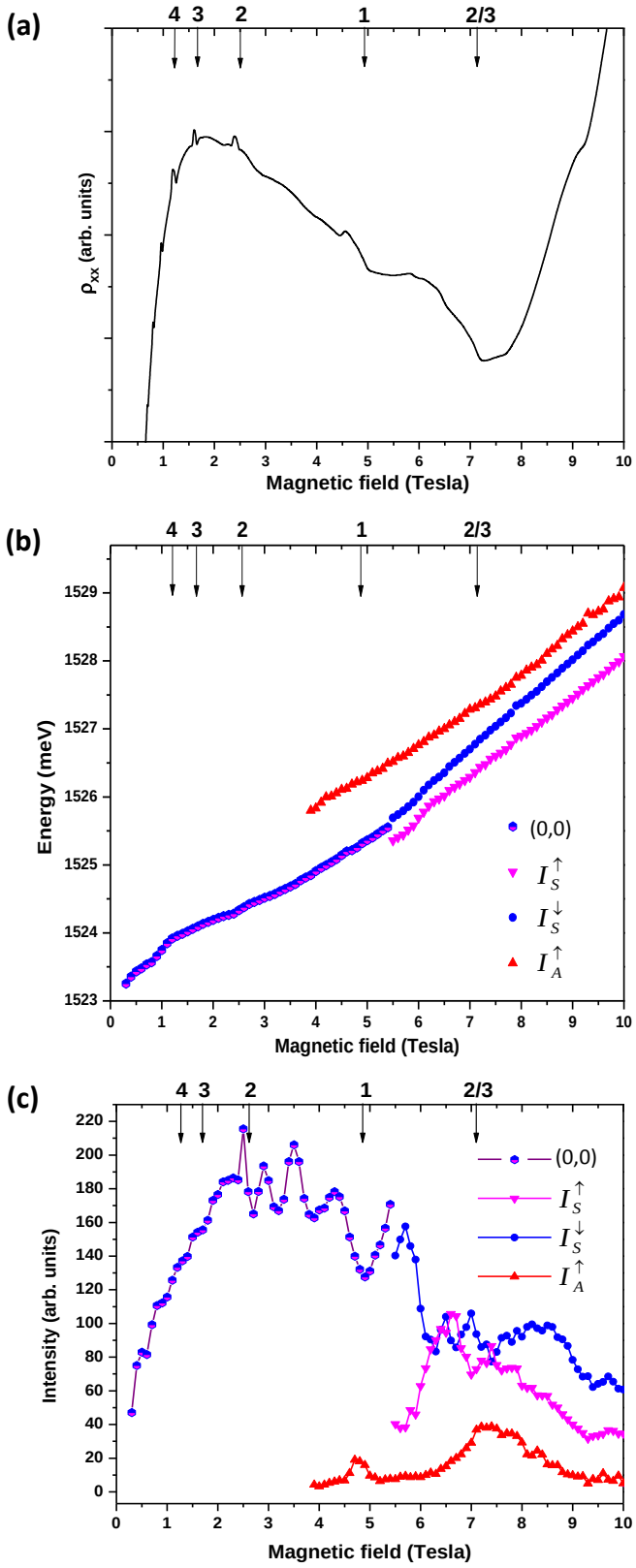

Figure 3.8: (a) Longitudinal resistivity vs magnetic field in the range 0 - 10 T, measured in a van der Pauw geometry at T = 260 mK. Numbers above the upper axis indicate the filling factor. (b) The peak energies and (c) integrated intensities for the (0,0), $I_{S\uparrow}$, $I_{S\downarrow}$ and $I_{A\uparrow}$ peaks, as obtained from Gaussian fits to the spectra in Fig. 3.2 at 50 mK.

pronounced and we believe that clearer signatures would have been obtained at T $<$ 260 mK. However this temperature is sufficient for uncovering the QH states.

Transport data taken in dark conditions show the same signatures, but at slightly smaller B values. The fact supports the hypothesis that the laser illumination used for PL measurements does not destroy the QH states, but merely modifies the carrier density, changing the magnetic field positions at which these states appear.

3.2.2 PL Signatures of QH States

Having identified the physical origin of the luminescence peaks, and the QH states that are realized in our sample, we can finally link the features seen in the magneto-luminescence spectra to the QH states. Figures 3.8(b),(c) resume the energy and intensity plots for the peaks (0,0), $I_{S\uparrow}$, $I_{S\downarrow}$ and $I_{A\uparrow}$.

Apart from the abrupt change around $\nu = 4$, the energy curves in Fig. 3.8(b) do not show other features that can be linked to the impact of inter-layer interactions. We believe the HS to be responsible for this behaviour. In fact, when the HS is valid, the emission energies are independent of the 2DEG density and do not provide information on electron correlations [47]. The role of the HS in our sample is demonstrated by the energy changeover around $\nu = 4$.

On the contrary, the intensity curves are quite rich in oscillations. The (0,0) line shows minima at 2.6, 3.2, 3.9 and 4.8 T. Two of these minima at 2.6 T and 4.8 T coincide with integer QH states at $\nu = 2$ and 1, respectively. A minimum is seen also at $\nu = 2/3$ (7.2T) in the lowest energy line $I_{S\uparrow}$. Similar minima at $\nu = 1$ and 2/3 were observed already in the initial PL investigations of the QHE in single layers [22, 24].

In order to understand these features, we can invoke the screening response of the electron gas. Since the electron gas becomes charge-gapped when it enters in the QH state, it fails to screen the disorder potential produced by the ionized donors. Localization of electrons and holes in the external potential leads to a reduction of the overlap of their wavefunctions in the plane of the well, suppressing the optical recombination.

This mechanism is sufficient for explaining the observed minimum at $\nu = 2$. We note, however, that at $\nu = 1$ and 2/3 in concomitance to the minimum of the lowest energy line, $I_{A\uparrow}$ shows an intensity maximum. We argue below that this effect reflects the reduction of pseudospin polarization at these QH states.

The $\nu = 1$ QH state

We start by considering the luminescence features around $\nu = 1$. The correspondence between the minimum in (0,0) and the maximum in $I_{A\uparrow}$ and their comparable magnetic field widths, suggest that at $\nu = 1$ a fraction of electrons leaves the spin up symmetric level and occupies the spin-up antisymmetric level. This phenomenon implies a loss of pseudospin polarization and we believe that it is induced by intrinsic many-body effects in the electron gas.

To illustrate the idea, we consider a bilayer containing only two non-interacting electrons. Because of the tunneling gap, electrons will occupy the lowest symmetric Landau level. Now we turn on the interaction. The Coulomb repulsion prefers to keep electrons in opposite layers, since this increases their net separation. This, however, would bring electrons in a superposition of S and AS states, so it would cost tunneling energy. Therefore there is a competition between tunneling and Coulomb interactions.

As a result of this competition, the ground state of the bilayer 2DEG at $\nu = 1$ is not a pseudospin ferromagnet, with a completely filled $S\uparrow$ level. Some electrons will be excited

to the AS level, in order to optimize the inter-layer correlations. This state, however, exhibits the characteristic transport signatures of the QHE, so it doesn't significantly modify the electrical conduction in the $\nu = 1$ QH state. It is therefore tempting to imagine that electrons in the AS level and the holes they leave behind in the S state form bound pairs [28].

This picture is supported by previous inelastic light scattering measurements [19], performed on the same sample. These experiments allowed to determine the energies of two long-wavelength spin excitations[3]. From these energies the order parameter $\langle \tau^x \rangle$, defined as the average pseudospin polarization along x, could be measured. If n_S and n_{AS} are the population densities of the symmetric and antisymmetric states respectively, then we have:

$$\langle \tau^x \rangle = \frac{n_S - n_{AS}}{n_S + n_{AS}}.$$

It was found that $\langle \tau^x \rangle \approx 0.36$, showing that 32% of electrons in the ground state reside in the antisymmetric level. It is not straightforward to evaluate $\langle \tau^x \rangle$ from the PL data. However, intuitively one expects that a decrease of $\langle \tau^x \rangle$ leads to a more intense emission from A↑, which is what is seen in Fig. 3.8(c).

The $\nu = 2/3$ QH state

$I_{A\uparrow}$ shows an enhanced emission also in the range 6.7 - 8 T, in correspondence to the intensity minimum of $I_{S\uparrow}$ and the ρ_{xx} minimum around $\nu = 2/3$. Again we attribute the excess emission to the loss of pseudospin polarization in the $\nu = 2/3$ QH state.

This state has been observed before (see [6, 35]) in the transport experiments on bilayers, but these transport data did not provide much insight into its physical properties. In our case, the comparison of the PL data at $\nu = 1$ and $\nu = 2/3$ is very instructive. In fact, at $\nu = 1$ the $I_{A\uparrow}$ line has an intensity of ≈20 units and nearly 30 % of the electrons populate the antisymmetric level. Here the intensity has doubled (≈40 units) and has become nearly half of the intensity of the $I_{S\uparrow}$ line. We conclude that at $\nu = 2/3$ there is a complete loss of pseudospin polarization, in other words $n_S = n_{AS}$. This is an unexpected result never reported so far, to our knowledge.

In Section 1.4.3, two wavefunctions were proposed for the 2/3 state. The first candidate wavefunction is a pseudospin ferromagnet with an orbital wavefunction identical to that of single layers at $\nu = 2/3$. However, in the pseudo-ferromagnetic state all the electrons occupy the symmetric level, which is not our case.

The other candidate is the Halperin (3,3,0) wavefunction, which basically describes the 2/3 state in terms of two uncorrelated layers, each of them corresponding to a 1/3 QH state. It is straightforward to show that

$$\langle 330 | \tau_x | 330 \rangle = 0,$$

hence the (3,3,0) state is pseudospin depolarized and thus compatible with the results of our analysis. In addition, this picture explains the unusually broad ρ_{xx} minimum observed in our transport data. In fact the 1/3 state in single layers has the widest minimum (and plateau) of all QH states (see for example Fig. 1.3).

Finally, we note that these candidate wavefunctions were proposed for bilayers with full spin polarization. However, from Fig. 3.8(c) we can see that the emissions from the S↓ and S↑ levels have comparable intensities, suggesting that the $\nu = 2/3$ QH state is not

[3] namely the spin-wave, built across the Zeeman gap of the spin-split symmetric levels and the spin-flip, built with transitions across Δ_{SAS} with simultaneous change in spin orientation.

spin polarized in our sample. Therefore a more realistic wavefunction for the QH state at $\nu = 2/3$ should be both spin and pseudospin unpolarized.

3.3 Summary

The magneto-PL spectra of the sample with finite tunneling gap offer evidence of the formation of several QH states (at $\nu = 2,\ 1,\ 2/3$), which were observed already in the first transport experiments on bilayers [35]. In particular, the occurrence of QH states is signalled by minima in the emission intensities.

Additionally, the emission intensities are sensitive to inter-layer correlations. In fact, the concomitance of intensity minima and maxima of different emission lines at $\nu = 1$ and $2/3$ suggests a loss of pseudospin polarization at these QH states, which is a fingerprint of the impact of inter-layer Coulomb interactions. This effect was observed previously through inelastic light scattering spectroscopy at $\nu = 1$ [19], while at $\nu = 2/3$ it was not seen before.

Finally, since the QWs of our sample are moderately narrow, the electron-photo-generated hole and electron-electron interactions have equal strength, giving rise to a peculiar cancellation of their effects, known as the Hidden Symmetry (HS). The HS hides the effects of electron correlations in the emission energies for $\nu < 4$. The onset of the HS at a filling factor twice of that seen in single layers emphasises once again the impact of the pseudospin degree of freedom.

Chapter 4

Photoluminescence from the Sample without Tunneling Gap

The key part of the experimental work carried out in this thesis, was dedicated to the study of the sample with zero tunneling gap, because of the remarkable phenomena predicted and partly observed in these systems at $\nu = 1$. We present in this chapter the most relevant optical data. The presentation and analysis of the data will follow nearly the same lines of the previous chapter.

The sample consists of two nominally symmetric modulation-doped GaAs/$Al_{0.1}Ga_{0.9}$As quantum wells, separated by 7 nm of pure AlAs barrier to ensure a negligible tunneling between the wells. A schematic of the sample's relevant energy levels is displayed in Fig. 4.1. Note that each spin level in the figure has a double pseudospin degeneracy. The electron gas has a total density of 6.9×10^{10} cm^{-2}, equally divided between the two wells, and a mobility above 10^6 cm^2/Vs. Since the inter-layer distance is $d = 9 + 9 + 7 = 25$ nm, we estimate that $d/\ell = 1.65$ at $\nu = 1$, which guarantees that a bilayer QH state will form at low temperatures at $\nu = 1$, as shown in Fig. 4.1(b).

4.1 PL Data and Analysis of the Peaks

We focus here on the LCP luminescence spectra taken in the magnetic field range 0 - 10 T, with 0.1 T step. Data were acquired in three different conditions : at 50 mK with 795 and 805 nm excitation lines (to rule out effects due to particular resonant conditions), and at 1 K with the laser at 795 nm. The incident power density on the sample was kept constant at $\approx 10^{-4}$ W/cm^2, and an integration time of 300 seconds per acquisition was sufficient for obtaining a good optical signal. We start with the PL data at 50 mK and 795 nm, shown in Fig. 4.2.

At B = 0 T the emission spectrum contains a single wide line, shown in Fig. 4.3(a). This line results from the recombination of photo-excited heavy holes (HH) with electrons in the Fermi sea as discussed in Section 3.1. The processes are illustrated schematically in Fig. 4.3(b). Thus all emission energies in the range E_0 - $(E_0 + E_F \frac{m_c}{m^*})$ are observed in the spectrum, where again m_c is the effective mass in the CB, and m^* is the reduced electron-HH mass. The Fermi energy E_F can be calculated from:

$$2\, D\, E_F \;=\; n,$$

where $D = m_c/\pi\hbar^2$ is the areal density of states, n is the gas density and the factor of 2 follows from the pseudospin degeneracy of the energy levels. We obtain $E_F = 1.23$ meV,

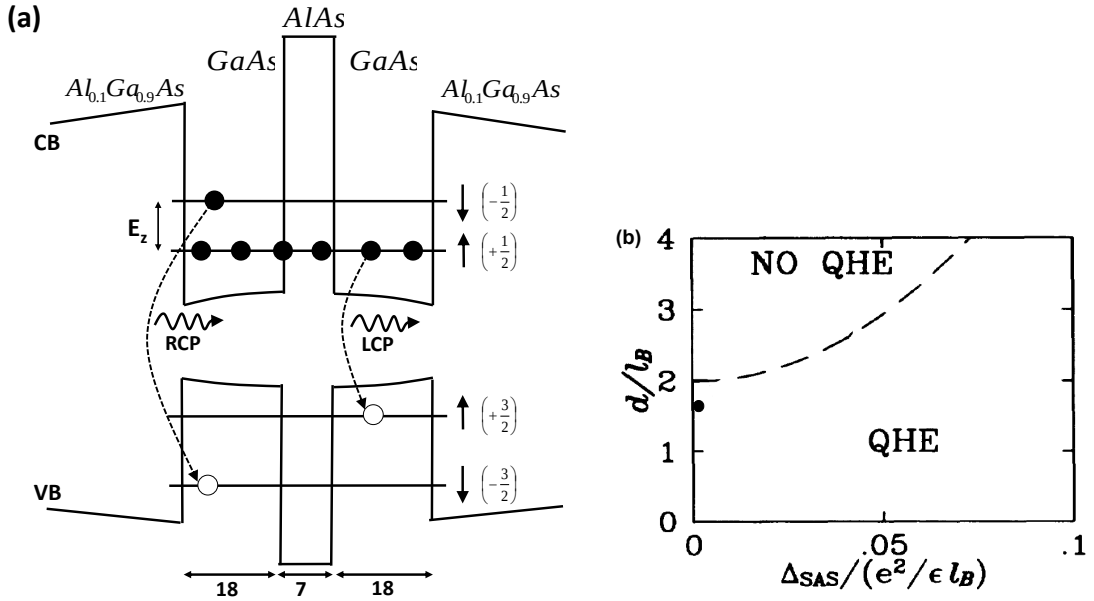

Figure 4.1: (a) Single particle energy levels in the lowest Landau level in the conduction(CB) and valence(VB) band, together with the band edge profiles in the growth direction for the sample with zero tunneling gap. The z-component of the total angular momentum for each level is shown in brackets and its orientation with respect to the magnetic field is represented by black arrows. Interband recombinations, indicated by dashed arrows, lead to the emission of left (LCP) and right (RCP) circularly polarized photons. The widths of the wells and the central barrier are given in nm at the bottom of the figure. (b) Position of the sample in the phase diagram of the QHE at $\nu = 1$, as obtained from [7].

which yields an optical width of $E_F \frac{m_c}{m^*} = 1.45$ meV. From the 0 T spectrum in Fig. 4.3(a) we evaluate an emission width of 1.3 ± 0.1 meV, compatible with the value obtained from the nominal density value.

The initial line splits into two bands (magenta and red curves in Fig. 4.2) upon application of a perpendicular magnetic field. The lower-energy band has an internal structure and displays various amplitude oscillations. At B $\approx$ 5 T a new line appears (blue curve) that splits from the magenta peak above 6 T. The higher band gains intensity for B $>$ 3 T and above 4 T it also splits into two peaks (red and green). The lower peak has a particular behaviour : it approaches the higher energy peak of the other band and at the same time it progressively looses intensity, until it dies out at 8.5 T. At B $>$ 6 T, a new peak (grey) appears on the high-energy side of the spectrum. The five peaks seen in the range 6 - 8.5 T will be labelled $I_0^{\uparrow}$, $I_0^{\downarrow}$, $I_1^{\uparrow}$, $I_2^{\uparrow}$ and $I_3^{\uparrow}$, in increasing order of energy.

In the range 9.5 - 10 T the whole spectrum becomes more intense. We attribute this behaviour to a resonant absorption of the exciting light. In fact the enhancement occurs in a different interval (9.0 - 9.5 T) when we excite the sample with the 805 nm line (data not shown here).

The fitting procedure is necessary for obtaining quantitative information on the energies and intensities of the peaks, because the peaks are not resolved in a significant part of the spectra. In Fig. 4.4 we illustrate a representative fit, performed on a spectrum taken at 7 T. Gaussian lines have been preferred to Lorentzians, because they fit better the spectra, as for the sample with a finite tunneling gap (see Chapter 3).

The fitting errors for the peak energies are below the instrumental resolution (70 μeV), while for the peak intensities the relative error remains smaller than 10^{-3}. Therefore

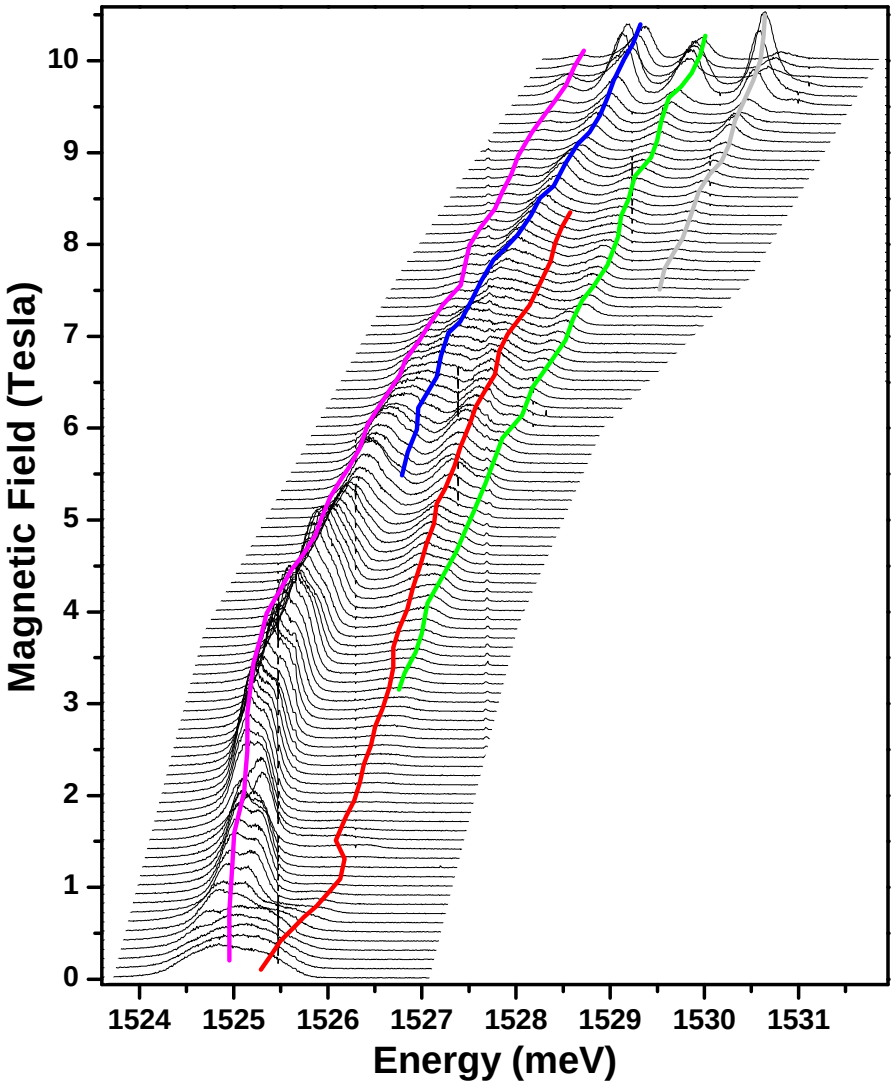

Figure 4.2: Left circularly polarized optical spectra in the magnetic field range 0 - 10 T, taken at T = 50 mK with an excitation wavelength of 795 nm. The coloured lines are guides to the eye that follow the evolution of the various peaks. In all following figures we will use the same colour representation for the peaks. Spectra are vertically shifted for clarity.

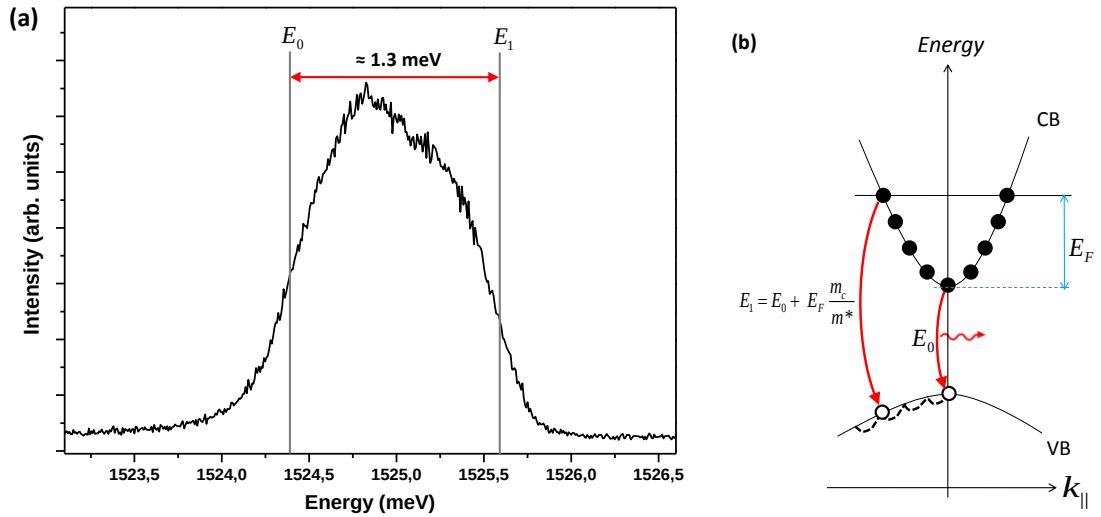

Figure 4.3: (a) Plot of the 0 T emission spectrum, taken in the same conditions as in Fig. 4.2. (b) Simplified band diagram of the sample at 0 T, showing the Fermi sea in the CB and the various relaxation steps (dashed black curves) of the hole in the VB. The figure illustrates the optical recombinations of minimum (E_0) and maximum (E_1) energy.

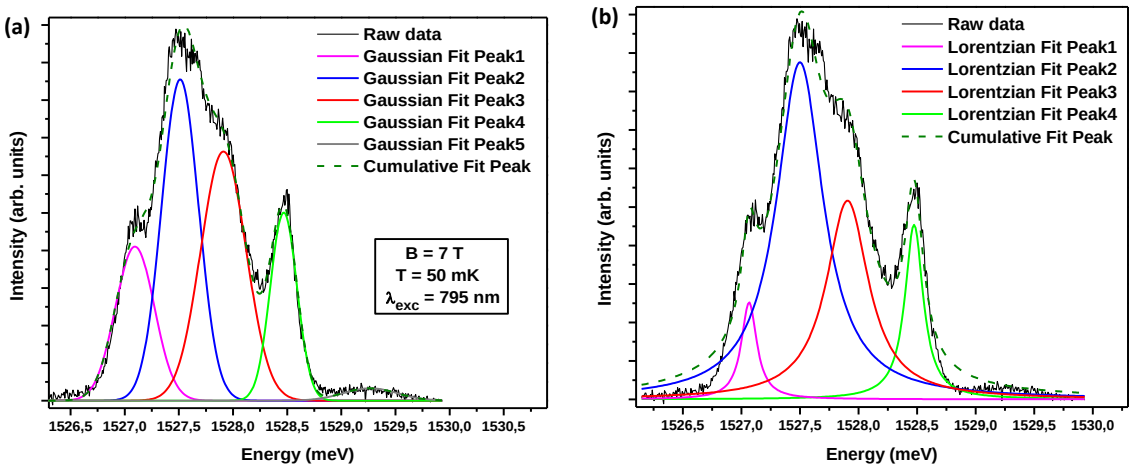

Figure 4.4: Best fit to the 7 T spectrum in Fig. 4.2 with five Gaussian (a) and four Lorentzian (b) lines. Clearly the Gaussian fit outperforms the Lorentzian, which fails to reproduce the lower and higher energy parts of the spectrum, because of the high intensity tails of the Lorentzian lines. Note that an additional (fifth) peak on the high energy side of the spectrum in (b) would further deteriorate the quality of the fit.

the fitting errors have been omitted from the energy or intensity plots presented in the following.

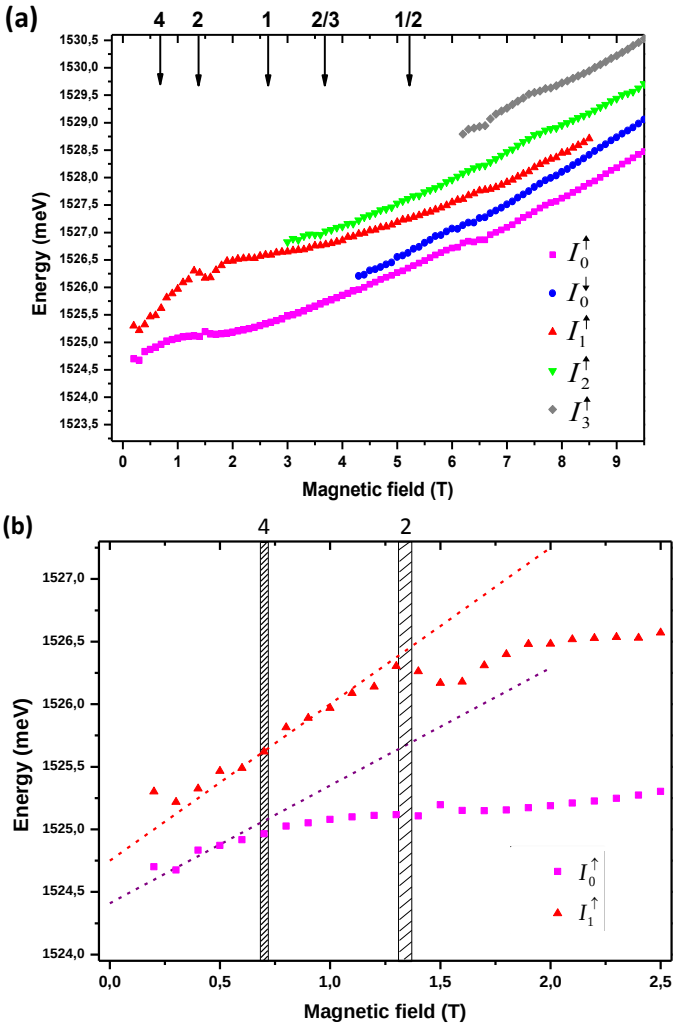

Figure 4.5: (a) Peak energies vs magnetic field as obtained from the Gaussian fits to the data shown in Fig. 4.2. The positions of the QH states, as derived from the magneto-transport analysis discussed in the following section, are also shown in the upper axis. (b) Magnified view of the peak energy evolutions for filling factors $\nu > 1$. The vertical strips indicate the position and magnetic field width of the QH states at $\nu = 4$ and 2.

4.1.1 Low Magnetic Field Sector

The evolution of the peak energies with magnetic field is shown in Fig. 4.5. We focus here on the field range 0 - 2.5 T (filling factor $\nu > 1$.). The peak energies in this range are reported in Fig. 4.5(b).

For B < 1.4 T the $I_1^\uparrow$ energy goes linear with B. The linear fit gives a slope of 1.30±0.04 meV/T[1]. This line results from the recombination of an electron in the n = 0 LL with a HH in the m = 1 LL, or (0,1) recombination in the notation of Chapter 3. In fact, using the above value for the slope and $m_c = 0.067m_e$, we obtain a hole mass of $m_v \approx 0.38m_e$, consistent with previously reported values [26].

[1]The slopes found in the other two scans are compatible with this value. In particular, we obtain 1.28 ± 0.03 meV/T for the scan at 805 nm and 1.27 ± 0.05 meV/T for the scan at 1 K.

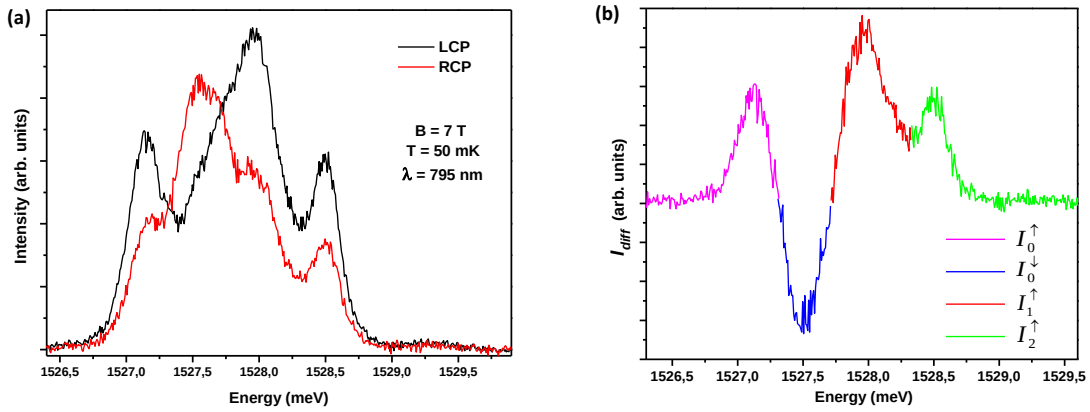

Figure 4.6: (a) Circular polarization components of the optical emission at B = 7 T, in the same experimental conditions as in Fig. 4.2. (b) Spectrum resulting from the difference of the RCP to the LCP spectrum in (a). The coloured segmentations represent the five peaks seen at B > 6 T.

Since the $I_0^{\uparrow}$ peak has a lower energy, it should originate from a (0,0) recombination. As illustrated in Fig. 4.5(b), the emission energy for $\nu > 4$ is well-described by a linear function with slope 1.01 ± 0.03 meV/T, compatible indeed with the above value of the HH mass. At higher fields the energy variation becomes quadratic and the curve deviates on the low-energy side of the fitting line.

This behaviour is analogous to the one encountered in the sample with tunneling gap. The changeover of the ground emission energy from linear to quadratic at $\nu \approx 4$, suggests the onset of the Hidden Symmetry (HS) and the impact of the pseudospin degree of freedom. The validity of the HS requires charge-symmetric interactions and occupation of the lowest LL only for both e and h. The charge symmetry condition is satisfied in the present sample, because the wells are narrow (18 nm) and the physical properties of the sample are symmetric in the growth direction, so that e and h cannot separate in different planes inside the single wells. The occupation of the lowest LL translates into $\nu < 4$, because each LL contains four sublevels *i.e.* two spin states, which are doubly pseudospin degenerate.

The manifestation of the HS in both samples demonstrates that this symmetry does not depend on the energy difference (tunneling gap) between the pseudospin levels. More generally the HS should remain valid for any arrangement of the energies of the four states inside the lowest LL, provided that $\Delta_{SAS} \ll \hbar\omega_c$.

Finally we note that the linear to quadratic change at $\nu = 4$ is only observed for the lowest energy line, whereas the $I_1^{\uparrow}$ energy is linear until $\nu \approx 2$ (1.4 T). This behaviour is in contrast with that of the sample with $\Delta_{SAS} \neq 0$, where both emission lines display the changeover at $\nu = 4$.

4.1.2 High Magnetic Field Sector

For B > 6 T the polarized PL spectra are composed of five peaks. In the single particle picture shown in Fig. 4.1, only two optical recombinations are possible and they have opposite circular polarizations. Hence we expect to see only one peak in the polarized spectra. The discrepancy emphasises the impact of many-body effects in the optical emission. The quadratic B-dependence of the emission energies brings further evidence of the role of Coulomb interactions.

When the 2DEG density is below 2×10^{11} cm^{-2}, e and h can form bound complexes such as neutral or charged excitons [49–51]. The fact that we see five peaks means that

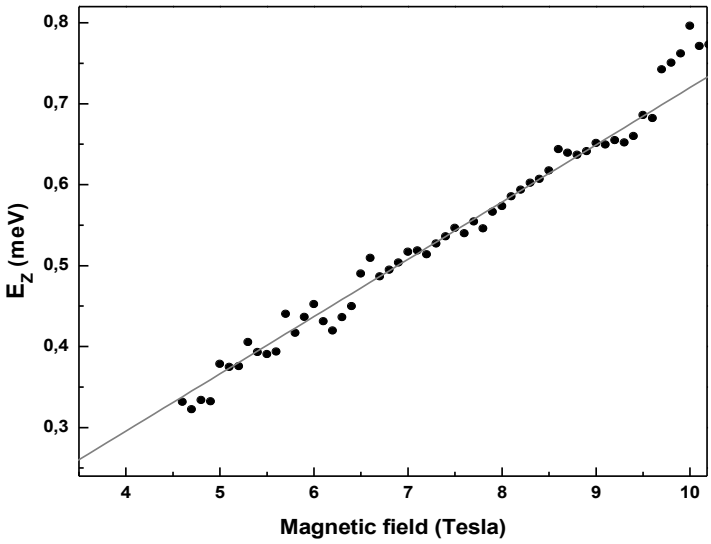

Figure 4.7: Energy difference of peaks $I_0^{\downarrow}$ and $I_0^{\uparrow}$ as a function of magnetic field, as obtained from Gaussian fits to the data in Fig. 4.2. The straight line represents the best linear fit to the energy curve.

different types of $e-h$ complexes are formed in our sample at high magnetic fields.

Regardless of the microscopic origin of the emission peaks, the polarization analysis is useful for identifying the spin state of the electrons involved in the optical recombination. As shown in Fig. 4.1, spin-up and spin-down electrons recombine by emitting LCP and RCP polarized photons, respectively.

Figure 4.6(a) illustrates representative spectra, with opposite circular polarizations, taken at 7 T. Both spectra contain five peaks, that appear at the same energies but with different intensities. In analogy with the tunneling gap sample, we attribute this behaviour to HH-LH mixing effects in the valence band. Similarly, we use the difference of the polarized spectra, to obtain the dominant polarization character of each peak. The difference spectrum $I_{diff} \equiv I_{LCP} - I_{RCP}$ at 7 T is shown in Fig. 4.6(b). We see that $I_0^{\uparrow}$, $I_1^{\uparrow}$, and $I_2^{\uparrow}$ have a predominant LCP polarization, so that they all involve the recombination of spin-up electrons. Given the low intensity of $I_3^{\uparrow}$, it is difficult to establish its polarization. Anyway the polarized spectra at B $>$ 8 T (not shown here) demonstrate that it is also LCP polarized. $I_0^{\downarrow}$ is the only RCP polarized peak, and it results from the recombination of spin-down electrons.

The opposite polarization characters of $I_0^{\uparrow}$ and $I_0^{\downarrow}$, and their monotonically increasing energy separation (Fig. 4.5(a)) suggest that they correspond to the Zeeman components of the same initial luminescence state. The plot of the energy difference between the two peaks, shown as black squares in Fig. 4.7, confirms this interpretation. In fact, the dots in Fig. 4.7 are well-described by a linear function with slope 0.071±0.003 meV/T and intercept -0.09±0.01 meV. Since Zeeman counterparts have an energy separation of $E_Z = g_{eff}\mu_B B$, we can estimate the effective Landé factor $g_{eff} = 1.22 \pm 0.05$, which agrees with previously reported values [50, 60].

Our data do not provide direct information on the microscopic origin of the emission peaks. This issue needs further theoretical and experimental investigation. The theoretical understanding of the magneto-luminescence of bilayers could reveal other aspects of the PL data that highlight the role of $e-e$ correlations and the pseudospin degree of freedom.

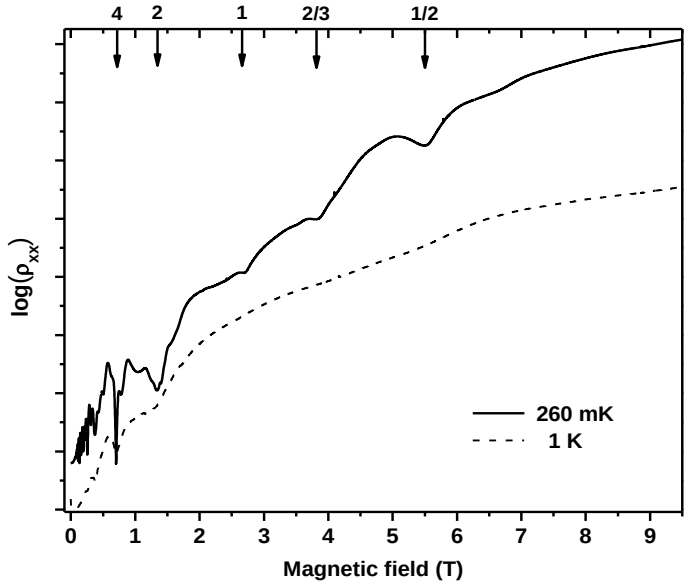

Figure 4.8: Longitudinal resistivity as a function of magnetic field for the sample with zero tunneling gap, under illumination, at 260 mK (full curve) and 1 K (dashed curve). The 1 K resistivity curve has been shifted downward for clarity. The total filling factor is indicated in the upper horizontal axis.

On the experimental side, the study of the evolution of the PL spectra with the electron density could clarify the nature of the many-body $e-h$ complexes that give rise to the observed peaks, in analogy to what performed in single layers [51].

4.2 Evidence of QH States

4.2.1 Transport Measurements

QH states are easily identified in magneto-resistivity measurements as zeros in the longitudinal resistivity and quantized plateaus in the Hall resistivity. To this end, we measured the magnetic field dependence of the longitudinal resistivity in a Van der Pauw geometry, after LED illumination, at 260 mK and at 1 K. The results are shown in Fig. 4.8.

Dips in the resistivity at 260 mK are found at 0.7, 1.4, 2.7, 3.8 and 5.4 T, that signal the formation of QH states with $\nu = 4$, 2, 1, 2/3 and 1/2, respectively. At 1 K, we still see a dip at $\nu = 4$, although smaller than the one at lower temperature; some anomaly remains near $\nu = 2$, while the signatures of the QH states with $\nu \leq 1$ almost disappear. We remark that the states at $\nu = 1$ and 1/2 are genuinely linked to the impact of interlayer correlations. In particular the $\nu = 1/2$ state has no counterpart in single layer - single component systems.

The measurements taken in dark conditions show the same signatures, but at slightly different magnetic fields (± 0.1 T). This demonstrates the marginal influence of laser illumination on the QH states in this sample.

4.2.2 PL Signatures of QH States at 50 mK

Having identified the QH states in magneto-transport, we now consider how these QH states appear in our PL data. The magnetic field dependence of the peak intensities, for all three scans, is shown in Fig. 4.9. In the following we show that the intensity curves provide evidence of the formation of QH states.

At 50 mK the intensity of $I_0^{\uparrow}$ shows several oscillations. The minima of the oscillations occur at B = 1.4, 2.6, 3.7 and 5.3 T, which coincide (to within 0.1 T) with the minima in ρ_{xx}. We link these intensity minima with the formation of QH states with $\nu = 2$, 1, 2/3, and 1/2. The fact that the oscillations are not modified when the excitation wavelength is changed from 795 to 805 nm, rules out the possibility that they are related to changes in the absorption.

Additional optical anomalies around 1.4 T suggest the existence of a QH state at $\nu = 2$. In particular we observe a maximum in the $I_1^{\uparrow}$ intensity and a dip in its energy curve (see red triangles in Figs. 4.9 and 4.5(a)). Similar anomalies in the PL energies, in correspondence to the onset of QH states, were also reported in previous works on single layers [23, 24].

Further experimental work is needed in order to clarify the connection between the suppression of the ground emission intensity and the onset of the QH phases. There are two possibilities : a decrease of the optical transition matrix element, or a many-body induced depopulation of the lowest spin-split LL .

The decrease in the optical matrix element can derive from the reduced overlap of the e and h wavefunction, due to the localization of carriers in the disorder potential. The latter becomes important in the QH phase, because of the inability of the electron gas to screen external potentials, due to the presence of a gap in the charged excitations spectrum. This hypothesis can be further checked by measuring the variations of the radiative recombination times, through time-resolved PL.

We exclude the depopulation of the spin up electron state as the cause of the observed minima, since it would lead to intensity minima in the other LCP polarized peaks ($I_1^{\uparrow}$, $I_2^{\uparrow}$ and $I_3^{\uparrow}$), which are not observed in our data.

In the end, we note that apart from the anomalies at $\nu = 2$, the luminescence energies do not provide much evidence for the QH states. We believe that this phenomenon is a consequence of the HS, that we observe in our sample. In fact when the HS is valid, the PL energy is expected to be independent of the number of electrons in the 2DEG , thus offering no information on $e - e$ correlations.

To highlight the impact of $e - e$ correlations in the PL energies, we should break the HS. One way of breaking the HS is to create a charge imbalance between the layers, which can be controlled by applying suitable gate voltages.

It might be argued that the charge imbalance could destroy or modify the properties of the QH states. Actually, it has been predicted theoretically [61] and observed experimentally [62, 63] that the coherent $\nu = 1$ phase is robust against density imbalance, whereas the $\nu = 1/2$ state is destroyed with small perturbations. Therefore a small charge imbalance could be a useful tool for obtaining information on the properties of the $\nu = 1$ QH phase from the PL emission energies. Anyway this technique cannot be applied to the study of the QH state at $\nu = 1/2$, and its suitability to the study of the other bilayer QH states is uncertain.

4.2.3 Temperature Evolution of the QHE Signatures

Finally, let's consider the PL data at 1 K (Fig. 4.9(c)), to verify the temperature evolution of the QH signatures. In order to quantify the intensity minima in Figs. 4.9(a) and (c), we evaluate the fractional depth, defined as the ratio between the depth of the minimum, measured from the lowest maximum surrounding it, and the height of such maximum.

When the temperature increases from 50 mK to 1K, the fractional depth of the $\nu = 2$

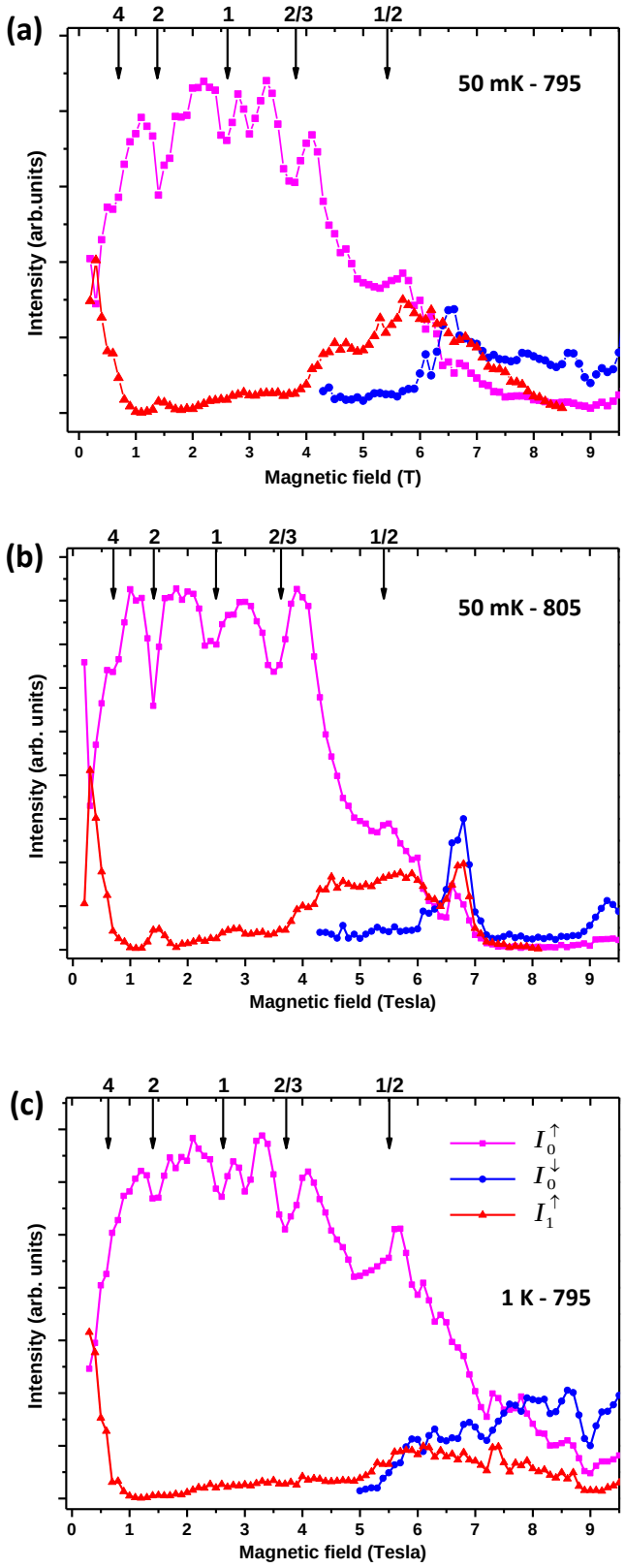

Figure 4.9: Peak intensity vs magnetic field for $I_0^{\uparrow}$, $I_0^{\downarrow}$, and $I_1^{\uparrow}$ at (a) T = 50 mK with laser excitation at λ = 795 nm (b) T = 50 mK, λ = 805 nm, and (c) T = 1 K, λ = 795 nm. The filling factors where the QHE is observed in transport experiments are indicated with arrows in the upper axis.

minimum (in the $I_0^{\uparrow}$ curve) decreases from 0.27 to 0.09, and the $I_1^{\uparrow}$ maximum disappears. Thus the temperature behaviour of the optical and transport signatures of the $\nu = 2$ QH state agree : in both measurements the signatures appear at 50 mK, but they are significantly weakened at 1 K. We conclude that the QH phase is not destroyed at 1 K, but it is weakened by the thermal excitation of quasiparticles.

On the contrary, we observe that the temperature evolution of the optical signatures of the $\nu = 1$ and 2/3 QH states is not so pronounced. In fact, with increasing temperature the fractional depth of the $\nu = 1$ minimum undergoes just a slight decrease (from 0.15 to 0.11), while the depth of the $\nu = 2/3$ minimum remains unchanged (≈ 0.17). In sharp contrast, the resistivity minima around $\nu = 1$ and 2/3 disappear almost completely at 1 K. We argue that the $\nu = 1$ and 2/3 QH states are not completely destroyed at 1 K, but there is a significant difference in the way they manifest in optical and transport measurements.

At $\nu = 1$ the disagreement between the temperature behaviour of the transport and optical data is not a novelty. In fact, while transport experiments [12,14] report an abrupt variation of the QH signatures for T $>$ 300 mK, a previous inelastic light scattering experiment on the sample studied here [20] indicates a continuous temperature evolution of the QH signature up to 1 K.

This was attributed to the role of disorder, which leads to a breakdown of the sample into domains (puddles) containing correlated and uncorrelated electron fluids [20]. Above 300 mK, the puddles with the correlated fluid become localized, so that the transport signatures of the QH state are destroyed. However they continue to contribute to the optical properties, which can explain why the intensity minimum in the PL data persists at 1 K. As the temperature further increases, the domains containing the correlated fluid should decrease both in number and dimensions. Therefore, in order to test this picture we should measure the luminescence spectra at even higher temperatures T $>$ 1 K. The minimum at $\nu = 1$ should wash out as the temperature increases above 1 K.

Regarding the QH state at $\nu = 1/2$, we note that when the temperature increases, the wide minimum around 5.3 T in the $I_0^{\uparrow}$ curve is replaced by a monotonically increasing profile. Hence both the transport and optical data suggest that the $\nu = 1/2$ QH state is destroyed at 1 K.

4.3 Summary

The magneto-PL spectra of the sample with zero tunneling gap offer evidence of the formation of QH states at $\nu = 2$, 1, 2/3, and 1/2, which appear as intensity minima. Inter-layer Coulomb interactions are of paramount importance for the occurrence of QH states at $\nu = 1$ and 1/2, although the PL spectra do not offer more insights with respect to the transport data.

The temperature evolution of the PL spectra emphasises the peculiar behaviour of the states at $\nu = 1$ and 2/3, which are not destroyed completely at 1 K, even though they lack the characteristic transport signatures of QH states. The fact could be related to the role of disorder in the finite temperature phase transition of these states.

Again the emission energies highlight the role of the Hidden Symmetry and of the pseudospin degree of freedom. While the PL energies do not provide information on electron correlations, the occurrence of the HS at $\nu = 4$ brings further evidence of the role of the pseudospin in this bilayer sample.

Finally, we note that our data do not show evidence of the Bose-Einstein condensation of inter-layer excitons at $\nu = 1$. The lack of such evidence in the PL energies could be due

to the impact of the HS. To this respect, the study of unbalanced bilayers, which break the HS and thus could provide access to the manifestation of inter-layer correlations, seems to be a promising direction for further research.

Conclusions

In this work we have reported the photoluminescence (PL) investigation of coupled electron double layers, confined in GaAs/AlGaAs double quantum wells, in the quantum Hall (QH) regime. Our main result is the identification, in the PL spectra, of several QH states dictated by inter-layer interactions. In addition, we have found evidence of inter-layer coupling in the intensity variation of the observed PL lines and in the PL energy evolution at low magnetic fields.

In particular, we studied two bilayer samples with zero and finite tunneling gap at temperatures down to 50 mK. In both samples the emission intensities are sensitive to the formation of QH states. In fact intensity minima appear in correspondence to the QH states with $\nu = 2$, 1, and 2/3.

Additionally, in the sample with finite tunneling gap our data suggest a loss of pseudospin polarization for the states with $\nu = 1$ and 2/3. This phenomenon, which is a fingerprint of the role of inter-layer correlations, was reported also in previous inelastic light scattering experiments for the $\nu = 1$ QH state, while at $\nu = 2/3$ it was not observed before.

In the sample with zero tunneling gap we obtained evidence of the QH state at $\nu = 1/2$. This state has no analogue in single-layer single-component systems and it is a genuine consequence of inter-layer Coulomb interactions. Furthermore we have studied the temperature evolution of the QH states up to 1 K. The retention of the luminescence signatures of the $\nu = 1$ and 2/3 states at 1 K leads to the conclusion that these QH states are not completely destroyed at this temperature, contrary to what suggested by the transport measurements. This behaviour could reflect the role of disorder in the finite temperature phase transition of the $\nu = 1$ and 2/3 QH states. To this respect the measurement of the luminescence at temperatures above 1 K could shed new light on the mechanism of this phase transition.

In both samples the emission energies reveal the central role of the Hidden Symmetry (HS). This symmetry results from a peculiar cancellation of the electron-electron and electron - photo-generated hole interactions and it hides the effects of Coulomb interactions above a certain magnetic field related to the occupation of the lowest Landau level. The HS manifests as an abrupt change from linear to quadratic dependence of the emission energy versus magnetic field at $\nu = 4$. The observation of this effect at a filling factor twice as high as in single layers in both bilayer samples reflects the impact of the pseudospin degree of freedom. For $\nu < 4$ the PL energies vary smoothly with magnetic field and they do not provide information on electron correlations.

In order to highlight the impact of $e-e$ correlations in the PL energies at $\nu < 4$, future studies should focus on bilayer samples with different electron densities in the two layers, *aka* unbalanced bilayers. The charge imbalance, which can be tuned by applying suitable gate voltages, should break the HS and make the PL energies sensible to the electron correlations in the QH states. This technique can be successfully applied to the study of

the properties of the $\nu = 1$ state and in particular to the exploration of the physics related to the Bose-Einstein condensation of inter-layer excitons. Indeed the $\nu = 1$ state has been shown to be stable against small charge imbalances [63].

There are also some unclear aspects of our data, that call for further investigation. In particular, in the sample with zero tunneling gap we observe five emission lines, whose origin is not fully understood. We believe that the theoretical study of electron double layers in the presence of valence band holes could help to clarify the nature of the many-body states that lead to the observed optical emissions and it could enable us to extract more information from the PL data. The understanding of this issue could benefit from the experimental study of samples with tunable electron density, in analogy to what has been done in single layers [51].

In conclusion, this work demonstrates that PL spectroscopy is a sensitive probe of inter-layer correlations and thus opens a new route to the study of QH bilayers [64]. We hope that in the near future this technique will lead to new insights into the remarkable properties of these systems.

Bibliography

[1] K. von Klitzing, G. Dorda, and M. Pepper, *Phys. Rev. Lett.* **45** , 494 (1980). 5

[2] D.C. Tsui, H.L. Stormer, and A.C. Gossard, *Phys. Rev. Lett.* **48** , 1559 (1982). 5

[3] R.B. Laughlin, *Phys. Rev. B* **27** , 3383 (1983) 5, 13

[4] F.D.M. Haldane and E.H. Rezayi, *Bull. Am. Phys. Soc.* **32** , 892 (1987). 5

[5] T. Chakraborty and P. Pietilainen, *Phys. Rev. Lett.* **59** , 2784 (1987). 5

[6] J.P. Eisenstein, G.S. Boebinger, L.N. Pfeiffer, K.W. West, and Song He, *Phys. Rev. Lett.* **68** , 1383 (1992). 5, 16, 54

[7] S.Q. Murphy, J.P. Eisenstein, G.S. Boebinger, L.N. Pfeiffer and K.W. West, *Phys. Rev. Lett.* **72** , (1994) 728. 5, 17, 18, 43, 58

[8] H. A. Fertig, *Phys. Rev. B* **40** , 1087 (1989). 5

[9] X.G. Wen and A. Zee, *Phys. Rev. Lett.* **69** , 1811 (1992). 5

[10] K. Yang, K. Moon, L. Zheng, A.H. MacDonald, S.M. Girvin, D. Yoshioka, and Shou-Cheng Zhang, *Phys. Rev. Lett.* **72**, 732 (1994). 5

[11] K. Moon, H. Mori, K. Yang, S.M. Girvin, A.H. MacDonald, L. Zheng, D. Yoshioka, and Shou-Cheng Zhang, *Phys. Rev. B* **51**, 5138 (1995). 5, 21

[12] I.B. Spielman, J.P. Eisenstein, L.N. Pfeiffer and K.W. West, *Phys. Rev. Lett.* **84**, 5808 (2000). 5, 21, 22, 67

[13] I.B. Spielman, J.P. Eisenstein, L.N. Pfeiffer and K.W. West, *Phys. Rev. Lett.* **87**, 036803 (2001). 5

[14] M. Kellogg, J.P. Eisenstein, L.N. Pfeiffer and K.W. West, *Phys. Rev. Lett.* **93**, 036801 (2004). 5, 22, 23, 67

[15] E. Tutuc, M. Shayegan and D.A. Huse, *Phys. Rev. Lett.* **93**, 036802 (2004). 5, 23

[16] L. Tiemann, J.G.S. Lok, W. Dietsche, K. von Klitzing, K. Muraki, D. Schuh and W. Wegscheider, *Phys. Rev. B* **77**, 033306 (2008). 5, 23

[17] M. Manfra, J. Pniower, B.B. Goldberg, A. Pinczuk, V. Pellegrini, L.N. Pfeiffer and K.W. West *Physica E* **6** , 590 (2000). 5, 25

[18] S. Luin, V. Pellegrini, A. Pinczuk, B.S. Dennis, L.N. Pfeiffer and K.W. West, *Phys. Rev. Lett.* **90** , 236802 (2003). 5, 24

[19] S. Luin, V. Pellegrini, A. Pinczuk, B.S. Dennis, L.N. Pfeiffer and K.W. West, *Phys. Rev. Lett.* **94** , 146804 (2005). 5, 24, 25, 44, 50, 54, 55

[20] B. Karmakar, V. Pellegrini, A. Pinczuk, L.N. Pfeiffer and K.W. West, *Phys. Rev. B* **80** , 241312 (2009). 5, 24, 25, 67

[21] B. Karmakar, V. Pellegrini, A. Pinczuk, L.N. Pfeiffer and K.W. West, *Phys. Rev. Lett.* **102** , 036802 (2009). 5, 24, 25

[22] A.J. Turberfield, S.R. Haynes, P.A. Wright, R.A. Ford, R.G. Clark, and J.F. Ryan *Phys. Rev. Lett.* **65**, 637 (1990). 5, 26, 53

[23] B.B. Goldberg, D. Heiman, M. Dahl, A. Pinczuk, L.N. Pfeiffer and K.W. West, *Phys. Rev. B* **44** , 4006 (1991). 5, 26, 30, 31, 65

[24] B.B. Goldberg, D. Heiman, A. Pinczuk, L.N. Pfeiffer and K.W. West, *Phys. Rev. Lett.* **65** , 641 (1990). 5, 26, 30, 31, 53, 65

[25] M. Byszewski, B. Chwalisz, D.K. Maude, M.L. Sadowski, M. Potemski, T. Saku, Y. Hirayama, S. Studenikin, D.G. Austing, A.S. Sachrajda and P. Hawrylak *Nat. Phys.* **2** , 239 (2006). 5, 26, 31, 51

[26] Gerald Bastard, *Wave mechanics applied to semiconductor heterostructures*, Les Editions de Physique, 1988. 7, 26, 27, 47, 61

[27] R. Dingle, H.L. Störmer, A.C. Gossard, and W. Wiegmann, *Appl. Phys. Lett.* **33**, 665 (1978). 8

[28] Stefano Luin, *Spectroscopy of emergent states in quantum Hall bilayers*. Ph.D.Thesis. Scuola Normale Superiore, Pisa, 2005. http://download.sns.it/nest/Luin_ PhDThesis.pdf 8, 14, 54

[29] S.M. Girvin, *The Quantum Hall Effect: Novel Excitations and Broken Symmetries* Les Houches Lecture Notes, in: *Topological Aspects of Low Dimensional Systems*, ed. by Alain Comtet, Thierry Jolicoeur, Stephane Ouvry and Francois David, (Springer-Verlag, Berlin and Les Editions de Physique, Les Ulis, 2000). 11, 13

[30] H.L. Störmer, *Physica B* **177**, 401 (1992). 11

[31] G. Grosso and G.P. Parravicini, *Solid State Physics*, Academic Press, 2000). 12

[32] S. Das Sarma and A. Pinczuk, *Perspectives in Quantum Hall Effects*, WILEY - VCH Verlag GmbH & Co.KGaA, Weinheim, 2004. 13, 22, 72

[33] J.P. Eisenstein, *Experimental Studies of Multicomponent Quantum Hall Systems* in [32], Chapter 2, Page 37 .

[34] S.M. Girvin and A.H. MacDonald, *Multicomponent Quantum Hall Systems: The Sum of Their Parts and More* in [32], Chapter 5, Page 161 . 21

[35] G.S. Boebinger, H.W. Jiang, L.N. Pfeiffer and K.W. West, *Phys. Rev. Lett.* **64**, 793 (1990) 17, 54, 55

[36] D. Yoshioka, A.H. MacDonald and S.M. Girvin, *Phys. Rev. B* **39**,1932 (1989) . 19

[37] S. He, S. Das Sarma and X.C. Xie, *Phys. Rev. B* **47**, 4394 (1993). 19

[38] J.P. Eisenstein and A.H. MacDonald *Nature* **432**, 691 (2004). 21

[39] J.P. Eisenstein, L.N. Pfeiffer and K.W. West, *Appl. Phys. Lett.* **57**, 2324 (1990). 21

[40] N. Kumada, K. Muraki, K. Hashimoto, and Y. Hirayama, *Phys. Rev. Lett.* **94**, 096802 (2005). 24

[41] N. Kumada, K. Muraki, and Y. Hirayama, *Phys. Rev. Lett.* **99**, 076805 (2007). 24

[42] V. Pellegrini, A. Pinczuk, B.S. Dennis, L.N. Pfeiffer and K.W. West, *Proceedings of the Würzburg Conference on "High Magnetic Fields in Semiconductor Physics"* (1996). 24, 33

[43] Y.A. Pusep, L.F. dos Santos, G.M. Gusev, D. Smirnov and A.K. Bakarov, *Phys. Rev. B* **109** , 046802 (2012). 24, 33

[44] I.V. Kukushkin, K. von Klitzing and K. Eberl, *Phys. Rev. B* **55** , 10607 (1997). 26, 30

[45] M. Dahl, D. Heiman, A. Pinczuk, B.B. Goldberg, L.N. Pfeiffer and K.W. West, *Phys. Rev. B* **45** , 6957 (1992). 31

[46] H.W. Yoon, M.D. Sturge and L.N. Pfeiffer, *Solid State Commun.* **104** , 287 (1997). 32, 33

[47] E.I. Rashba and M.D. Sturge, *Phys. Rev. B* **63** , 045305 (2000). 32, 53

[48] A.H. MacDonald and E.H. Rezayi, *Phys. Rev. B* **42** , 3224 (1990). 32

[49] A. Wojs, J.J. Quinn and P. Hawrylak, *Phys. Rev. B* **62** , 4630 (2000). 33, 62

[50] T. Vanhoucke and M. Hayne, M. Henini and V.V. Moshchalkov *Phys. Rev. B* **63**, 125331 (2001). 33, 50, 62, 63

[51] I. Bar-Joseph, G. Yusa and H. Shtrikman, *Solid State Commun.* **127** , 765 (2003). 33, 62, 64, 70

[52] B.M. Ashkinadze, E. Linder, E. Cohen, A.B. Dzyubenko and L.N. Pfeiffer, *Phys. Rev. B* **69** , 115303 (2004). 33

[53] A.J. Shields, J.L. Osborne, D.M. Whittaker, M.Y. Simmons, M. Pepper and D.A. Ritchie *Solid-State Electronics* **55** , 1318 (1997). 33

[54] K.S. Lee, S.K. Noh and S.K.Chang *Phys. Rev. B* **76** , 073305 (2007). 33

[55] N.H. Balshaw *Practical Cryogenics*, Oxford Instruments Superconductivity Limited, Oxon, 2001. 36, 37

[56] L.J. van der Pauw, *Philips Res. Repts* **13** , 1 (1956). 41

[57] N.J. Traynor, R.J. Warburton, M.J. Snelling and R.T. Harley *Phys. Rev. B* **55**, 15701 (1997). 50

[58] M. Stern, P. Plochocka, V. Umansky, D.K. Maude, M. Potemski, and I. Bar-Joseph *Phys. Rev. Lett.* **105**, 096801 (2010). 50

[59] J.L. Osborne, A.J. Shields, M.Y. Simmons, N.R. Cooper, D.A. Ritchie and M. Pepper *Physica B* **249-251**, 538 (1998). 51

[60] M.J. Snelling, E. Blackwood, C.J. McDonagh, R.T. Harley, and C.T.B. Foxon *Phys. Rev. B* **45**, 3922 (1992). 63

[61] Y.N. Joglekar and A.H. MacDonald, *Phys. Rev. B* **65** , 235319 (2002). 65

[62] A. Sawada, Z.F. Ezawa, H. Ohno, Y. Hari Koshi, Y. Ohno, S. Kishimoto, F. Matsukura, M. Yasumoto, and A. Urayama, *Phys. Rev. Lett.* **80** , 4534 (1998). 65

[63] A.R. Champagne, A.D.K. Finck, J.P. Eisenstein, L.N. Pfeiffer, and K.W. West, *Phys. Rev. B* **78**, 205310 (2008). 65, 70

[64] I. Aliaj *et.al.* in preparation. 70